Institutt for fysikk og teknologi

Bjarte Alsaker Mohn

Charged Higgs boson searches and SemiConductor Tracker commissioning for the ATLAS experiment

2007

Abstract

The ATLAS (A Toroidal Lhc ApparatuS) experiment is one of four major experiments presently being installed at the upcoming Large Hadron Collider (LHC) at the European Centre for Nuclear Research (CERN) outside Geneva. In this thesis we present work done on both the simulation of the ATLAS physics potential for a charged Higgs boson and the construction of the Semiconductor Tracker (SCT) - a subdetector within the ATLAS Inner Detector.

The discovery of a charged Higgs boson would be an unambiguous sign of physics beyond the Standard Model (SM) and it is thus of great interest to study the ATLAS potential for a charged Higgs discovery. Two such studies have been conducted for this thesis. In the first study a large-mass-splitting Minimal Supersymmetric Standard Model (MSSM) is assumed in which the charged Higgs boson decays into a W boson and a neutral Higgs may receive a large branching ratio. We conclude, however, that charged Higgs searches in this decay channel are made difficult by a large irreducible SM background.

Despite its small brancing ratio at high masses for the charged Higgs boson, the decay mode $H^{\pm} \to \tau\nu$ remains the most powerful decay mode for a charged Higgs discovery. Discovery through this channel depends heavily on excellent detector performance and understanding of the background. We show that with detector full simulation and with more complete background samples this channel still remains the most powerful decay mode. We also show that it is possible to connect the discovery countour for charged Higgs boson masses below and above the top-quark mass.

The SCT detector is a tracking detector based on silicon microstrip detector technology. It is a highly modular detector consisting of 4088 detector modules that are mounted on 4 barrels and 9x2 end cap disks. Some 320 of the SCT barrel detector modules were built by a Scandinavian collaboration and presented here are the results of this work and procedures for building and quality assurance.

Each SCT detector module is powered by an individual high and low voltage supply and thus a large scale and robust power supply control system is needed for controlling the SCT detector. Presented in this thesis is work done to prepare the SCT power supply software for this task, as well as the results obtained during testing and development.

As a part of the commissioning of the completed SCT barrel, a series of cosmic runs were performed. Data from these runs allowed for first studies of the detector alignment and alignment results and conlusions thereof are presented in this thesis.

List of Work

This thesis is based on the following papers, which are referred to in the text by their Roman numerals.

I Mohn B., Gollub N. and Assamagan K. (2005) The ATLAS discovery potential for a heavy Charged Higgs boson in a large mass splitting MSSM scenario.
ATL-PHYS-PUB-2005-017.

II Mohn B., Flechl M. and Alwall J. (2006) ATLAS discovery potential for the Charged Higgs Boson in $H^+ \rightarrow \tau\nu$ decays.
ATL-PHYS-PUB-2007-006.

III Johansen, L. G. *et al.* (2006) Production of ATLAS silicon detector modules - Report from the Scandinavian Cluster.
ATL-INDET-PUB-2006-003

IV Mohn B., Phillips P. W., Stanecka E. (2007) SCT Power Supply PVSS Software
ATL-IS-ON-0001 (EDMS ID: 841651)

V Abdelouahab Abdesselam, AA. *et al.* (2007) The Detector Control System of the ATLAS SemiCondutor Tracker during Macro-Assembly and Integration
ATL-COM-INDET-2007-010

Additional work is presented in Chapters 5 and 6 as explained in the Introduction.

Contents

1. Introduction

The aim of particle physics is to identify and explain the fundamental building blocks of matter and the forces of nature which make up the world that surrounds us. Today the Standard Model of particle physics is a firmly established theory which predictions have been experimentally verified with excellent agreement. Yet it is also known that in its present version the Standard Model can not be a final theory as it does not incorporate gravity and furthermore is unable to explain experimentally verified phenomena such as dark matter.

Particle physicists around the world are hoping for the Large Hadron Collider (LHC) to answer many of the open questions. The LHC is presently under construction at the European Organisation for Nuclear Research (CERN), outside Geneva, Switzerland, and is scheduled to become operational during the first months of 2008. At four collision points it will collide protons head on at the unprecedented centre-of-mass energy of 14 TeV.

At one of the four collisions points the ATLAS experiment is currently being installed. It is a multi-purpose detector designed to exploit the full physics potential of the upcoming LHC collider, and the work done for this thesis has been performed within the ATLAS collaboration. The work is divided in two parts, where first part relates to Supersymmetric extensions of the Standard Model and more specifically the possibility to detect charged Higgs bosons predicted by such models with the ATLAS detector. The second part of this thesis deals with the construction and commisioning of the SemiConductor Tracker (SCT), one of the three subdetectors of the ATLAS Inner Detector.

This thesis thus follows a structure in which Chapter 2 gives an introduction to the formalism of the mathematical foundations of modern particle physics, as well its shortcomings. A short introduction to the Minimal Supersymmetric Standard model (MSSM) is also given with emphasis on charged Higgs boson production and decay. Chapter 3 then presents the most recent experimental constraints on the charged Higgs boson's existence as well as the outlook for a charged Higgs boson discovery with the ATLAS detector derived from simulation studies of the detector. The work done for Paper I and II of this thesis are thus put in a perspective.

A short introduction to the ATLAS detector and its sub detectors is given in Chapter 4, and a more detailed introduction to the SemiConductor Tracker is given in Chapter 5. The SCT detector has an important role in this thesis starting with the production of 320 SCT barrel detector modules carried out in

collaboration between the universities of Bergen, Oslo and Uppsala. The SCT barrel detector module is explained in Section 5.1 while the module production itself, to which I contributied by carrying out the quality assurance tests, is described in Section 5.2 and Paper III.

Once tested and passed, the completed detector modules were sent to the macro assembly site at Oxford University where they were mounted onto their support structures. Section 5.3 explains the macro-structures of the SCT detector, and Section 5.3.1 gives an overview of the work carried out to calibrate and understand the performance of the humidity sensors mounted on the SCT detector, to which I contributed to by performing data analysis.

In total the SCT detector consists of 4088 silicon detector modules, all of which have to be individually supplied with both high and low voltage. For this thesis I have been working on the SCT Detector Control System (DCS) and in particular the power supply software. An overview of the DCS system is thus given in Section 5.4, with emphasis on the power supply hardware and software. My contribution to the software development has been to redesign the software used during macro-assembly and prepare it for full scale deployment in the ATLAS cavern where it will run as a distributed software on several computers. The modifications also involved the implementation of the Finite State Machine (FSM) through which the SCT DCS will be integrated into the central ATLAS DCS. The present state of the software is presented in Sections 5.4.2 and 5.4.3, and in Paper IV. As software evolves with time and experience the material presented here represent a snapshot of the software at the time of writing.

The SCT barrel was completed and ready for commissioning in February 2006, and for a period of 4 months, while the detector was still on surface, the SCT barrel collected cosmic data as a part of the commisioning phase. These cosmic runs were invaluable tests of the both the Data Acquisition (DAQ) and DCS systems of the detector as well as a starting point for the detector alignment group. For this thesis both DCS and alignment work was carried out. The DCS work is summarized in Paper V, to which I contributed by analysing the power supply performance.

With the reconstructed cosmic tracks it was possible to perform the first alignment of the SCT detector. Chapter 6 is devoted to the alignment of the SCT barrel using the local χ^2 alignment algorithm, a work carried out in collaboration with Ola K. Øye. We showed that by slightly modifying the algorithm stable alignment parameters could be obtained that were in good agreement with the expected build precision of the SCT barrel.

A conclusion and outlook is given at the end of the thesis, followed by an informal summary in Norwegian.

2. Theoretical Background

The Standard Model (SM) of particle physics is one of the most succesful theories of modern science. It explains the fundamental building blocks of nature as well as the three important forces: the electromagnetic force, the weak force and the strong force. Numerous textbooks have been written on the basics of the SM and the interested reader can find more information in Ref. [19, 41, 21] that go beyond the summary of the present chapter.

Despite its huge success in describing the observed physics the Standard Model has intrinsic problems which motivates the extension of the SM to include new particles and new interactions that are not yet known. Among the the most popular extensions are theories of Supersymmetry in which the so-called Higgs sector contains five Higgs bosons contrary to only one within the Standard Model.

This chapter first presents the basics of the Standard Model in Section 2.1 before looking at some of the short comings of the SM in Section 2.2. Possible extensions to the SM are treated in Section 2.3, in particular the Minimal Supersymmetric Standard Model (MSSM).

2.1 Standard Model

The Standard Model groups elementary particles into two classes: bosons (particles that transmit forces) and fermions (particles that make up matter). The bosons have integeger particle spin (0, 1, 2 *etc*) while fermions have half integer spin (1/2, 3/2, 5/2 *etc*).

Within the fermion class of elementary particles we find two different subclasses, these are the leptons and quarks. The leptons and quarks are themselves divided into three generations according to their characteristics, and Table 2.1 shows how they are organised.

In addition to electrical charge the quarks have what we call colour charge, which is the charge of the strong force. Each quark flavour comes in three different colours but since coloured objects do not exist as free objects in nature they need to combine to make up composite particles where colour charge cancels out. This phenomen is called confinement.

The second class of particles in the SM is the bosons. They transmit the different forces between the leptons and quarks and we can split them in two groups depending on whether they belong to the unified electroweak force (electromagnetic + weak force) or the strong force, see Table 2.2. The gravi-

Generation	**I**	mass [MeV]	**II**	mass [GeV]	**III**	mass [GeV]	Q [q_e]
Leptons	e	0.51	μ	0.105	τ	1.777	-1
	ν_e	$< 3 \cdot 10^{-6}$	ν_μ	< 0.19	ν_τ	< 0.018	0
Quarks	u	1.5 to 3.0	c	1.25 ± 0.09	t	178.0 ± 4.3	+2/3
	d	3 to 7	s	0.095 ± 0.025	b	4.5 ± 0.07	$-1/3$

Table 2.1: *The fermions (leptons and quarks) in the SM. Neutrinoes were for a long time thought to be massless but recent observations of neutrino oscillations show that they must have a small non-zero mass. For further details about the particle masses and how they are determined see [55].*

Interaction	particle	spin	mass [GeV]	Q [q_e]
Electroweak force	γ	1	0	0
	$W^\pm$	1	80.403 ± 0.029	± 1
	Z^0	1	91.1876 ± 0.0021	0
Strong force	g	1	0	0

Table 2.2: *The bosons in the SM. The zero mass of the photon reflects its infinite range while the heavy $W^\pm$ and Z^0 bosons have a very short range. The massless gluons have colour charge and are hence subject to confinement and limited to a very short interaction range.*

tational force is not a part of the SM since it is very weak at the distances and respective energies accesible in present particle physics experiments.

In the SM, particles interact via the exchange of a virtual force carrier (vector gauge boson). Passing virtual photons between electrically charged particles yields the electromagnetic force, exchanging virtual W's and Z's between quarks and leptons produce the weak subnuclear force and rapid emission of gluons between themselves and quarks make up the strong force.

The existence of one additional boson, the Higgs boson, is predicted by the SM but has not been observed yet. The Higgs boson is associated with the Higgs mechanism, a proposed mechanism to give masses to the fundamental particles of the SM. See Section 2.1.3 for more details about the Higgs mechanism.

2.1.1 Quantum Electro Dynamics (QED)

The Standard Model is a local gauge theory which means that the physical observables of the Model do not change when the fields of the theory are transformed according to some transformation rule. In more mathematical words this means that if we are allowed to change the fields independently at ev-

ery space-time point x, then the Lagrangian of the theory should remain the same. Let us consider a Lagrangian describing a free (non-interacting) spin 1/2 fermion:

$$\mathscr{L}_0(x) = \bar{\psi}(x)(i\gamma^\mu \partial_\mu - m)\psi(x) \tag{2.1}$$

The free Lagrangian is invariant under global U(1) transformations in which $\psi(x) \rightarrow \psi^{'}(x) = \psi(x)e^{-iq\chi}$, but not under local U(1) transformations in which $\chi \rightarrow \chi(x)$ because

$$\partial_\mu \psi(x) \quad \rightarrow \quad e^{iq\chi(x)}(\partial_\mu + iq\partial_\mu \chi(x))\psi(x). \tag{2.2}$$

For the Lagrangian to be invariant under this local transformation we need to add an additional piece to it which transforms in such a way that it cancels the contribution from the $\partial_\mu \chi(x)$ term. Hence we introduce a new spin 1 field which tranforms as

$$A_\mu(x) \rightarrow A_\mu^{'}(x) = A_\mu(x) + \partial_\mu \chi(x), \tag{2.3}$$

and furthermore we define the covariant derivative

$$D_\mu \psi(x) = [\partial^\mu + iqA_\mu(x)]\psi(x). \tag{2.4}$$

The covariant derivative has the proporty that it transforms like the field itself:

$$D_\mu \psi(x) \rightarrow (D_\mu^\psi)'(x) = e^{iq\chi(x)} D_\mu \psi(x). \tag{2.5}$$

The new Lagrangian

$$\mathscr{L} = \bar{\psi}(x)(i\gamma^\mu D_\mu - m)\psi(x) = \mathscr{L}_0(x) - q\bar{\psi}(x)\gamma^\mu \psi(x)A_\mu(x) \tag{2.6}$$

is invariant under the simultaneous transformations (2.2) and (2.3). A direct consequence from the requirement that the free-field Lagrangian density $\mathscr{L}_0$ should be invariant under local U(1) phase transformations is that we have obtained a new Lagrangian density with an interaction term which creates an interaction betweeen the fermion field $\psi(x)$ and the gauge field $A_\mu(x)$. If we want $A_\mu(x)$ to be a true propagating field we need to add a gauge invariant free field kinetic term to the Lagrangian at which point we would have the QED Lagrangian for one type of fermions, and the vector field $A_\mu(x)$ would represent photons.

For QED the absence of a mass term $\frac{1}{2}m^2 A_\mu(x)A^\mu(x)$ in the Lagrangian density is as it should be. Photons are indeed massless. This however causes problems when we turn to weak interactions, as we shall see in the next section.

2.1.2 The Electro Weak Interaction

While the electromagnetic interaction is an Abelian local U(1) symmetry the weak theory is described using the non-Abelian symmetry group SU(2). From experimental observations it is known that weak charged currents only involve left-handed fermion fields and right-handed anti-fields. This motivates us to write the Lagrangian in the following way

$$\mathscr{L}_0 = i[\bar{\Psi}_l^L(x)\partial\Psi_l^L(x) + \bar{\psi}_l^R(x)\partial\psi_l^R(x) + \bar{\psi}_{\nu_l}^R(x)\partial\psi_{\nu_l}^R(x)], \tag{2.7}$$

where $\Psi_l^L(x)$ is the doublet field

$$\Psi_l^L(x) = \begin{pmatrix} \psi_{\nu_l}^L(x) \\ \psi_l^L(x) \end{pmatrix}. \tag{2.8}$$

The Lagrangian (2.7) is invariant under the global SU(2) transformations

$$\begin{array}{rcl} \Psi_l^L(x) & \rightarrow & \Psi_l^{L\prime}(x) = U(g)\Psi_l^L(x) = e^{(ig_j\tau_j/2)}\Psi_l^L(x) \\ \psi_l^R(x) & \rightarrow & \psi_l^{R\prime}(x) = \psi_l^R(x) \\ \psi_{\nu_l}^R(x) & \rightarrow & \psi_{\nu_l}^{R\prime}(x) = \psi_l^R(x) \end{array} \tag{2.9}$$

where we have defined each right-handed lepton field to be a weak isoscalar, i.e. to be invariant under SU(2) transformations. $g_{1,2,3}$ are any real numbers and $\tau_{1,2,3}$ are the 2x2 hermetian Pauli matrices.

According to Noether's theorem the invariance under a global transformation corresponds to a consverved quantity (current) which here can be identified as the weak isospin charges I_i^W. Furthermore if we impose that the langrangian (2.7) in addition should invariant under global U(1) transformations then this leads to the conservation of weak hypercharge Y. It can then be shown that the conservation of the electric charge follows from the relation

$$Y = Q/q_e - I_3^W. \tag{2.10}$$

We now require that the Lagrangian should be invariant under local SU(2)xU(1) tranformations and in order for this to be possible we shall replace the fermion derivatives with covariant objects which contain new gauge fields. Since we have four gauge parameters four different gauge fields are needed:

$$D^\mu\Psi_l^L(x) = [\partial^\mu + ig\tau_j W_j^\mu(x)/2 - ig'B^\mu(x)/2]\Psi_l^L(x) \tag{2.11}$$

$$D^\mu\psi_l^R(x) = [\partial^\mu - ig'B^\mu(x)]\psi_l^R(x) \tag{2.12}$$

The fields $W_i^\mu(x)$ are defined to be invariant under U(1) transformations and $B^\mu(x)$ to be invariant under SU(2) transformations. The new Lagrangian is SU(2)xU(1) gauge-invariant and if we write the Lagrangian in the form $\mathscr{L} =$

$\mathscr{L}_0 + \mathscr{L}_I$ then the interaction part of the Lagrangian takes the form (for simplicity of notation the spacial dependency of the fields and currents is from now on left out):

$$\begin{aligned}\mathscr{L}_I &= i\bar{\Psi}_l^L[ig\tau_j \not{W}_j/2 - ig'\not{B}]\Psi_l^L + \bar{\psi}_l^R[-ig'\not{B}]\psi_l^R \\ &= -gJ_j^\mu W_{j\mu} - g'J_Y^\mu B_\mu \end{aligned} \tag{2.13}$$

The interaction part of the new Lagrangian represent the interaction between the weak isospin current J_j^μ, the weak hypercharge current J_Y^μ and the gauge fields $W_{j\mu}$ and B_μ. If $W_{1\mu}$ and $W_{2\mu}$ were to be interpreted as the gauge field of the charged weak interaction (mediated by $W^\pm$ bosons) and $W_{3\mu}$ as the neutral weak interaction (mediated by W^0) then the charged and neutral weak interactions would have the same strength and this is in contradiction with experimental observations. Instead it turns out that the gauge fields $W_{3\mu}$ and B_μ combine into the physical photon and Z^0 fields:

$$A_\mu = \sin\theta_W W_{3\mu} + \cos\theta_W B_\mu \tag{2.14}$$

$$Z_\mu = \cos\theta_W W_{3\mu} - \sin\theta_W B_\mu \tag{2.15}$$

The angle θ_W is the weak mixing angle, also known as the Weinberg angle, and if we require that the gauge field A_μ is the electromagnetic field and is coupled to electric charges the usual way then we have to require

$$g\sin\theta_W = g'\cos\theta_W = q_e. \tag{2.16}$$

In other words the coupling strengths of the weak interactions are related to the coupling strength of the electromagnetic interaction.

In order to give the fields $W_{1\mu}$ and $W_{2\mu}$ a physical interpretation they are linearly combined to the new fields W and $W^\dagger$ and the interaction Lagrangian of the electroweak theory takes the final form

$$\begin{aligned}\mathscr{L}_I = &-q\bar{\psi}\gamma^\mu\psi A_\mu - \frac{g}{2\sqrt{2}}[J^{\mu\dagger}W_\mu + J^\mu W_\mu^\dagger] \\ &-\frac{g}{cos\theta_W}[J_3^\mu - sin^2\theta_w q\bar{\psi}\gamma^\mu\psi/e]Z_\mu. \end{aligned} \tag{2.17}$$

The first term of this SU(2)xU(1) gauge-invariant interaction Lagrangian is the familiar interaction of QED as shown in Equation (2.6). This is obtained by imposing the condition (2.16). The second term is charged weak currents mediated by the $W^\pm$ bosons while the last term describes netrual weak current mediated by the Z^0 boson.

In the examples above we have considered one family of leptons in our equations but the equations would be the same with any fermionic doublet. However, the $W^\pm$ bosons do not couple to the quark mass eigenstate shown in Table 2.1 but to a linear combination of these. This is the origin behind flavour

changing currents and the transition between mass eigenstates is described by the 3x3 Cabibbo-Kobayashi-Maskawa (CKM) matrix:

$$\begin{pmatrix} d' \\ s' \\ b' \end{pmatrix} = \begin{pmatrix} V_{ud} & V_{us} & V_{ub} \\ V_{cd} & V_{cd} & V_{cd} \\ V_{td} & V_{ts} & V_{tb} \end{pmatrix} \begin{pmatrix} d \\ s \\ b \end{pmatrix} \tag{2.18}$$

We saw that in the case of QED the absence of a mass term for the $A^{\mu}(x)$ field is correct (photons are massless), but the new electroweak Lagrangian describes processes mediated by the massive $W^{\pm}$ and Z^{o} bosons and for the Lagrangian to be correct we need to introduce mass terms for these fields. But in a gauge theory, the gauge fields have to be massless because any term of the kind $\frac{1}{2}M^2 W_{j\mu} W_j^{\mu}$ would break the U(1) symmetry. Hence we are left with massless gauge fields and the solution to this problem is known as *spontaneous symmetry breaking* a concept to be outlined in the next section.

2.1.3 Spontaneous Symmetry Breaking

The Goldstone Model

The Goldstone model is the simplest example of a field theory with spontaneous symmetry breaking. The Lagrangian of the model is given by;

$$\mathscr{L} = [\partial^{\mu}\phi^{*}(x)][\partial_{\mu}\phi(x)] - \mathscr{V}(\phi) \tag{2.19}$$

where $\phi(x)$ is a complex scalar field

$$\phi(x) = \frac{1}{\sqrt{2}}[\phi_1(x) + i\phi_2(x)] \tag{2.20}$$

and the potential $\mathscr{V}(\phi)$ is

$$\mathscr{V}(\phi) = \mu^2|\phi(x)|^2 + \lambda|\phi(x)|^4. \tag{2.21}$$

μ^2 and λ are real parameters. In order to have the energy bounded from below, i.e. for a ground state to exist, we note that λ must be positive, $\lambda > 0$. Two cases now arise. If μ^2 is positive the potential energy will have its minimum for $\phi(x) = 0$. In this case the vacuum state is unique and there is no symmetry breaking. In the case when μ^2 is negative the potential will have a minimum value for

$$\phi(x) = \phi_0 = \sqrt{\frac{\mu^2}{2\lambda}}e^{i\theta}, \qquad 0 \leq \theta < 2\pi. \tag{2.22}$$

This is a circle in the ϕ_1-ϕ_2 (See Figure 2.1) plane and hence the vacuum state is not unique. We now make a choice and take $\theta_{vac} = 0$. In doing this we

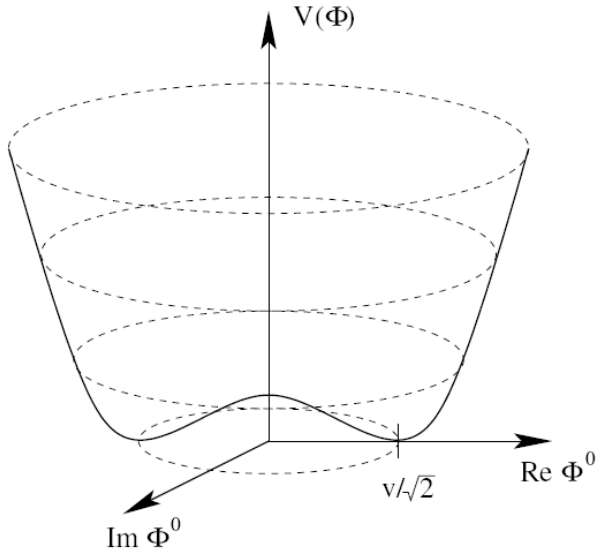

Figure 2.1: The potential $\mathscr{V}(\phi)$ of the Goldstone model when μ^2 is negative.

violate the invariance of the Goldstone model Lagrangian (2.19) under global U(1) transformations. The symmetry is broken given the value

$$\phi_0 = \sqrt{\frac{\mu^2}{2\lambda}} = \frac{1}{\sqrt{2}}v. \tag{2.23}$$

For the ground state we can now choose a new basis for $\phi(x)$ i.e. we rotate the coordinate system.

$$\phi(x) = \frac{1}{\sqrt{2}}[v + \sigma(x) + i\eta(x)] \tag{2.24}$$

$\sigma(x)$ and $\eta(x)$ are two real fields and they measure the deviations of the field from the equilibrium ground state configuration $\phi(x) = \phi_0$. In terms of these new fields we can rewrite the Lagrangian density of the Goldstone model

$$\begin{aligned}\mathscr{L}(x) &= \frac{1}{2}[\partial^\mu\sigma(x)][\partial_\mu\sigma(x)] - \frac{1}{2}(2\lambda v^2)\sigma^2(x) + \frac{1}{2}[\partial^\mu\eta(x)][\partial_\mu\eta(x)] \\ &\quad -\lambda v\sigma(x)[\sigma^2(x)+\eta^2(x)] - \frac{1}{4}[\sigma^2(x)+\eta^2(x)]^2,\end{aligned} \tag{2.25}$$

where a constant term has been omitted. Although expressed in a different way, this is the same Lagrangian density as in (2.19), i.e. it describes the same physics. The first three terms of Equation (2.25) is the free-field part, while the terms of order three or higher in $\sigma(x)$ and $\eta(x)$ represent interactions. From the free-field part we conclude that given $\mu^2 < 0$ the Goldstone model gives rise to two neutral scalar (spin 0) boson fields, $\sigma(x)$ and $\eta(x)$. The σ

bosons are massive with their mass given by $m_\sigma = \sqrt{2\lambda v^2}$, while the η's are left massless since there is no $\eta^2(x)$ term. The zero mass of the η bosons is a direct consequence of the degeneracy of the vacuum state and they are known as Goldstone bosons. They do not exist in nature but occur frequently in theories with spontaneuos broken symmetry.

The Higgs Model

The Higgs model is a simple example of how we can make use of spontaneous broken symmetry to give gauge bosons, like $W^\pm$ and Z^0, masses without destroying the gauge invariance of the gauge theory.

Starting out with the Lagrangian density of the Goldstone model we now introduce a covariant derivative instead of the partial derivative and add a free-field term for the gauge field $A_\mu(x)$. The Lagrangian density of the Higgs model is hence given by

$$\mathscr{L} = [D^\mu \phi(x)]^* [D_\mu \phi(x)] - \mu^2 |\phi(x)|^2 - \lambda |\phi(x)|^4 - \frac{1}{4} F_{\mu\nu}(x) F^{\mu\nu}(x), \quad (2.26)$$

where the field strength tensor $F_{\mu\nu}(x)$ is defined as

$$F_{\mu\nu}(x) = \partial_\nu A_\mu(x) - \partial_\mu A_\nu(x). \quad (2.27)$$

The Higgs model Lagrangian is invariant under local U(1) phase transformations as outlined in Section 2.1.1 replacing the spinor field $\psi(x)$ with $\phi(x)$ and $\bar{\psi}(x)$ with $\phi^*(x)$. Like the Goldstone model there is nothing special about the case when μ^2 is positive. In fact the lowest energy corresponds to both $\phi(x)$ and $A_\mu(x)$ vanishing. For μ^2 negative the vacuum state is however degenerated leading to spontaneous symmetry breaking. To preserve Lorentz invariance the gauge field $A_\mu(x)$ must vanish for the vacuum, but we again obtain a circle of minimum potential. Like the Goldstone model we choose a real value for the ground state (2.23) and expand the field $\phi(x)$ (2.24). The Lagrangian can then be written as:

$$\begin{aligned} \mathscr{L}(x) \quad = \quad & \frac{1}{2}[\partial^\mu \sigma(x)][\partial_\mu \sigma(x)] - \frac{1}{2}(2\lambda v^2)\sigma^2(x) - \frac{1}{4} F_{\mu\nu}(x) F^{\mu\nu}(x) \\ & + \frac{1}{2}(qv)^2 A_\mu(x) A^\nu(x) + \frac{1}{2}[\partial^\mu \eta(x)][\partial_\mu \eta(x)] + qv A^\mu(x) \partial_\mu \eta(x) \\ & + \text{'interaction terms'} \end{aligned} \quad (2.28)$$

The interaction terms are terms of order three or higher and an insignificant constant has been omitted. There is however a problem with this Lagrangian density. The third term on the second line couples the fields $A_\mu(x)$ and $\eta(x)$ but being of second order it is not an interactions term. This means that the $A_\mu(x)$ and $\eta(x)$ fields are not independent of each other.

Counting the number of degrees of freedom of the original Lagrangian density (2.26) and the "new" one (2.28) leaves us with one degree of freedom too

many in the new Lagrangian density. This can be solved by transforming the $\eta(x)$ field away by means of a U(1) gauge transformation, and this will at the same time remove the unwanted term as discussed above. The chosen gauge is called the *unitary gauge* and in this gauge the free-field Lagrangian has the form:

$$\begin{aligned}\mathscr{L}_0(x) &= \frac{1}{2}[\partial^\mu\sigma(x)][\partial_\mu\sigma(x)] - \frac{1}{2}(2\lambda v^2)\sigma^2(x) \\ &\quad -\frac{1}{4}F_{\mu\nu}(x)F^{\mu\nu}(x) + \frac{1}{2}(qv)^2 A_\mu(x)A^\nu(x) \qquad (2.29)\end{aligned}$$

When quantized the free-field Lagrangian represents one real scalar field, $\sigma(x)$, with its mass given by $m_\sigma = \sqrt{2\lambda v^2}$ and one gauge field, $A_\mu(x)$, with mass $|qv|$. (In comparison we started out with a complex scalar field and a massless gauge field.) The scalar particle associated with the field $\sigma(x)$ is the so-called Higgs boson and the mechanism in which a vector boson acquires mass without destroying the gauge invariance of the Lagrangian is known as the Higgs mechanism.

In the Standard Model the broken symmetry is the SU(2) symmetry and the mechanism for that is very similar to the abelian U(1) symmetry breaking outlined above. We introduce a weak isospin doublet

$$\Phi(x) = \begin{pmatrix} \phi_a(x) \\ \phi_b(x) \end{pmatrix}, \qquad (2.30)$$

which transforms the same way as the doublet field $\Psi_l^L(x)$ under SU(2)xU(1) transformations and couples to the vector fields through the Lagrangian

$$\mathscr{L}_\Phi = [D^\mu\Phi(x)]^*[D_\mu\Phi(x)] - \mu^2|\Phi(x)|^2 - \lambda|\Phi(x)|^4. \qquad (2.31)$$

Again we take $\mu^2 < 0$ which leads to a degenerate vacuum state and we can break the symmetry by choosing the vacuum state

$$\Phi_0(x) = \begin{pmatrix} \phi_a^0(x) \\ \phi_b^0(x) \end{pmatrix} = \begin{pmatrix} 0 \\ v/\sqrt{2} \end{pmatrix} \qquad (2.32)$$

In the Standard Model the upper component of the Higgs doublet is electrically charged while the lower is neutral and to ensure an electrically neutral vacuum state we choose our vacuum state so that the charged component is zero. This choice can also be motivated by the need to keep the photon massless when the symmetry is broken.

Once again we parametrize the field in terms of deviations from the vaccum state

$$\Phi(x) = \frac{1}{\sqrt{(2)}}\begin{pmatrix} \eta_1(x) + i\eta_2(x) \\ v + \sigma(x) + i\eta_3(x) \end{pmatrix}, \qquad (2.33)$$

and by using the unitary gauge we are able to transform away the $\eta(x)$ fields in which process the $W^{\pm}$ and Z^0 bosons acquire mass terms. In this way three of the four introduced degrees of freedom are absorbed as mass terms for the gauge bosons leaving the fourth degree of freedom as the physical scalar Higgs particle.

The Standard Model Higgs sector is the simplest possible mechanism predicting only one Higgs boson. However, nothing restricts us from adding more Higgs fields to the model, increasing the number of expected Higgs bosons, and as long as no Higgs boson has been experimentally observed we can not rule more complicated models. The present 95% CL from LEP on the lower Higgs boson mass limit is 114.4 GeV [12].

2.2 Problems with the Standard Model

Despite its success in predicting the mass and properties of the W and Z bosons before they were experimentally found, it is widely accepted that the Standard Model can not be the finite theory to explain all microscopic aspects of nature. Not only does the SM need a lot of experimental input, it also has several theoretical problems.

At least 19 parameters have to be determined experimentally as input to the SM, a situation which clearly is not very satisfactory for a fundamental theory. Among these parameters are the particle masses which arise through the Yukawa couplings between the Higgs field and the fermions. The 3 Yukawa coupling constants (one for each fermion generation) are free parameters of the theory and hence the SM is unable to explain the large range of particle masses detected.

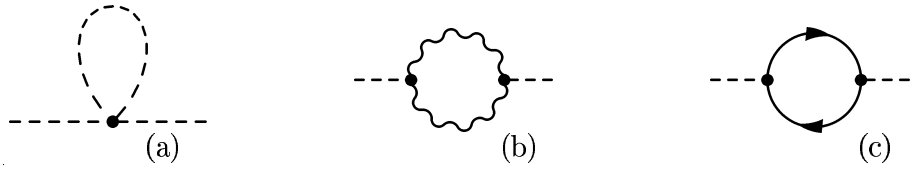

Figure 2.2: Corrections (radiative) to the Higgs boson mass: a) Quartic Higgs self-coupling term. b) Gauge boson loops. c) Fermion loops

The mass of the Higgs boson is another parameter which is connected with problems. In the electroweak Lagrangian the Higgs boson couples to all particles, thus when calculating higher order corrections to the Higgs mass contributions arise from each SM particle. In Figure 2.2c one such correction is represented by the fermion loop and in the case of a fermion of mass m_f the correction to m_H^2 is given by

$$\Delta m_H^2 = \frac{|\lambda_f|^2}{16\pi^2}\left[-2\Lambda_{UV}^2 + 6m_f^2 \ln(\Lambda_{UV}/m_f + \cdots)\right]. \tag{2.34}$$

Here Λ_{UV} is the cut of scale used to regulate the loop integral and it should be intepreted as the energy scale at which new physics enters. At the Planck scale (10^{19} GeV) we know that the SM must break down since gravity can no longer be neglected, hence Λ_{UV} is often taken to be of order M_P. With this choice of Λ_{UV} the quantum correction to m_H^2 is some 30 orders of magnitude larger then the value required by electro-weak measurements of the SM $m_H^2 \sim (100GeV)^2$. This is clearly not acceptable and requires a remarkable finetuning of parameters so that the different contributions cancel. This is considered an unnatural procedure and the problem is hence often referred to as the fine-tuning or unnaturalness problem of the Standard Model.

Finally recent cosmological observations made by the WMAP [13] experiment have revealed that only 4% of the Universe is made up of matter (i.e. particles) described by the SM. About 22% of the universe consists of so-called dark matter which is weakly interacting and hence can only indirectly be observed through its gravitational impact. The remaining 74% of the Universe is dark energy which is distinct different from dark matter and responsible for the present-day accelearation of the universe.

2.3 Beyond the Standard Model

To tackle the problems of the Standard Model many extensions and alternatives to it have been proposed. Some of the simplest solutions have already been ruled out by experiments while the more complex theories generally are still within the present constraints from data.

Among the most popular extensions to the Standard Model are theories of Supersymmetry (SUSY) in which there exist a supersymmetric partner for all particles in the SM. These supersymmetric partners have identical quantum numbers compared to their counterpart in the SM but their spin differ by 1/2. In other words, supersymmetry relates fermions and bosons, and a supersymmetry transformation turns a bosonic state into a fermionic and vice versa:

$$Q|fermion>=|boson>, \quad Q|boson>=|fermion> \tag{2.35}$$

There are several motivations behind SUSY and one of the most prominent ones is that with unbroken SUSY the contribution from supersymmetric particles in loop diagrams like 2.2c will exactly cancel the contribution of the SM particle. The reason is that in loop diagrams a fermionic particle comes with a relative minus sign as compared to a bosonic particle, and hence the problems with large corrections to the Higgs mass due to loop corrections vanishes in SUSY theories.

Another desirable feature of SUSY is the possibility for a Grand Unified Theory (GUT) in which the electromagnetic, weak and strong force unite at a higher energy scale, and that the 'complicated' SU(3)xSU(2)xU(1) symmetry of the SM is just the result of a larger symmetry group which is broken

at a higher energy. Unfortunately if the experimentally measured couplings constants are extrapolated in the SM to higher energies they do not unite, like shown in Figure 2.3a. However, if SUSY is realized with SUSY masses close to 1 TeV it will change the way the couplings run and they will unite at the scale of $\mathcal{O}$ 10^{16} GeV, as seen in Figure 2.3b.

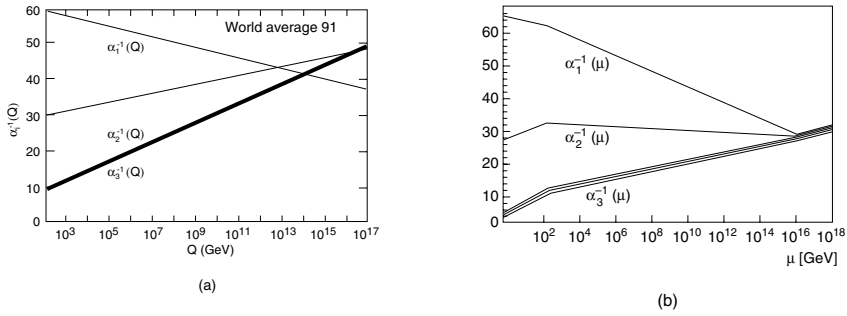

Figure 2.3: (a) The running of the coupling constants as experimentally measured and extrapolated in the SM. (b) If SUSY is realized with masses close to 1 TeV the running of the coupling constants change and they will unit at the scale of $\mathcal{O}$ 10^{16}. Figures taken from [24].

As the SUSY Lagrangian might contain gauge-invariant terms which would violate baryon or lepton number conservation, a new symmetry called R-parity, is introduced to eliminate such terms. The R-parity is a multiplicative symmetry and is defined as

$$P_R = (-1)^{3(B-L)+2s}, \tag{2.36}$$

where s is the particle spin, B is the baryon number and L is the lepton number. From the definition it follows that all SM particles (including the Higgs boson) have R-parity +1 while their supersymmetric partners have R-parity -1. Hence, in R-parity conserving processes sparticles have to be produced in pairs and when a sparticle decays it has to decay to one particle plus one lighter sparticle, causing the lightest supersymmetric particle (LSP) to be stable. If the LSP is neutral and not strongly interacting it may serve as good candidate for dark matter in the universe.

If supersymmetry was an unbroken symmetry there would exist supersymmetrics partner to the SM particles with the exact same mass. Such particles should be extremely easy to detect, and if they existed they should have been found a long time ago. Thus SUSY can not be a symmetry at our energy scale, and must be broken. SUSY breaking has to be designed carefully as one would otherwise risk destroying the cancellations of correction terms to the Higgs mass, one of the main reasons for why SUSY was introduced in the first place. SUSY is hence broken by the concept of ‘soft‘ supersymmetry

breaking:

$$\mathscr{L} = \mathscr{L}_{SUSY} + \mathscr{L}_{soft} \tag{2.37}$$

Here $\mathscr{L}_{soft}$ breaks the supersymmetry but only contains terms involving the masses and couplings with positive mass dimension. Various models for constructing the soft breaking exist on the market, among those Gauge Mediated Symmetry Breaking (GMSB) [23] and Anomaly Mediated Symmetry Breaking (AMSB) [49], but the discussion of those is beyond the scope of the present chapter.

The construction of a Lagrangian with soft breaking terms is not alone enough to ensure the cancellations of quadratically divergent terms to the Higgs mass, we also need to impose the condition that the mass difference between the SM particles and their superpartners can not be too large. More precisely the lightest few superpartners should have a mass of no higher than ~ 1 TeV an energy range well within the reach of the upcoming Large Hadron Collider (LHC) at CERN.

2.3.1 The Minimal Supersymmetric Standard Model (MSSM)

The Minimal Supersymmetric Standard Model is the supersymmetric extension to the SM with a minimal new particle content. In the MSSM the partners to the SM fermions are the spin-0 sfermions, and supersymmetric partners exist for both left and right handed fermion fields even though the concept of handedness is not defined for spin-0 particles. The lepton SUSY-partners are the sleptons where the selectron ($\tilde{e}$), smuon ($\tilde{\mu}$) and stau ($\tilde{\tau}$) together with the sneutrinoes ($\tilde{\nu}$) are the SUSY counterparts of the SM particles. The SM quarks have their partners in the squarks ($\tilde{q}$) following the same naming rule as the sleptons (stop, sbottom, *etc*).

While there is a direct one to one correspondance between the fermions mass eigenstates and the sfermion partners this is not the case for the SM vector bosons and their susy spin-1/2 partners. We saw in Section 2.1.2 that the observable states of the SM are linear combinations of 4 other gauge fields. The same situation is true also for the susy-partners, but the mixing between the gauge fields is different and they may also mix with the higgs sector. The resulting observerable state are two charginoes ($\tilde{\chi}^0_{1,2,3,4}$) and 4 neutralinoes ($\tilde{\chi}^{\pm}_{1,2}$)), where the subscript order them in mass.

In order to describe all particles of the MSSM as shown in Table 2.3 together with their interactions more than 100 parameters are needed as input to the model. The larger fraction of these parameters are related with the soft susy breaking term $\mathscr{L}_{soft}$ which also describes all the masses of the new particles.

The Higgs mechanism in MSSM

A feature of supersymmetric versions of the SM is that they need at least two Higgs doublets in order to give mass to all particles. The reason is two fold,

Names	spin	Mass Eigenstates	Gauge Eigenstates
Higgs bosons	0	$h^0\ H^0\ A^0\ H^\pm$	$H_u^0\ H_d^0\ H_u^+\ H_d^-$
squarks	0	$\tilde{u}_L\ \tilde{u}_R\ \tilde{d}_L\ \tilde{d}_R$ $\tilde{s}_L\ \tilde{s}_R\ \tilde{c}_L\ \tilde{c}_R$ $\tilde{t}_1\ \tilde{t}_2\ \tilde{b}_1\ \tilde{b}_2$	$\tilde{u}_L\ \tilde{u}_R\ \tilde{d}_L\ \tilde{d}_R$ $\tilde{s}_L\ \tilde{s}_R\ \tilde{c}_L\ \tilde{c}_R$ $\tilde{t}_L\ \tilde{t}_R\ \tilde{b}_L\ \tilde{b}_R$
sleptons	0	$\tilde{e}_L\ \tilde{e}_R\ \tilde{\nu}_e$ $\tilde{\mu}_L\ \tilde{\mu}_R\ \tilde{\nu}_\mu$ $\tilde{\tau}_1\ \tilde{\tau}_2\ \tilde{\nu}_\tau$	$\tilde{e}_L\ \tilde{e}_R\ \tilde{\nu}_e$ $\tilde{\mu}_L\ \tilde{\mu}_R\ \tilde{\nu}_\mu$ $\tilde{\tau}_L\ \tilde{\tau}_R\ \tilde{\nu}_\tau$
neutralinos	1/2	$\tilde{\chi}_1^0\ \tilde{\chi}_2^0\ \tilde{\chi}_3^0\ \tilde{\chi}_4^0$	$\tilde{B}^0\ \tilde{W}^0\ \tilde{H}_u^0\ \tilde{H}_d^0$
charginos	1/2	$\tilde{\chi}_1^\pm\ \tilde{\chi}_2^\pm$	$\tilde{W}^\pm\ \tilde{H}_u^+\ \tilde{H}_d^-$
gluino	1/2	$\tilde{g}$	$\tilde{g}$
gravitino	3/2	$\tilde{G}$	$\tilde{G}$

Table 2.3: *Mass and Gauge eigenstates of the undiscovered particles of MSSM. Table taken from [42].*

one reason being that two doublets with different hypercharge (Y = 1, Y = -1) are needed in order to give mass to both up-type and down-type fermions. Such models are called Two Higgs Doublet Models (THDM) of type II, and is what we find in the MSSM.

Two complex Higgs doublets introduce eight degrees of freedom (*dof*) which after electroweak breaking are reduced to five as three are absorbed into the longitidunal components of the three massive vector fields. Hence, there are five physical Higgs bosons in the MSSM:

h, the lighter neutral CP-even scalar
H, the heavier neutral CP-even scaler
A, the neutral CP-odd scalar
$H^\pm$, the charged scalar and its antiparticle

At tree level in the MSSM the Higgs sector is determined by two parameters in addition to the parameters of the SM. These are normally taken to be the mass of the CP-odd scalar A and $\tan\beta$ which is the ratio between the vacuum expectation values of the two Higgs doublets ($\tan\beta = v_2/v_1$). At tree level we then have the following mass relations for the Higgs particles in the MSSM:

$$m_{H^\pm}^2 = m_A^2 + m_W^2 \tag{2.38}$$

$$m_{H,h}^2 = \frac{1}{2}\left(m_A^2 + m_Z^2 \mp \sqrt{(m_A^2+m_Z^2)^2 - 4m_A^2 m_Z^2 \cos^2 2\beta}\right) \tag{2.39}$$

It can be shown that these relations impose the following constraints $m_{H^\pm} \geq m_W$, $m_H \geq m_Z$, $m_A \geq m_h$ and finally $m_h \leq m_Z$. The latter constraint would have been ruled out already by the LEP2 results if not higher order radiative corrections would relax the constraint which is then extended to $m_h \leq 130\text{GeV}$. Nevertheless the constraint is a crucial and testable prediction of the theory and already one year after LHC startup one should be able to tell if the MSSM is possible or not.

Higher order corrections do not only change the constraint on the mass of the lightest Higgs boson, it also changes the mass splitting between the other Higgs bosons enabling decays of charged Higgs bosons not only to the lighest Higgs boson (h), but also to the heavier H. The most important parameters which enter in these loop corrections are the top-quark and stop-masses together with the soft trilinear coupling constant A_t and the supersymmetric Higgs parameter μ [25].

Charged Higgs boson production and decay

The dominant process for charged Higgs boson production is dependent on the mass of the charged Higgs boson, and below the top-quark mass the main production mode at the LHC will be $t\bar{t}$ production with subsequent decay of the top-quark into a charged Higgs boson:

$$gg \to t\bar{t}, \quad t \to H^+ b \tag{2.40}$$

The LHC will be the first top-quark factory producing about 10^7 $t\bar{t}$ pairs per year, hence if the charged Higgs boson is lighter then the top-quark mass it can be produced copiously.

Above the top-quark mass the main contribution to direct single charged Higgs boson production is through the so-called twin processes $gb \to H^\pm t$ $(2 \to 2)$ and $gg \to H^\pm tb$ $(2 \to 3)$. These processes are called twin processes since they correspond to two different approximations describing the same basic process in proton-proton collision, see Figure 2.4. Hence the two processes cannot be directly added without double-counting as explained in Reference [7].

Figure 2.5 shows the integrated cross-section as a function of mass for each of the different processes and the double-count term which has to be substracted when the $2 \to 2$ and $2 \to 3$ are used together. It is clear that in the transition region $m_{H^\pm} \sim m_t$ where the two processes are of similar size this mathing is of crucial importance in order to get the correct description of the physical process.

Like the production mechanism the main decay mode of the charged Higgs is also dependent on whether the mass is above or below the top-quark mass. Below the top-quark mass the main decay mode is into a tau lepton. For high $\tan\beta$ this is an almost exclusive decay mode, while for low $\tan\beta$ a few percent is left to decay modes involving neutral higgses (like Wh^0) or quark pairs like cs. See Figure 2.6.

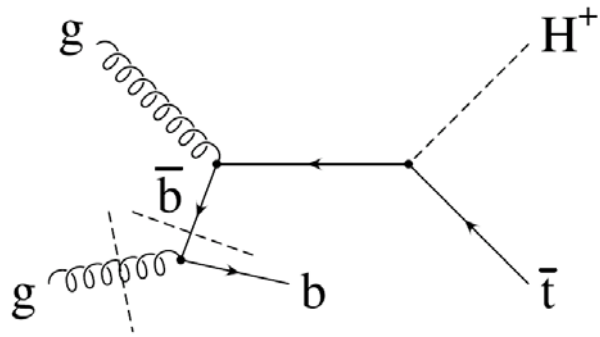

Figure 2.4: Feyman diagram depicting the two direct charged Higgs production modes at the LHC where the dashed line shows the difference between the $2 \rightarrow 2$ and $2 \rightarrow 3$ processes.

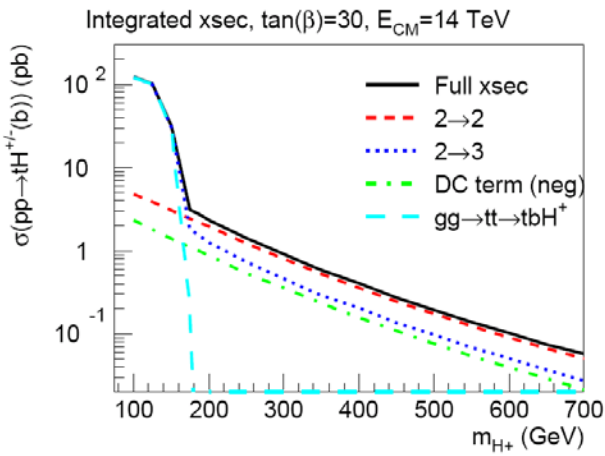

Figure 2.5: Integrated cross-section for charged Higgs production at the LHC for $\tan\beta = 30$. Shown are the $2 \rightarrow 2$ and $2 \rightarrow 3$ processes as well as their double-counting term. For low values of the charged Higgs mass the $2 \rightarrow 3$ process is well approximated by $t\bar{t}$ production and subsequent decay of top to charged Higgs and a b-quark. Figure taken from [6].

Once above the top-quark mass threshold the tb decay mode shows a rapid growth and soon becomes the dominant decay mode. Contrary to the tau lepton decay mode the tb mode is an almost exclusive decay mode for low $\tan\beta$ while for high values of $\tan\beta$ a few percent is still allowed to decay into the tau lepton mode. As we shall see in the next chapter these few percents are indeed sufficient to make the tau-lepton decay mode the main discovery mode also for high masses and high $\tan\beta$ since the tb decay mode suffers from large backgrounds, including combinatorial ones.

In this discussion we have assumed a heavy SUSY mass spectrum, and thus no $H^{\pm}$ decays into SUSY particles are allowed. Should such decay modes be

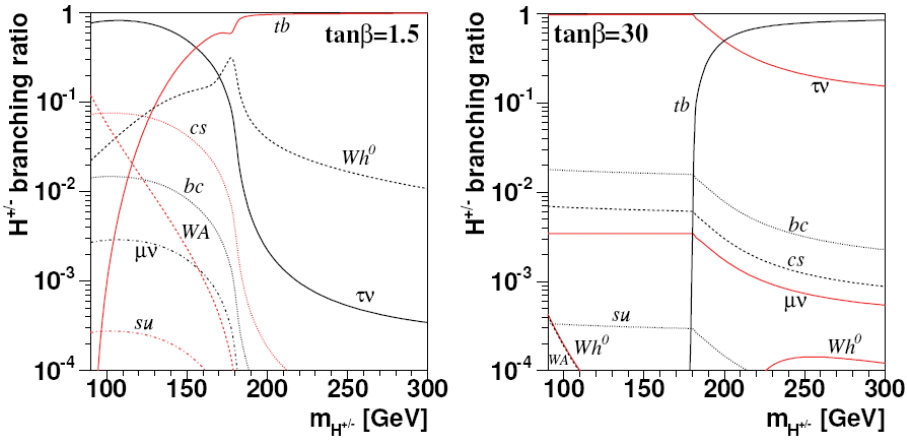

Figure 2.6: Charged Higgs decay modes shown as a function of mass and for two different values of $\tan\beta$. For low charged Higgs masses the tau lepton decay mode is the dominant one while for $m_{H^\pm} > m_t + m_b$ the tb decay mode soon becomes the dominant one. A maximal mixing SUSY scenario is used. Figure taken from [8].

open they would significantly change the situation, but this is beyond the scope of this thesis and will hence not be covered here.

3. Charged Higgs Boson Searches

A discovery of a charged Higgs boson would be an unambiguous sign of physics beyond the Standard Model and hence it is most interesting to study the present limits on the existence of a charged Higgs boson as well as the possibilities for charged Higgs detection at future colliders.

In this chapter current experimental contraints from both direct and indirect searches are presented in Section 3.1, while Monte Carlo simulation studies of the charged Higgs discovery potential for the future ATLAS detector are presented in Section 3.2.

3.1 Experimental Constraints

At the Large Electron Positron collider (LEP) at CERN the main production mode for charged Higgs bosons would have been pair production in the process $e^+e^- \rightarrow H^+H^-$. For the light charged Higgs boson masses accesible at LEP energies the main decay modes would be $H^\pm \rightarrow \tau\nu$ and $H^\pm \rightarrow cs$, and these were both investigated by the ALEPH collaboration. No excess of events over SM predictions were found and the resulting exclusion contour is shown in Figure 3.1. For all values of $\tan\beta$ charged Higgs masses below 79.3 GeV are excluded at a 95% confidence level, and for regions in the $\tan\beta$ parameter space where the branching fraction $H^\pm \rightarrow \tau\nu$ is large the exclusion limit can be extended up to 87.8 GeV.

At the TEVATRON the DØ experiment has conducted both indirect and direct searches for the existence of a charged Higgs boson. In the indirect search [2] a decrease in the rate $t\bar{t} \rightarrow W^+W^-b\bar{b}$ expected from the SM was searched for, while the direct search [1] looked for the $H^\pm \rightarrow \tau\nu$ decay mode. No evidence of signal was found, and the resulting limits on the charged Higgs mass is shown in Figure 3.2 as a function of $\tan\beta$. Regions of high and low $\tan\beta$ have been excluded where the direct search only contributes in the high $\tan\beta$ region since only here the branching ratio to tau-leptons is sufficiently high. For $\tan\beta < 1$ the indirect search yields a maximum exclusion of charged Higgs masses up to 120 GeV for very small values of $\tan\beta$. For high $\tan\beta$ the direct search helps extend the exclusion contour from the indirect search and $m_{H^\pm} < 75$ GeV is excluded for $\tan\beta > 32$. As the mass is increased the limit is weakened until $m_{H^\pm} = 150$ GeV, where no limit can be set.

CDF, which is DØ's companion experiment at the TEVATRON, has recently updated their charged Higgs search results [4], and in addition to ex-

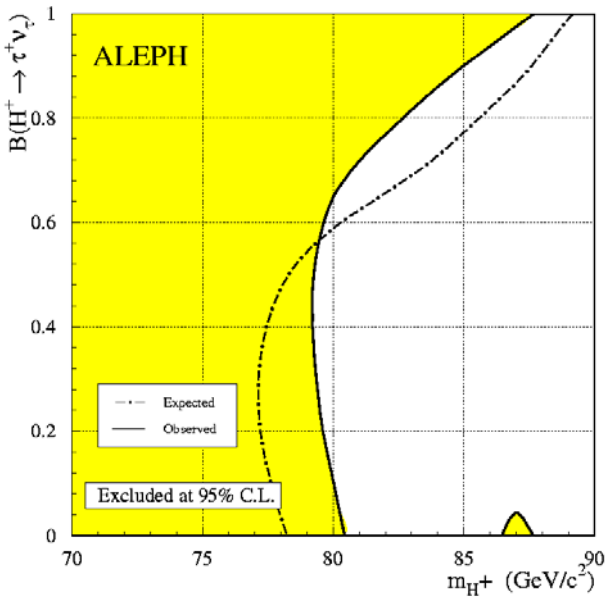

Figure 3.1: Limits on the charged Higgs mass at 95% confidence level from the ALEPH collaboration shown as a function of BR($H^{\pm} \to \tau\nu$). Figure taken from [33].

tending the excluded region in the $(\tan\beta, m_{H^{\pm}})$ plane, as shown in Figure 3.3, they also limit the branching ratio of $t \to H^{+}b$ to < 0.91 for 80 GeV $< m_{H^{\pm}} <$ 160 GeV. Figure 3.3 also shows the regions which are theoretically inaccesible due to a non-self-consistent Higgs sector $(\alpha(H^{\pm}tb) > 1)$.

Indirect constraints on the charged Higgs mass can also be inferred from measurements on branching ratios of meson decays. In particular the flavour changing neutral current $b \to s\gamma$, which is forbidden at tree level in the SM, is sensitive to the existence of a charged Higgs boson which would enter through radiative corrections. Hence any model extending the SM would have to deal with the very small rates measured, and this puts strong constraints on the charged Higgs mass. The combined result from the ALEPH, CLEO, BELLE and BABAR experiments sets a lower bound of 320 GeV at a 95% CL [55]. This result is significantly more constraining than any exclusion limit from the direct searches, however the result is much more model dependent. Anomalous couplings or sparticle loops in SUSY models may invalidate this result and hence indirect limits can not replace direct searches at present and future colliders.

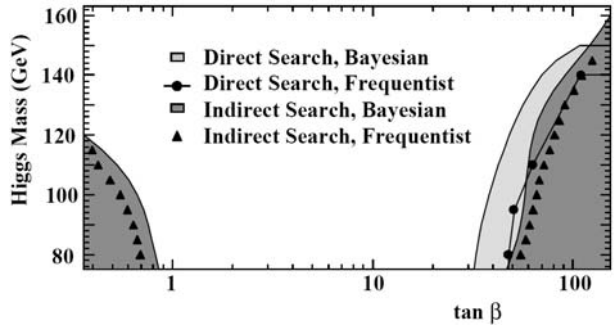

Figure 3.2: Limits on the charged Higgs mass from indirect and direct searches by the DØ experiment at the TEVATRON. The limits were obtained using data passing the multijet + $\not\!\!E_T$ trigger which comprises 62.2 ± 3.1 pb^{-1} of integrated luminosity. Figure taken from [1].

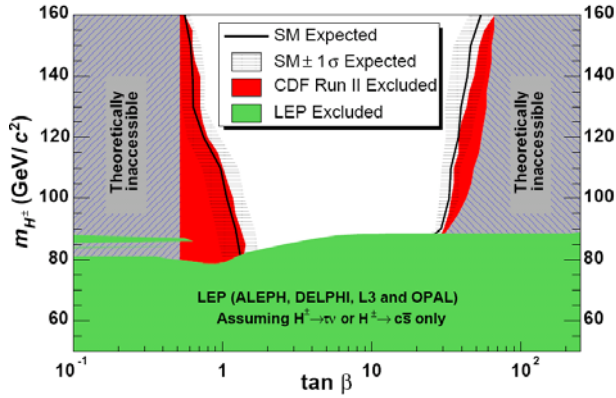

Figure 3.3: MSSM exclusion plot from the CDF collaboration obtained with 193 pb^{-1} data from the TEVATRON. Figure taken from [4].

3.2 Charged Higgs Boson Simulation Studies with ATLAS

As stated previously the LHC will become the world's first top-factory producing $\sim 10^7$ ttbar pairs every year. Hence, if kinematically possible ($m_{H^\pm} < m_t - m_b$), charged Higgs bosons may be copiously produced in top-quark decays. Furthermore the high energy of the LHC is also sufficient to give decent cross-sections ($\tan\beta$ dependent) for direct charged Higgs production (See Figure 2.5). Thus if the charged Higgs boson exists the ATLAS detector may become the first detector to observe it. Several sensitivity studies have been presented, searching for a charged Higgs boson signal both below and above the top-quark mass.

The current ATLAS sensitivity plot for a charged Higgs with SM decays only is shown in Figure 3.4. It shows that in the $H^\pm \to \tau\nu$ decay channel a discovery is possible up to $m_{H^\pm} \lesssim 160$ GeV independent of $\tan\beta$. The dis-

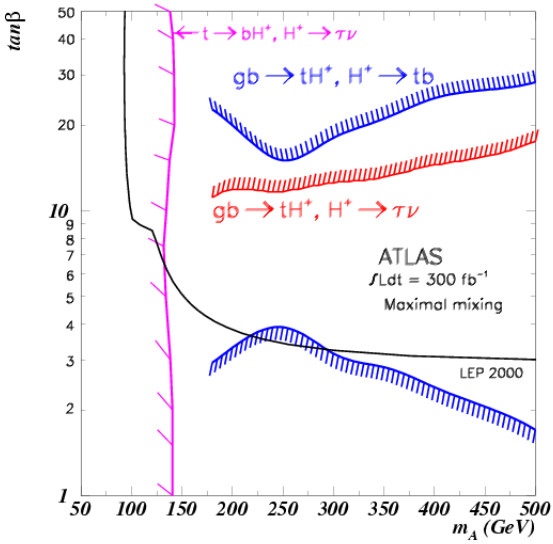

Figure 3.4: ATLAS charged Higgs discovery potential for 300 fb^{-1} in the decay channels $H^{\pm} \to \tau\nu$ [14, 37] and $H^{\pm} \to tb$ [9]. Note that m_A and $\tan\beta$ are chosen as the two free parameters determining the MSSM Higgs sector at three level. See Equation (2.39) for the relation between m_A and $m_{H^{\pm}}$.

covery contour in Figure 3.4 shows the discovery reach with 300 fb^{-1} which corresponds to 3 years of high luminosity running, but already 30 fb^{-1} will be sufficient for a discovery reach down to BR($t \to H^+ b$) $\sim$ 1% [14].

The region $m_{H^{\pm}} > m_t$ was at first thought to be difficult due to the large QCD background to the main decay mode $H^{\pm} \to tb$. Indeed this channel is a challenge, and the discovery contour as presented in Figure 3.4 [9] depends heavily on excellent b-tagging performance. The CMS collaboration has presented an updated study on this channel [40], which includes updated b-tagging, trigger acceptance and background estimation results, and concludes that the detection of the charged Higgs boson is not viable in this decay mode.

Despite the low branching ratio it turns out to be advantageous to search for the decay $H^{\pm} \to \tau\nu$ also in the high mass region. The tau-lepton signature enables an efficient background suppression and the tau polarization gives another handle for further suppression of the background, in particular $t\bar{t}$. As presented in [37] it is the size of the expected signal which is the limiting factor of the discovery reach in this channel.

The discovery contours as presented in Figure 3.4, contains only SM decay modes and do not cover the so-called intermediate $\tan\beta$ region defined by $m_{H^{\pm}} \gtrsim m_t$ and $4 \lesssim \tan\beta \lesssim 10$. This is related to a minimum in the $H^{\pm}tb$ vertex coupling for $\tan\beta \approx 7$, which enters not only in the main production mode $gb \to tH^+$, but also in the main SM decay mode $H^{\pm} \to tb$. The intermediate

$\tan\beta$ region is addressed in [31] where the SUSY $H^{\pm}$ decay to a chargino ($\tilde{\chi}^{\pm}$) and a neutralino ($\tilde{\chi}^{0}$) is studied. It is shown in [31] that the process $gb \rightarrow tH$ with $H^{\pm} \rightarrow \tilde{\chi}^{\pm}\tilde{\chi}^{0}$ can be discovered over the SM and MSSM background using three hard leptons and substantial amounts of missing energy as signature, and it is possible to cover a large fraction of the intermediate $\tan\beta$ region.

It is important to note that if the assumption of a SUSY spectrum much heavier then the charged Higgs boson is dropped, then the existing discovery contours as presented in Figure 3.4 do not hold. Hence even though is has been shown possible to cover the intermediate $\tan\beta$ region with a SUSY decay mode it is not directly complementary to discovery contours originating from SM decays of the charged Higgs boson. Thus, in an attempt to cover the intermediate $\tan\beta$ region with SM decays Paper I considers a part of the MSSM parameter space where the decay branching fraction $H^{\pm} \rightarrow W^{\pm}H^{0}$ is large. However, due to the large SM backgrounds a discovery of the charged Higgs boson in this channel is very challenging.

The studies outlined above are all performed using ATLAS fast simulation (ATLFAST) and furthermore, they all make use of composite reconstruction objects like b-jets, τ-jets, missing energy etc. Hence it is of great importance to study the impact of full simulation of the detector, and this is studied in Paper II, where ATLAS full simulation is used to study the charged Higgs boson signal in its most viable decay mode $H^{\pm} \rightarrow \tau\nu$. The study also features the matched event generation as explained in Section 2.3.1, which enables a continous scan over the $m_{H^{\pm}} \sim m_t$ region where the contributions from the two main production modes are of roughly equal size. Significant differences are found in this new study compared to the one presented in [37] but detailed investigation reveals that this is mainly caused by the more complete backgrounds used by the new study as compared to the old one. Still the new study is able to present a discovery contour close to the one presented in Figure 3.4. The striking result presented in Paper II is that the study for the first time is able to close the discovery gap between low ($m_{H^{\pm}} < mt$) and high ($m_{H^{\pm}} > mt$) charged Higgs boson masses with a SM decay mode.

4. The ATLAS experiment

In the following chapter the experimental environment of the simulation studies Paper I and II is presented. Section 4.1 presents the Large Hadron Collider (LHC) and Section 4.2 gives a brief overview of the ATLAS detector and technologies used in the different subdetectors. A more thorough introduction to the SemiConductor Tracker (SCT) of the Inner Detector (ID) is given in Chapter 5.

4.1 The Large Hadron Collider (LHC)

The Large Hadron Collider [38] is presently under construction at CERN (the European Organisation for Nuclear Research) which is situated outside Geneva, Switzerland. The LHC accelerator structure will be installed in the tunnel which previously hosted the Large Electron Positron collider (LEP). It measures 27 km in circumference and is situated 50 - 100m underground.

The LHC will provide $p-p$ and heavy-ion (e.g. Pb-Pb) collisions at 4 intereaction points. When operating in $p-p$ mode the energy available will reach the TeV scale ($\sqrt{s}$ = 14 TeV), about 7 times higher than the TEVATRON collider at Fermilab. At the design luminosity of $10^{34} cm^{-2} s^{-1}$ the counter rotating proton beams contain 2835 bunches of 10^{11} protons each, thus each beam stores an energy of 362 MJ. These beams are kept on their trajectories by 1232 main dipole magnets each one providing a magnetic field of 8.33 T.

At the design luminosity the LHC will have an interaction rate of 10^9 events/s. This results on average in 25 soft interactions at each bunch crossing, and about 1000 charged particles flying through the detectors in the pseudo-rapidity range $|\eta| < 2.5$[1]. These 25 soft interactions are referred to as the pile-up and have had a major impact on the design of the different detectors.

Four large-scale experiments will be running at the LHC. ATLAS [11] and CMS [20] are the two multipurpose detectors for $p-p$ collisions and they allow for precision measurement of electrons, muons taus, jets, b-jets and more. The LHCb [39] is an experiment dedicated to the physics of B-hadrons, and unlike ATLAS and CMS which have almost full spherical coverage the LHCb detector is a single arm forward spectrometer to exploit the fact that

[1]Pseudo-rapidity is defined as $\eta = -\ln \cot\theta/2$ where θ is the polar angle of produced particle with respect to the beam pipe.

at the LHC B-hadrons are predominantly produced in the forward direction. As mentioned above the LHC also features heavy ion collisions and the ALICE [5] experiment is optimised to study these collisions and the behaviour of nuclear matter at high densities and energies.

With the current installation rate the LHC is scheduled for first test runs at the end of 2007. During these first runs the accelerator will circulate 450 GeV proton beams, i.e. the same energy is the injection energy from the Super Proton Synchrotron (SPS) which is used to pre-accelerate the protons. Normal operation at 7 TeV beam energy is foreseen to 2008.

4.2 The ATLAS Detector

ATLAS (short for A Toriodal Lhc ApparatuS) is the largest of the four detectors operating at LHC. Its physical size is enormous, and its cylindrical shape measures 44 meters in length and 11 meters in radius. Its total weight is $\sim$ 7000 tons. ATLAS is a general purpose $p-p$ detector designed to exploit the full physics potential of the LHC.

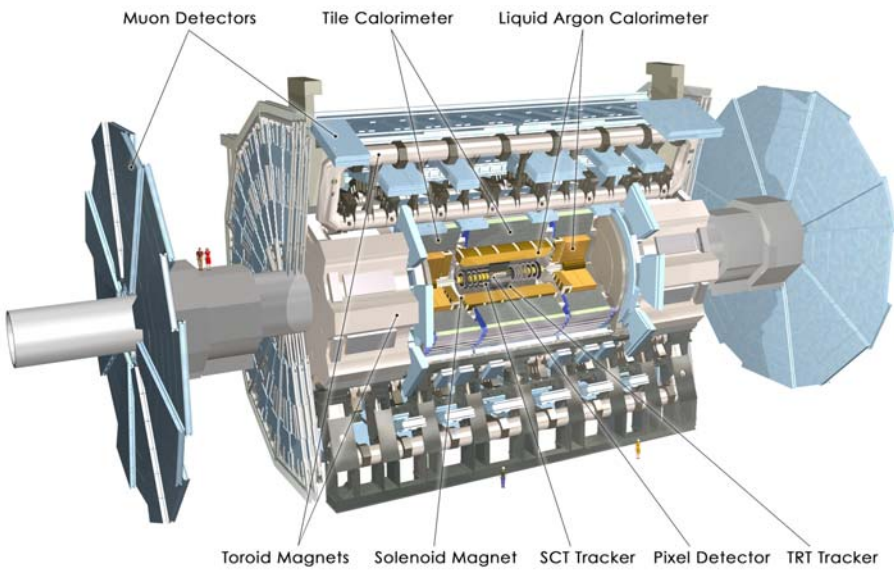

Figure 4.1: Schematic view of the ATLAS detector. The scale is indicated by the human figures shown on the left hand side.

The origin of mass at the electroweak scale is one of many fields of interest for the ATLAS community. The detector optimization is therefore guided by physics issues such as sensitivity to the largest possible Higgs mass range. The search strategies for finding the SM Higgs boson are well known from theoretical work, and in order to cover the full mass range above the present

LEP limit of 80 GeV the ATLAS detector has to be sensitive to the following processes (ℓ = e or μ):

$h \rightarrow b\bar{b}$	$80 < m_h < 100$ GeV
$h \rightarrow \gamma\gamma$	$90 < m_h < 150$ GeV
$h \rightarrow ZZ^* \rightarrow 4\ell^{\pm}$	$130 < m_h < 2m_Z$
$h \rightarrow ZZ \rightarrow 4\ell^{\pm}, 2\ell^{\pm}2\nu$	$m_h > 2m_Z$
$h \rightarrow WW, ZZ \rightarrow \ell^{\pm}\nu 2jets, 2\ell^{\pm}2jets$	$m_h \rightarrow 1TeV$

Thus, in order to maximise the discovery potential for finding the SM Higgs boson in addition to being sensitive to all kinds of new phenomena which might occur in $p-p$ collisions at multi-TeV energies, the ATLAS detector needs excellent resolution for measurements of leptons, jets and missing transverse energy. This is achieved by combining various detector subsystems as seen in Figure 4.1 and detailed information about the detector construction and expected performance can be found in [11]. Below a short summary of each subdetector system is given based in the information from [11].

4.2.1 Inner Detector

The Inner Detector (ID) is the subdetector closest to the beam-pipe, and is stored within a cylindrical superconducting solenoid which measures 7 metres in length and has a radius of 1.15 metres. The solonoid provides a magnetic field of 2T which bends the charged particle tracks and enables precision measurements of the particle momentum. Mechanically the ID consists of three units, one central barrel part and two end caps. The barrel part extends over -80cm $< z <$ 80cm while the two identical end caps cover up the rest of the cylindrical cavity.

The ID is made up from three subsystems and closest to the beam pipe we find the Pixel detector. The Pixel detector consists of semiconductor pixel detectors mounted on 3 barrel layers (at radii $\sim$ 4,10 and 13cm) and 5 end cap disks (between radii of 11 and 20cm). The Pixel detector has to cope with high levels of radiation and the readout chips for the 140 million channels have to withstand 300 kGy of ionising radiation and over $5\times\ 10^{14}$ neutrons per cm^2 over ten years. Due to expected radation damage the mechanical design of the ID allows for the innermost barrel layer (B-layer) to be replaced when needed.

Outside the Pixel detector the SemiConductor Tracker (SCT) is positioned. The barrel SCT uses eight layers (four space points) of silicon microstrip detectors to provide precision points in the Rϕ and z coordinates, where a small stereo angle between layers is used to obtain the z measurement. In total the detector contains 61 m^2 of silicon detectors, with more then 6.2 million readout channels. The spatial resolution is 16 μm in Rϕ and 580 μm in z, per detector module containing one Rϕ and one stereo measurement. Tracks can

be distinguished if seperated more than $\sim 200\ \mu$m. More about the SCT detector in Chapter 5.

The outermost subsystem of the ID is the Transition Radiation Tracker (TRT) which consists of straw detectors which are well suited for a LHC environment due to their small diameter (4mm) and hence fast response. The technique is radiation hard and allows for a large number of measurements, typically 36, per track. By employing Xenon gas to the straw tubes the detector also becomes capable of detecting transition-radiation photons created in the radiator between the straws and hence the TRT is also able to do electron identification.

The overall layout of the ID provides full tracking coverage over $|\eta| < 2.5$, including impact parameter measurements and vertexing for heavy-flavour and τ tagging. The relative precision of the different measurements from the different subsystems is well matched, so that no single measurement dominates the momentum resolution. This implies that the overall performance is robust.

4.2.2 Calorimeters

The ATLAS calorimeter system consists of an electromagnetic (EM) calorimeter and hadron calorimeters. The EM calorimeter is situated outside the Inner Detector and goes out to a radial range of 2.25 metres, covering the pseudorapidity region $|\eta| < 3.2$. Outside the EM calorimeter we find the Hadron Calorimeters extending to a radius of 4.25 metres. They cover the range $|\eta| < 4.9$ using different techniques.

The EM calorimeter is a lead LAr detector with accordion-shaped Kapton electrodes and lead absorbers over its full coverage. The region devoted to precision physics ($|\eta| < 2.5$) is segmented into three logitudinal sections. The innermost one, strip section, acts as a preshower detector, enhancing particle identification ($\gamma/\pi^0, e/\pi, etc$) and provides a precise position measurement in η. The second, and middle, section is segmented into square towers of size $\Delta\eta \times \Delta\phi = 0.025 \times 0.025$ while the back section has a granularity of 0.05 in η.

The barrel section of the Hadronic calorimeters ($|\eta| < 1.5$) is also called the tile calorimeter due to the technique used. It is a sampling calorimeter using iron as absorber and scintillating tiles as the active medium which are read out by two seperate photomultipliers. For the range $1.5 < |\eta| < 4.9$ a more radiation hard technique was needed and intrinsically radiation hard LAr detectors were chosen. The liquid-argon Hadronic End cap Calorimeters (HEC) consists of two independent wheels of outer radius 2.03 m.

The final part of the hadronic calorimeters is the liquid-argon forward calorimeter (FCAL). This is placed next to the beam pipe and is a particularly challenging detector due to the high level of radiation it has to cope with. In

ATLAS the FCAL is mounted inside the end cap cryostat and its front face is 4.7 m from the interaction point.

4.2.3 Muon Spectrometer

The outermost part of the ATLAS detector is the muon spectrometer. High muon momentum resolution is acheived with three stations of high-precision tracking chambers, and multiple scattering is reduced due to the light and open structure. In the barrel the chambers are positioned in order to determine the momentum from the curvature (sagitta) of the trajectories while the end caps have the chambers arranged to determine the momentum from a point-angle measurement.

Over most of the η range a high-precision measurement of the track coordinates in the principal bending direction of the magnetic field is provided by Monitored Drift Tubes (MDTs). At large pseudorapidities and close to the interaction point, Cathode Strip Chambers (CSCs) with higher granularity are used in the innermost plane over $2 < |\eta| < 2.7$, to withstand the demanding rate and background conditions.

The Muon Spectrometer is instrumented with trigger chambers (Resistive Plate Chambers (RPCs) in the barrel region and Thin Gap Chambers (TGCs) in the end caps) which serve a threefold purpose. They have a time resolution better than the LHC bunch spacing of 25ns and thus provides bunch identification. Furthermore they provide a trigger with well-defined P_T cut-offs in moderate magnetic fields and their 'ϕ-strips' are orthogonal to the MDT wires and provide the second-coordinate measurement.

4.2.4 Magnet System

The magnet system is best shown on Figure 4.1 and it is an arrangement of a Central Solenoid (CS), providing the inner detector with magnetic field, surrounded by three large air-core toroids generating the magnetic field for the muon spectrometer. The three toroids are divided into one Barrel Toroid (BT) and two End Cap Toroids (ECT). The overall sizes of the magnet system are 26 m in length and 20 m in diameter.

The CS extends over a length of 5.3 m and has a bore of 2.4 m. It provides a central field of 2 T with a peak magnetic field of 2.6 T at the superconductor itself. The CS design has been of high importance and due to its position in front of the EM calorimeter the CS is designed to be as thin as possible. This is done in a comprimize between best possible calorimeter performance without sacrifying the operational safety and reliability.

The BT is a large construction with its 25.3 metres of length and 20.1 metres of outer diameter. It consists of eight coils assembled radially and symmetrically around the beam axis. The coils are of a flat racetrack type with two double-pancake windings made of 20.5 kA aluminium-stabilised NbTi super-

conductor, and the windings are housed in an aluminium alloy casing. These coils provide a peak magnetic field of 3.9 T with a bending power of 2 to 6 Tm.

The ECT are also made up from eight racetrack, double-pancake coils in an aluminium alloy housing, which in turn are all housed in one large crystat. However these coils are rotated 22.5° with respect to the BT coils in order to provide radial overlap and to optimise the bending power in the interface regions of both coil systems. The ECTs provide a peak magnetic field of 4.1 T and a bending power of 4 to 8 Tm. They measure 5 m in length and have an outer diameter of 10.7 m. The ECTs are inserted in the barrel toroid at each end and line up with the CS.

4.2.5 Trigger and Data-Acquisition System

The ATLAS trigger and data-acquisition (DAQ) system is a three level system where each level provides an online refinement of the decisions made at the previous level. Starting from the initial 40 MHz (interaction rate of $\sim 10^9$ Hz at the luminosity $10^{34} cm^{-2} s^{-1}$), the rate of selected events must be reduced to ~ 100 Hz for permanent storage. This requires an overall rejection factor of 10^7 and is obtained by the two trigger levels and the final event filter. The level-1 (LVL1) trigger makes the intial selection and reduces the number of interesting events down to 100 kHz. This will be further reduced by the level-2 (LVL2) trigger which takes the number of events down with a factor of 2 before the Event Filter makes the final selection and 100 Hz, or 100 MB/s, will be written to permanent storage.

The LVL1 trigger makes its initial selection based on reduced-granularity information from a subset of detectors. This includes identification of high transverse-momentum (high-p_T) muons using the muon trigger chambers and also reduced-granularity information from the calorimeters. The calorimeter trigger is looking for high p_T electrons and photons, jets and τ-leptons decaying into hadrons as well as large missing and total transverse energies. The time taken from an event until the LVL1 decision is taken is required to be less than 2.5 μs and in order to achieve this the LVL1 trigger is implemented as a system of purpose-built hardware processors. Awaiting the decision the data from the detectors is stored in pipelines placed on or close to the detectors.

The LVL2 trigger makes use of 'region of interest' (RoI) information provided by the LVL1 trigger. (This includes information on position (η and ϕ) of candidate objects among others.) Using this information the LVL2 trigger selectively accesses the data only moving the data necessary to take the LVL2 decision. The LVL2 trigger has access to all data, with full precision and granularity, and much of its rejection power comes from recalculating the decisions taken by LVL1, but now with full granularity. In some situastions the LVL2 trigger also makes use of increased thresholds and additional requirements in order to significantly reduce the rate, this being the case for jets.

The final stage in the event selection process is the Event Filter (EF). It will employ offline algorithms and methods, adapted to the online environment, and use the most up to date calibration and alignment information and the magnetic field map. The EF will make the final decision, in which the output rate should be reduced to 100Hz, and these physics events will be written to mass storage for subsequent full offline analysis.

5. The ATLAS SemiConductor Tracker

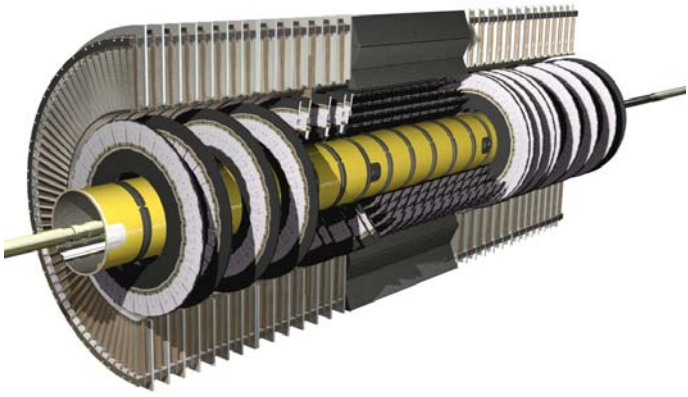

Figure 5.1: The SCT detector with its 4 central barrels and 9 disks in each end cap seen inside the TRT. The yellow tube is the housing for the Pixel detector.

The ATLAS SemiConductor Tracker (SCT) as situated inside the TRT is shown on Figure 5.1. It consists of four concentric barrels (3,4,5 and 6[1]) and two end caps, A and C, with nine disks each (1 to 9, counted from the interaction point). Each barrel and disk is equipped with silicon detector modules as discussed in Section 4.2.1. The barrels are fully populated with modules thus giving a hermetical ϕ coverage, while the disks have 1,2 or 3 rings of modules depending on their distance from the interaction point.

Starting with the construction and testing of SCT barrel modules and ending with the design and implementation of the power supply detector control system, a large fraction of this thesis has been devoted to the SCT detector. The work related to the barrel modules is summarized in Paper III and an introduction to this work is given in Sections 5.1 and 5.2.

Section 5.3 gives an introduction to the SCT detector structures as they are important for the work presented in the later sections of the present chapter. The section also gives a summary of the testing and evaluation of radiation hard humidity sensors mounted on the SCT detector.

With its size and complexecity the SCT detector requires a highly advanced Detector Control System (DCS). For this thesis the design and implementation

[1]Barrel 0,1 and 2 are the three pixel barrels

of a distributed power supply control system for the SCT detector is presented. A general introduction to the SCT DCS is thus given in Section 5.4, while a detailed explanation of the power supply part is given in Paper IV. Results obtained with the system during macro-assembly and later integration are given in Paper V.

5.1 The SCT Barrel Module

The SCT barrel detector module [3] as seen on Figure 5.1 consists of 4 silicon microstrip sensors which measure $(63.96 \times 63.56 \times 0.285)\text{mm}^3$ each. Two sensor pairs are mounted back-to-back on each side of the module baseboard, which provides the thermal and mechanical structure for the module. The readout hybrid, which is placed near the center of the module, bridges over the sensors and is held clear of their surface by feet that are glued to the Beryllium facings of the baseboard.

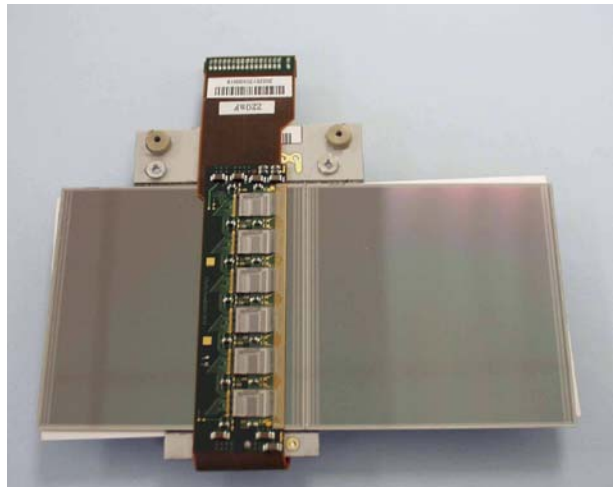

Figure 5.2: The SCT barrel module as built from 4 silicon microstrip sensors, one baseboard and one hybrid with readout electronics which brigdes over the sensor surfaces.

Each silicon sensor is equipped with 768 readout strips (80μm pitch) and each strip is bonded together with the corresponding strip of the adjacent sensor. Together they form a 12cm readout strip which is bonded to the readout electronics through one common bounding. A precision spacepoint measurement is enabled by having the two layers of sensors rotated with respect to each other by 40 mrad. As the barrel module is mounted with the strips running along the z-direction this gives a precision of 17μm in the $r\phi$-plane and 580μm in the z-direction when combining measurements from both module layers.

5.1.1 Microstrip Sensor and Baseboard

The design of the barrel module is the result of several years of R&D where not only the high demands related to the LHC environment had to be met, but also costs and production yield were important aspects. Below a short description is given of the most important design considerations for the microstrip sensor:

- **A radiation hard** sensor is a prerequisite to be able to survive the harsh environment at the LHC. The innermost part of the SCT detector should be able to withstand doses of$\sim 2 \times 10^{14}$ 1 MeV equivalent neutrons per cm^2. Such a high dose has severe consequences for the sensor and among other things it will cause a type conversion where the n-type bulk becomes p-type moving the initial p-n junction towards the sensors' back surface. It is thus foreseen that bias voltages of up to 450V will be required after 10 years of LHC running to maintain the performance of the detectors.
- **An AC coupled single sided p-in-n design** proved to be the detector design type which combined high performance with the best properties for mass production and production yield.
- **The sensor thickness** is of crucial importance due to the SCT detector's position in front of all the calorimeters. The biggest contribution to the radiation length caused by the SCT detector comes from the silicon sensors which should be kept as thin as possible. On the other hand a thicker sensor produces a higher signal giving rise to a larger signal to noise ratio. As a compromise a thickness of 285 μm was chosen for the microstrip sensor.
- **Sensor dimensions** and strip pitch is guided by requirements on granularity and noise performance in the SCT. The desired momentum resolution and occupancy in physics events is obtained with 80 μm strip pitch, and a stereo angle of 40 mrad. The specified limit for the noise-occupancy is 5×10^{-4} per channel and this limits the physical size of the detector to about 12 cm for a readout strip. Hence each sensor is constructed $\sim$ 6 cm long and the strips of two sensors on each side is joined by wirebonds.

The foreseen high voltages needed for sensor depletion after several years of running will result in a total leakage current of ~ 0.5mA for a single sensor operated at 450V and $-7^{\circ}C$. The leakage current is highly dependent on temperature (roughly doubles every $7^{\circ}C$) and combined with the heat generated by the readout electronics an in-plane thermal conductivity beyond the one of silicon alone is needed. This is provided by having a baseboard made of a 380μm thick anisotropic thermal pyrolytic graphite (TPG) sheet encapsulated in epoxy and sandwiched between the two layers of sensors. The baseboard is equipped with BeO facings (seen as the white surfaces extending outside the sensors on Figure 5.2) on which the hybrid feet are mounted. The larger BeO facing has two holes that are aligned with similar holes in the graphite substrate which are used for mounting the barrel module to the cooling interface of the barrel support structure.

Sensor biasing

The SCT module is reverse biased and the bias contact to the back surface of the silicon sensors is through areas where the epoxy encapsulating the TPG is removed and electrically conduction epoxy is applied during the attachment process of the silicon sensors. The TPG is electrically conducting and the bias connectivity is completed with small holes filled with electrically conducting epoxy under each beryllium facing. The hole through the beryllium facing has a gold plated surrounding which is wirebonded to the HV line of the above mounted hybrid.

5.1.2 Readout Electronics

Each SCT module comprises 1536 strips, and as the SCT detector consists of 4088 SCT modules about 6.3 million strips/channels have to be read out every 25ns. Given the size and complexity of the system, data reduction is of crucial importance and solved by having a binary readout scheme. A binary readout system significantly reduces the amount of data as no information about pulse height, length or energy deposition is read out from the system.

The 1536 strips of the SCT module are read out by 12 128-channel ASICs which are mounted onto the hybrid circuit. The ASICs are single chip implementations of a binary readout using the radiation hard BICMOS DMILL technology, and are referred to as the ABCD3TA ASIC [17]. Each chip contains all functions required for processing signals from the 128 strips and transmitting the data off the detector module in the SCT.

A schematic representation of the ABCD3TA ASIC is shown in Figure 5.3. In order to ensure a detection efficiency of above 99% the signal from the strips need to be discriminated at the level of 1 fC. At the same time the noise occupancy is required to be kept below 5×10^{-4}. Below a description of the main ASIC functionalities is given starting with from the collected charge ending with the chip readout:

1. Charge integration and shaping of the signal is performed by the front end preamplifier-shaper circuit which has a nominal gain of 50mV/fC. In addition to being connected to the silicon strip the preamplifier-shaper is also connected to a circuitry that can inject a known charge in the range from 0 to 16 fC thus faking a real strip readout. This circuitry is important in order to measure the analogue parameters of the front end electronics.
2. From the preamplifier-shaper the signal is passed to a discriminator which compares the signal to a threshold voltage. A common threshold for all 128 channels is set by an 8 bit DAC (spanning the range 0-640 mV), but in order to adjust for individual channel variations there is an additional 4 bit TrimDAC for each channel which can be set for channel threshold corrections.
3. In the input register the binary output from the discriminator output is latched to a pulse of well defined width. Depending on the selected detec-

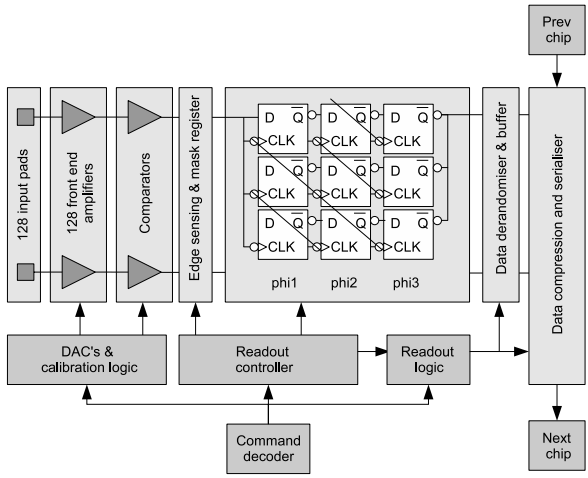

Figure 5.3: Block diagram of the ABCD3TA readout chip. Figure taken from [45].

tion mode either a single 1 (edge detection mode) is written to the pipeline input regardless of the response time of the discriminator, or multiple 1s are written to the pipeline for each clock cycle in which the discriminator output is on (level detect mode).

4. Given a L1 trigger latency of 3.3 μs a 132 cells deep pipeline clocked at 40MHz is needed. This is realised as a multiplexed FIFO circuit with 12×12 cells controlled by 12 non-overlapping clock signals. All data is propagated through the pipeline and if a L1 decision arrives when an event has reached the end of the pipeline then all 128 channels are read out both for the triggered event but also for the neighbooring events in time.
5. Bit values for three consequtive time bins are read out and put into a 24 bit deep readout buffer for processing. Once the flag signifying data in the readout buffer has been set the data compression logic converts the data from 3 128 bit words into 128 3 bit words and starts to match each 3 bit word with the required hit pattern (01X of X1X during normal operation). If a match is found the hit pattern from that channel is sent to the readout circuitry for transmission.

On the hybrid the readout from the 6 chips on each side are read out through daisy chaining where 1 chip serves as the master sending tokens to the other chips to organize the readout sequence. Each chip can be programmed to be either a Master, a Slave or End chip and in case of chip failure the chip is programmed to use one of the many redundant connections on the hybrid to pass its data to the next chip in the chain. In the event of a failed Master chip the data from one module side can be routed around the module and read out by the master chip on the opposite side. This design ensures a minimum of lost channel in the case of damage to a readout chip.

ASICs powering

As the ASIC is built from one analogue and one digital circuit, two power supply voltages are needed to operate the chip. The analogue voltage Vcc is set to 3.5V while the digital Vdd voltage is 4.0V. The 4.0V chosen for the digital power is lower than the nominal 5V for a DMILL technology, and this is done to keep the power consumption of the module as low as possible. Deviations from the chosen values by up to 200mV should not influence on the chip's performance.

5.2 SCT Module Production

The construction of 4088 detector modules needed for the SCT construction is today completed and the detector modules are mounted on barrels or disks and available at CERN. While some construction tasks like the mounting of modules to their support structures are hard to distribute, the production of modules is of modular nature and permits smaller groups to take on significant responsibilities. The SCT barrel modules where thus produced by several institutes/groups around the world and among them the Scandinavian (SCAND) cluster, a joint effort between University of Bergen, University of Oslo and Uppsala University. In total the SCAND cluster succesfully delivered some 320 modules to the barrel SCT and the results of the production are given in Paper III.

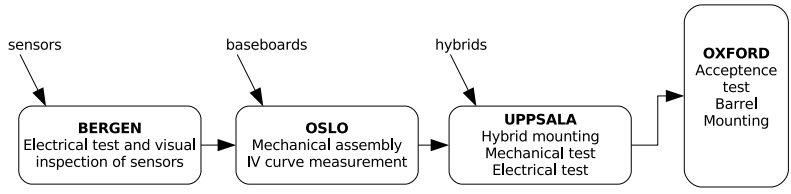

Figure 5.4: The SCAND production chain.

Figure 5.4 shows how the construction work of the barrel module was shared between the institutes which made up the SCAND cluster. Silicon sensors made by Hammamatsu Photonics were first visually inspected and tested for IV performance at the University of Bergen. The tested sensors were sent to University of Oslo where 4 sensors with equal IV performance were mounted on a TPG baseboard that were fabricated at CERN. Sensors were matched according to their IV performance since the total production of SCT barrel modules included a 10% surplus to account for production mistakes and to provide spare modules. Sensors with non-optimal IV characteristics were thus put together, making that module a more likely spare candidate.

The finished detector-baseboard sandwich (called baseboard assembly) was once more tested for its IV performance before being shipped to Uppsala.

Upon arrival in Uppsala the baseboard assemblies were first subject to a metrology test where their geometrical properties were measured. Also, all hybrids that were provided to the cluster from collaborators in Japan and USA were tested upon reception. The unmounted hybrids were clamped onto a water cooled aluminium block inside a custom made test box, and a test sequence known as a Confirmation test was run (For more details about the test see [47]). The Confirmation test aims to verify if the hybrid's, or module's, performance has detoriated as a result of handling or shipping, and was used to determine the number of bad readout channels on the hybrid. Occasionally hybrids with high a high number of defective channels were received (> 10), and as the bonding process increases the risk for having more defective channels those hybrids were typically paired with baseboard assemblies with less good IV characteristiscs.

If the baseboard assembly and hybrid passed the reception tests, the hybrid was mounted using special jigs which folded the hybrid around the sensors without touching their surfaces. Once the hybrid was wirebounded to the sensors the module was taken through a series of Quality Assurance (QA) tests. The results were compared against the specifications for an electrically good module and the module was classified accordingly. Both in Uppsala and Bergen test setups were ready for QA tests [44], but as the test capacity in Uppsala was large enough to cope with the entire production, personel from Bergen were sent to Uppsala to assist with the testing.

As earlier discussed the radiation damage to the silicon sensors will be significant after 10 years of ATLAS operation, but the level of damage will vary with the radii from the interaction point at which the module is positioned. It is expected that barrel 3 modules will have to be operated at a ~ 450V bias, while barrel 6 modules will do with ~ 250V after irradiation. This is reflected in Table 5.1 where different IV requirements are set for modules close to the interaction point, or the ones to be mounted on barrel 5/6 only.

The production of modules by the SCAND cluster is today finished and the modules are already installed in ATLAS as a part of the SCT barrel. A summary of the production including electrical testing and discussions about defective ASICs is presented in Paper III.

5.3 The SCT Detector Structures and Monitoring Sensors

The silicon detector modules in the SCT are mounted on carbon fibre support structures. The SCT barrel is made up of 4 concentric barrels with flanges at the ends to connect them to each other, and the SCT end caps consists of 9 carbon fibre wheels which have one, two or three rings for module attachment

Measured Quantity	Limit for an electrically good module
Avarage noise occupancy per channel at 1 fC threshold (Both warm and cold test)	5×10^{-4}
Number of bad readout channels per module (Both warm and cold test)	≤ 15(1% of total)
Number of consecutive bad readout channel on one module	≤ 7
Strip micro-discharge	None to 500V bias (any barrel) None to 350V bias (barrel 5/6 only)
Leakage current at 20°C and 500V bias if no micro-discharge	$< 4\mu$A

Table 5.1: *The electrical specifications of the assembled SCT barrel module.*

(depending on the position of the disk). The support structure is of utmost importance to the SCT detector. It should have a minimum of material thickness, both in terms of radiation and absorption length, and at the same time have excellent thermal and humidity stability.

All four SCT barrels were assembled at the Oxford macro assembly site [54] where modules were mounted onto the support structures by a custom robot [43]. Figure 5.5 shows the details of how the modules are fixed to the support structure. The horizontal tubes seen on the figure are the cooling pipes for the evaporative cooling neded to cool the modules during operation. Before each module is mounted and clamped onto the cooling block, situated under the larger BeO facing, a layer of thermal grease is spread onto the cooling block to ensure good thermal contact.

Within the SCT barrel each cooling half loop services two rows of modules (2×12 modules) and each cooling loop consists of two cooling half loops. The two inner rows of the cooling loop end in a common outlet manifold, while the two outer rows are the inlets connected directly to the capilliaries. At the end of each outlet row a pair of thermistors are mounted to monitor the temperature of the cooling stave and to serve as input to the power supply interlock system which will prevent the modules from overheating. For the SCT endcap the cooling pipe is organised such that each half loop services one octant of the disk independently of the number of module rings. As for the barrel two half loops make up one cooling loop with a common outlet and which then services one quadrant of the disk.

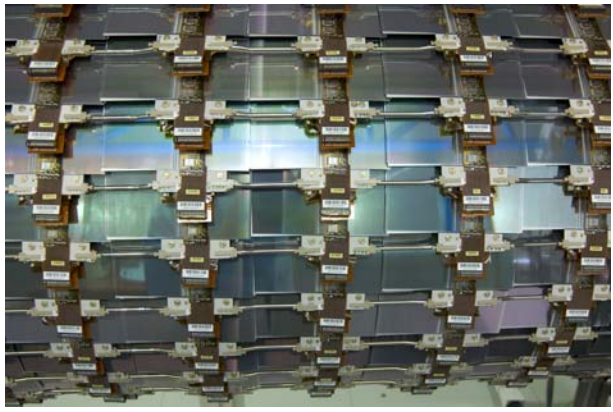

Figure 5.5: SCT barrel modules mounted on barrel 3. Each module is mounted at an angle of 10° with respect to the tangent of the barrel in order to minimize the impact of the 2T magnetic field on the drift charges. The horizontal pipes are the CuNi cooling pipes of the evaporative cooling system.

Figure 5.6: SCT barrel 4 being prepared for shipping to CERN.

Figure 5.6 shows barrel 4 when fully populated with its 480 modules. The individual barrels and disks are today installed in the SCT barrel and SCT endcaps which are housed inside a thermal enclosure. The thermal enclosure acts as a thermal shield between the SCT detector, which operatates at $-7°$C, and the TRT which operates at $+20°$C.

The extreme operating conditions of the SCT detector requires close monitoring of all environmental parameters to ensure the performance and safety of the detector. The individual barrels and disks as well as all inlets, outlets and the thermal enclosure itself are thus equipped with almost a thousand sensors that provide information on the humidity, temperature and pressure. The monitoring and control of all these parameters is maintained by the SCT Detector Control System (DCS) which is presented in the Section 5.4.

5.3.1 Humidity Sensors for the SCT

Run preparations for the SCT detector involves cooling the detector down from room temperature to its sub zero working temperature. During this process it is most important to know the dew point inside the cooled detector volume to prevent condensation of water vapor on the detector surfaces. Humidity sensor readings are important inputs to the dew point calculation and for the SCT a radiation hard sensor that has a range down to 0% RH, preferably with a linear response, was needed. The only sensor on the market that the met the specifications is a cellulose crystallite strain gauge sensor manufactured by Hygrometrix Inc..

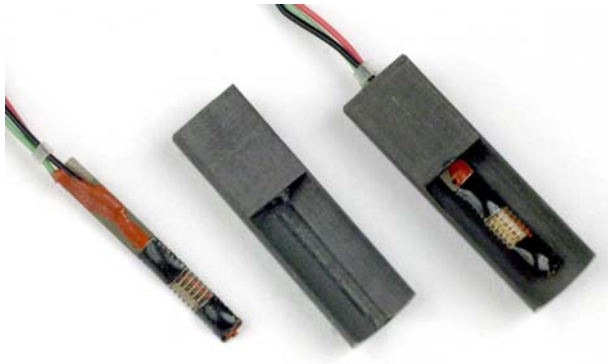

Figure 5.7: On the left a humidity sensor as delivered by Hygrometrix Inc., in the middle a carbon fibre housing and on the right the humidity sensor package.

The type XN1018 sensors from the Xeritron^{TM} series from Hygrometrix (Figure 5.7) have two resistors R1 and R2 that both change with humidity. The ratio between these resistances is unique for each sensor and the relation

$$RH = a \times \frac{R1}{R1+R2} - b, \tag{5.1}$$

determines the relative humidity. The ratio is however also sensitive to temperature and the calibration of the sensors thus involves two steps:

1. The temperature dependence of the resistors is determined. This is done with a set of sensors and later the calibration constant derived is applied to all resistors.
2. The constants a and b that are unique for each individual sensor are determined for each sensor prior to installation in the SCT.

Testing and calibration of all SCT humidity sensors was carried out at Uppsala University where the testbox originally made for the testing of SCT detector modules was reused for the purpose. Four Xeritron sensors were placed in the environmental chamber that was flushed with dry nitrogen gas for 32 hours prior to and during the measurement to maintain a stable environment close to 0%RH. Measurements were made for different temperatures and Figure 5.8 shows the sensors' behaviour as the temperature in the chamber was

changed. From the results one can estimate that an increase in temperature by 1°C would equal to an increase in the humidity reading of 0.3%RH. The temperature dependence was then determined by straight line fitting to each resistors temperature dependency and the correction formula [15].

$$R' = R - [1.6 + R \cdot 0.0012] \cdot T \tag{5.2}$$

was derived. Here R is the measured value and R' is the corrected one. The correction formula is used to correct both $R1$ and $R2$ resistances.

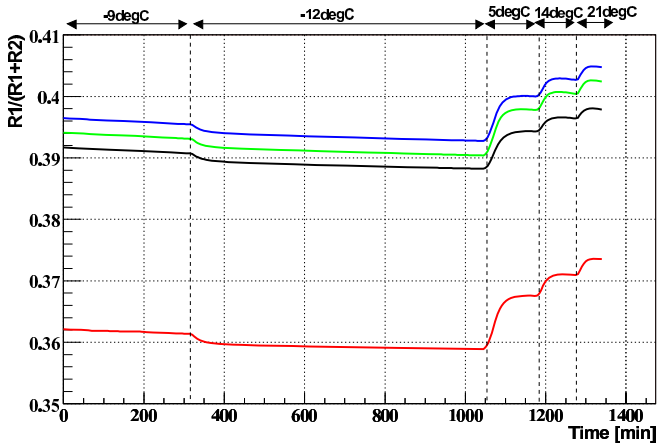

Figure 5.8: Ratio of the Xeriton sensor resistances measured at 0% RH humidity and for 5 differenct temperatures. The temperatures are noted on the top of the plot.

Using the corrected resistance values, the response parameters a and b from Equation (5.1) were determined. A calibratation sequence with four calibration points was performed using the climate chamber. The first calibration point was recorded at $\sim$ 0% RH and to ensure that the sensors were fully stabilised the chamber was flushed with dry nitrogen a minimum of 48h before the calibration sequence was started. The second calibration point was recorded at medium humidity while the third point was taken with the chamber saturated with water vapor. The last calibration point was again recorded at medium humidity. The entire calibration sequence was done at 20°C and Figure 5.9 shows a calibration sequence for 5 sensors and one reference measurement. The reference measurement was taken as the mean value of two Honeywell humidity sensors of model HIH-3605-B, which has a significantly faster response time than the Xeritron sensors under evaluation.

The performance of a calibrated sensor can be seen in Figure 5.10. The new calibration gives a very good agreement with the reference sensor but the Xeritron sensor has a slow response. This is a known feature of the sensors and a detailed study of the response time is given in [15].

A total of 40 sensors were calibrated in Uppsala and shipped to the macro assembly sites (Oxford for the SCT barrels, NikHef and Liverpool for the

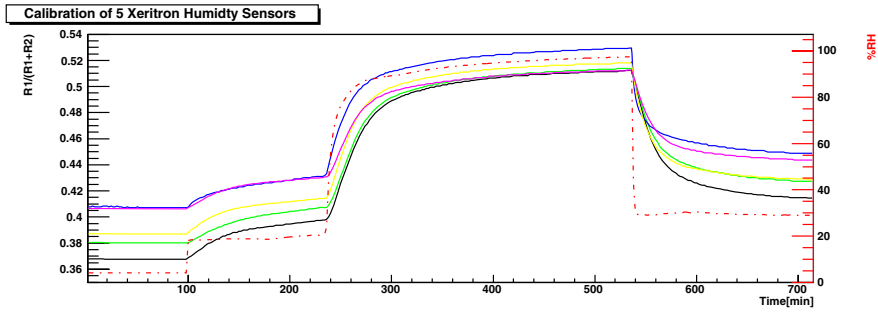

Figure 5.9: Calibaration run for 5 Xeritron humidity sensors taken at 20 °C. The red dashed line represents the references measurement.

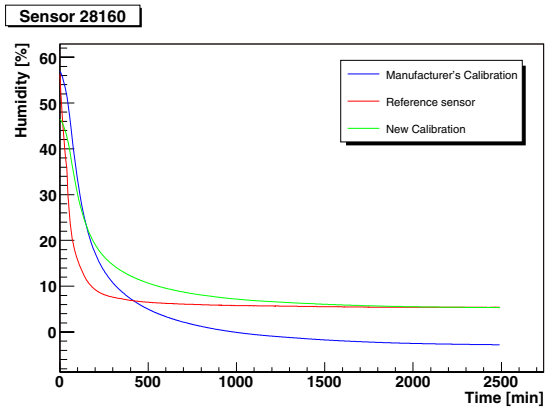

Figure 5.10: Comparison of the manufacturer's calibration and the calibration described in this section and in [15]. With the new calibration the sensor reading converges to the correct value given by the reference sensor after $\sim$ 1500 minutes.

SCT forward disks) for being mounted on the support structure. After installation their performance has been tested at CERN, both during barrel and disk reception and during the combined SCT and TRT barrel run (See Paper V).

5.4 The SCT Detector Control Systems

The SCT Detector Control System (DCS) is responsible for stable and safe operation of the detector and consists of several subsystems to supply the detector with the necessary power and cooling. Each subsystem consists of both hardware and software and is designed to operate independently of the other subsystems as well as together, as they will in the final integrated system.

Figure 5.11 gives a schematic overview of the different systems that are needed to operate the SCT detector in a controlled way. The power system is the largest DCS subsystem and has two components: 1) The Power Supply System (PS) which delivers high and low voltage together with various

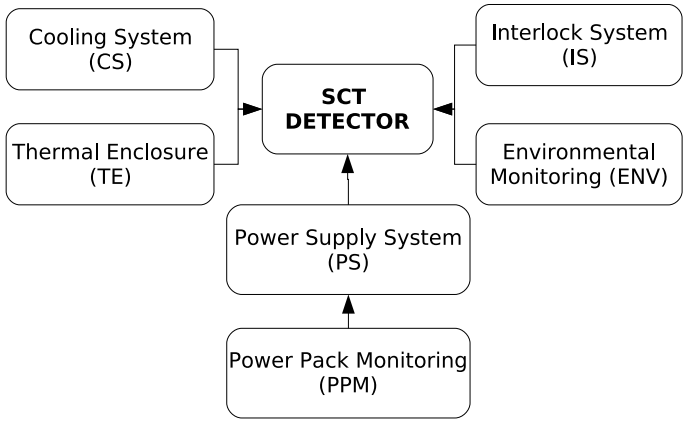

Figure 5.11: Overview of the detector control systems needed for running the SCT detector.

control commands to each individual detector module, and 2) the Power Pack Monitoring (PPM) which monitors the 48V and 12V supplies to the PS racks. The Cooling System (CS) controls the evaporative fluorcarbon cooling which cools both the SCT and Pixel detectors, while all temperatures are monitored by the Environmental Monitoring project (ENV) which reads out the thousands of sensors that the SCT detector is equipped with. The Thermal Enclosure (TE) ensures that the SCT and Pixel detectors are kept cold and dry (nitrogen) inside the warm TRT environment. Finally there is an Interlock System (IS) which connects (through the IBOX [50] and IMatrix) the thermistors situated on each cooling pipe outlet to a System Interlock Card (SIC) in the PS rack. In the event of a fatal high temperature reading on a cooling pipe outlet the IS system will interlock all LV&HV cards powering modules on the the pipe in question.

All control systems as they appear today are the results of several years of research and development [30]. In particular the macro-assembly and integration at CERN was most valuable for large scale tests of the individual systems as well as the inter-system communication. Paper V presents the DCS setup and results from SCT barrel reception and Combined Testing (described in Section 6).

5.4.1 Power Supply Hardware

The Power Supply hardware is best described starting with the PS crate which is the smallest unit of operation in the PS project. One crate provides power to 48 detector modules (PS channels) and consists of:

- **6 High Voltage (HV) [28] cards** which supply bias to 8 detector modules each. The HV card can supply bias in the range 0V to 500V with a precision

of 1V and read back the applied voltage with a relative precision of 1%. The ramping speed kan be set in the range 3 to 50 V/s.

- **12 Low Voltage (LV) [35] cards** which supply the ASICs (analogue and digital circuitry) and opto packages with power. Each card can supply 4 detector modules with power and the analogue and digital part for each channel is fully separated and floating. The LV card also reads out the NTC thermistors placed on each side of the hybrid [52].
- **1 Crate Controller (CC) [27] card** which controls all 18 LV and HV cards of the crate and thus serves as the interface between the cards and the DCS software. The CC is made from a general purpose ELMB[2] mounted on a custom made motherboard. The CC also features a EEPROM memory for storing predefined channel settings for different run states.
- **1 System Interlock Card (SIC) [26]** which receives an input from the IMatrix and in the event of a high temperature reading (or any other interlock event) the card switches of the channel power in less then 1s.

Each crate is connected to a DCS computer by means of a CAN bus network, according to the Communication Area Network (CAN) [18] open communication protocol. Requirements on the read out frequency of the system and trafic limitations on the bus limits the number of crates to be connected to one DCS computer to 11. Figure 5.12 shows the typical layout for one such system with 4 crates in each rack. Between each crate in the rack a fan is inserted and at the bottom (or top) four power packs are located as well as the circuit breaker box.

The complete PS system for the SCT comprises a total 88 crates which has to be divided on 8 computers known as Local Control Stations (LCS) for operation. 4 LCS stations are located in each underground cavern (US15 and USA15) divided in 2 computers for endcap crates and 2 computers for barrel crates. The 8 LCS computers are connected via Ethernet to one top level computer known as the Subdetector Control Station (SCS). The SCS interfaces all the SCT DCS subsystems to one common user interface for the end user, and it is also the connection point towards the DAQ system.

5.4.2 Power Supply Software

ATLAS DCS is constructed to enable a homogenous integration of all subdetectors into one final common DCS structure which ultimately will be integrated into the LHC DCS. To achieve this a common Supervisory Control and Data-Acquisition (SCADA) software has been chosen, the PVSS II by ETM Austria [46]. An ATLAS developed CANopen OPC server [53] is integrated into PVSS and enables PVSS to communicate with the hardware on the CAN bus, thus a so-called PVSS project can both monitor and control the hardware.

[2]The Embedded Local Monitoring Board (ELMB) [48] is a general purpose low cost standardised plug in board based on the main AVR micro-prosessor ATmega128L.

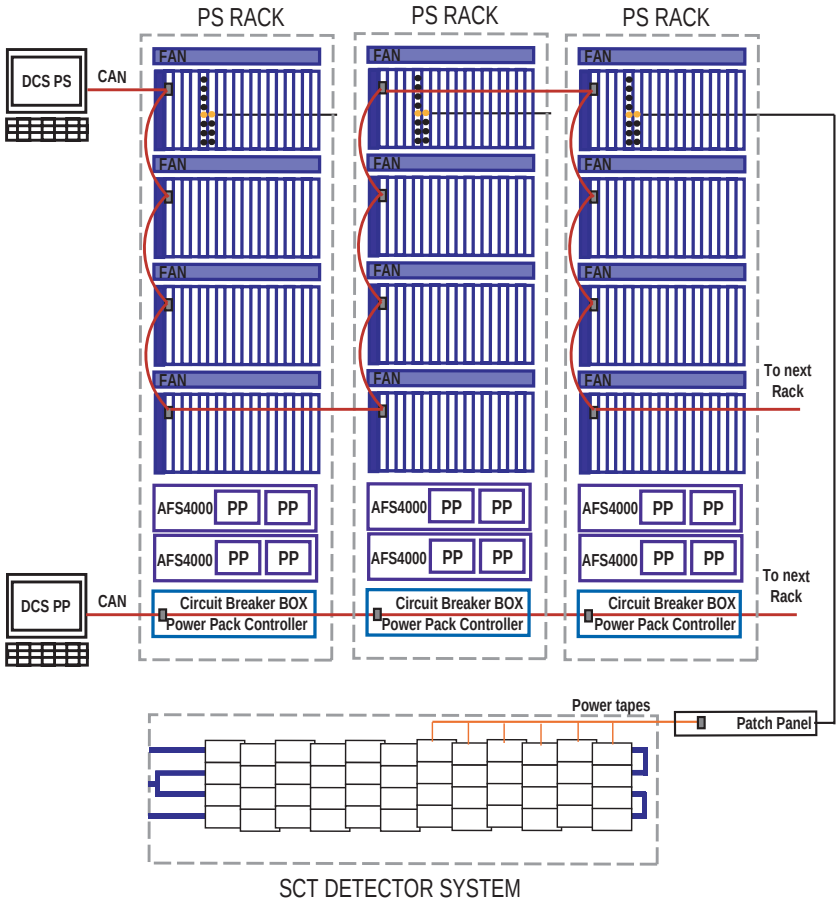

Figure 5.12: Schematic overview of the Power Supply hardware. Each rack contains 4 crates and 4 power packs. 11 Crates are read out to one DCS computer (LCS). Power is delivered to the individual sensor module via cables that ultimately connect to the Low Mass Tapes (LMT) that connects to the modules. Figure taken from [30].

The CERN Joint Controls Project (JCOP) [36] was initiated to develop common software tools and in particular solutions tailored to the hardware, such as the ELMB, which is common to the many LHC experiments.

Figure 5.13 shows the ATLAS DCS hierarchy. The SCT Sub Detector Control Station controls the SCT Power Supply and the Environmental monitoring, while Cooling and Thermal Enclosure, which are common for all 3 subdetectors of the Inner Detector, are located under an Inner Detector control station. All systems are linked to each other as distributed PVSS projects to enable DCS-DCS communication. As mentioned above the PS system comprises a total 8 computers each one of them running a custom made PVSS project known as the Monitoring Power Supply (MoPS) project.

The MoPS project is designed for complete monitoring and control of a large number of parameters. One LCS (one PVSS project installation) can

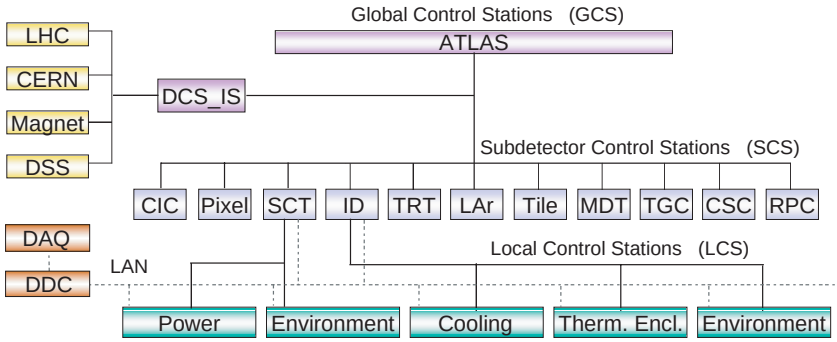

Figure 5.13: The ATLAS DCS hierarchy.

handle up to 11 crates which each supply 48 SCT detector modules with power. The number of parameters per module is about 30 (LV & HV), making a total of 16500 parameters which are to be updated every 15s for one LCS system. The parameter transfer from the OPC server to the MoPS project is done by means of adresses. Each PVSS datapoint is assigned with a unique adress that is used by the OPC server.

The MoPS project allows the user to command single channels, groups of channels or single or all crates. This can be done using various interfaces as explained in Paper IV. Commands can be sent to change the operational state from OFF to STANDBY and to ON which are predefined operational states for which the voltage set points (a configuration) are stored in the CC EEPROM. The EEPROM stores 3 sets of configurations for each channel which can be updated by a configuration tool featured by the MoPS project. In addition to state transitions to a predefined operational state, the MoPS project also enables complete manual control for individual channels, a functionality that is important for finding optimal module performance.

Slow commands to the SCT detector module and software (firmware) trip limits implemented in the PS cards and CC are also handled by the MoPS Project:

- **Hard reset** - A signal is sent to the module which will hard reset all its electronics.
- **Select line** - Instructs the module to receive its clock and command from the neighboring module.
- **Trip Limits** - In addition to hardware trip limits implemented in each card there are programmable firmware trip values that can be set for both card and CC for sensitive values. See Paper V for details.
- **Commanded readout** - Upon request a crate can be read out by the user to check for the immidiate effect of e.g. an issued command.

While the firmware and hardware trip limits ensure the module safety, they do not warn the user about the presence of a problem such that the problem can be resolved before the HV or/and LV are switched off by either the PS card

itself or the CC. To solve this issue the MoPS project has PVSS alerts implemented for each monitored parameter. The alert has 5 ranges being *low/high alarm, low/high warning* and *ok* often referred to as the status of the parameter. Stable operation should be represented by status = ok, but in the event of a low/high readout which crosses the boundary (threshold) between two ranges the status will change to reflect the new readout. The MoPS user will be visually notified about the situation by colours which reflects the status. Each channel has a summary alert associated with it which is a logical "or" of all parameter alerts associated with it. This is used to derive the status of the module.

The size and complexity of the MoPS project requires a robust and maintainence friendly implementation. This is ensured by the usage of scripts and libraries throughout the project. Scripts contain functions that are realtime connected to datapoints. If the connected datapoint changes the specified callback function will be executed and perform its tasks. Using this functionality, all commands in the MoPS project are implemented as scripts which are connected to special command datapoints. Graphical applets which involve state transitions, configurations, readouts, etc will, instead of excuting any code on their own, write the command input parameters given by the user to the command datapoint and leave the execution to a connected script. Thus, the graphical user interfaces contain a minimum of code with the core code of the project being available through scripts and libraries.

A detailed introduction to the MoPS project is given in Paper IV which summarizes the present status of the software. Considerable experience gained during macro-assembly and later during barrel/endcap reception and intergration at CERN (Paper V) has already been implemented in the software but it is an inevitable fact that the software will change and improve once the complete SCT detector is ready for operation within ATLAS.

5.4.3 The Finite State Machine

Ultimately the DCS hierarchy as presented in Figure 5.13 will be implemented using a Finite State Machine (FSM) [29] written in SMI++ [51]. In the FSM a strict hierarchy (tree) is built from two kind of nodes which are assigned with a state and status[3]. The *Device Unit* (DU) represents physical equipment (e.g. a SCT detector module) and is able to monitor its state and status and to control it. The *Control Unit* (CU) correspond to a Finite State Machine and can model and control the tree below itself. A third variety the *Logical Unit* (LU) also exists, but this is just a scaled down version of the Control Unit which can not have CUs as a child, i.e. it can only be the mother of DUs.

In a FSM hierarchy, commands flow downwards while state and status information is propagated upwards as shown on Figure 5.14. Each DU derives

[3]A node's state corresponds to its operational state e.g. "running", while the node's status represents how well the node is doing, e.g "overheating".

its state and status information directly from PVSS datapoints to which it is connected while the CUs and LUs calculate their state and status from their children. A FSM tree can be partioned, meaning that a CU (or LU with some limitations) can be disconnected from the tree. Several partitioning modes exist and below a short description of each mode is given:

- **INCLUDED** - Normal mode of operation. The CU receive commands from its parent and its state/status is taken into account by the parent.
- **EXCLUDED** - The CU does not receive any commands, nor is its state/status evaluated by its parent.
- **STAND ALONE** - The component is removed from the tree to work in a stand alone mode. It does not belong to the hierarchy any more and has a new owner.
- **COMMANDS DISABLED** - No commands are received by the node, but its state is taken into account by the hierarchy.
- **MANUAL** - Expert operation mode where the expert user has full control.
- **IGNORED** - The node recieves commands from the parent node but its state is not taken into account.

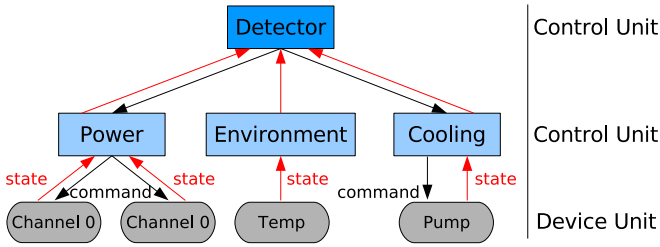

Figure 5.14: A FSM structure. Using partioning (as explained in the text) the Environment, Power or Cooling CUs can be disconnected from the tree and operated in a stand alone mode.

FSM for the SCT Power Supply

Ultimately the SCT power supply system will only have one state and status. The FSM tope node thus have to reflect the state and status of 4088 SCT detector modules which all have individual LV and HV supplies. Consequently the system has to be designed with great care in order to acheive a control structure which offers the best possible information about the overall system state but at the same time ensures that information about critical events are propogated upwards. One such example would be a cooling pipe failure, causing 24 modules to be powered off to prevent them from overheating. From the SCT overall point of view the loss of 24 out of 4088 modules is not critical

for datataking, which most likely should continue, but at the same time the incident is critical since the may be an early symptom of a larger problem.

Motivated by the example above and the structure of the SCT detector and DCS software it is natural for the SCT power supply system to construct a control hierarchy which has modules grouped into cooling loops as the two lowest levels. The module, or PS channel, is a device unit and its state and status should be the sum of both the HV and LV supplies that it depend on. Above the module the cooling loop is implemented as a logical unit, deriving its state and status from its module children and being able to control them by sending commands to a special crate controller device unit.

As explained in Paper IV, the HV and LV states are calculated by the crate controller and updated in the PVSS project with every readout of the crate. Figure 5.15 shows how the LV and HV states are combined to form PS channel (module) states and how it is possible to move from one PS channel state to the other. Solid lines/arrows represent user initiated transitions while the dashed lines/arrows are automatic state transitions with the exception of transitions to the MANUAL state. The MANUAL state can be entered and left from any other state except from the error states. There are several error states reflecting that errors can arise in either the HV or LV supply or both at the same time. The UNKNOWN error state is special, corresponding to monitored parameters from the HV, LV or both do not match neither the CC database nor the RAM. In other words the voltages have drifted away from there requested values without any user interference. Finally there is an interlock state which is reported by the crate controller when the PS cards are interlocked by the SIC card in the crate.

The main design philosophy behind the definition of the cooling loop states is that during normal operation (i.e. no children in error states) the highest state of the module children should be flagged. This is implemented using partial (_Part) states for the cooling loop unit as shown on Figure 5.16. An unsuccesful ramping from STANDBY to ON would thus lead to the ON_PART state. This tells the user that one or more modules did not move to the requested ON state (possibly due to a missed command) and to resolve the situation the GO_ON command needs to be resent. The partial states also protects the system from unwanted commands sent to modules, thus from a partial state it is only possible to move to the “complete” state or to the state directly below it. This forces the user to resolve the situation with missed commands at every stage during switch on and prevents modules from receiving a GO_ON command before they have reached the STANDBY state. It should be emphesized that the probability for a module to miss a command is small.

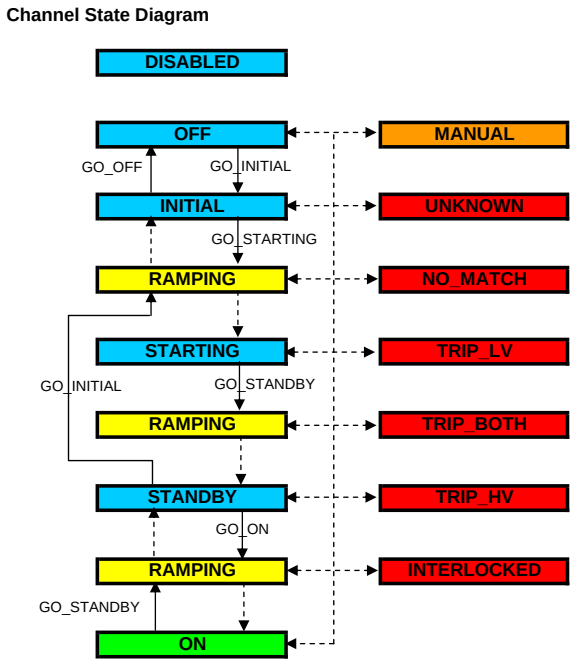

(a) PS channel (module) state diagram. Solid lines are commanded state transitions while dashed lines, except to MANUAL, are automatic transitions.

State Conditions

State	Condition		Comment
ON	LV ON	HV ON	State used for physics
STANDBY	LV ON	HV STANDBY	State used during LHC filling and/or unstable beam
STARTING	LV STANDBY	HV STANDBY	State used when powering up the detector (or for tests)
INITIAL	LV OFF	HV OFF	PS channel powered but set to deliver zero volts
OFF	LV MASKED OFF	HV MASKED OFF	PS channel not powered
DISABLED	LV DISABLED	HV DISABLED	Channel must re re-enabled in Configuration DB
RAMPING	LV, HV or both in RAMPING		Transitional state: will always resolve to another state
MANUAL	LV, HV or both in MANUAL		Set to temporary commanded values by expert user
UNKNOWN	LV, HV or both report unknown		CC-HW or PC-CC communication failure
NO_MATCH	LV, HV or both in NO_MATCH		Monitored values do not match commanded values
TRIP_BOTH	LV & HV tripped by hardware or software		
TRIP_LV	LV tripped by hardware or software (inc latch)		
TRIP_HV	HV tripped by hardware or software		
INTERLOCKED	Channel Interlocked by SIC card (hardware)		

(b) PS channel (module) state conditions as function of HV and LV state.

Figure 5.15: The FSM states and transitions for the PS channel (module).

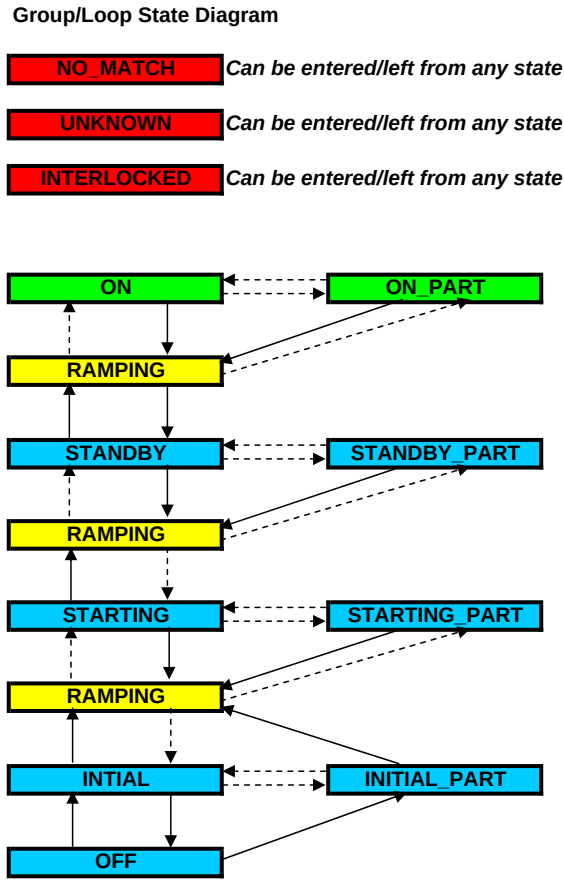

(a) PS channel (module) state diagram. Solid lines are commanded state transitions while dashed lines are automatic transitions.

State	Condition
ON	All children of type Module in state ON
ON_PART	ON is highest state of children of type Module
STANDBY	All children of type Module in state STANDBY
STANDBY_PART	STANDBY is highest state of children of type Module
STARTING	All children of type Module in state STARTING
STARTING_PART	STARTING is highest state of children of type Module
INITIAL	All children of type Module in state INITIAL
INITIAL_PART	INITIAL is highest state of children of type Module
OFF	All children of type Module in state OFF
RAMPING	Any child of type Module in state RAMPING
NO_MATCH	Any child of type Module in state NO_MATCH
UNKNOWN	Any child of type Module in state UNKNOWN
INTERLOCKED	All children of type Module in state INTERLOCKED

(b) Cooling loop state conditions as function its module childrens.

Figure 5.16: The FSM states and transitions for the cooling loop.

In order to move move from one state to another the FSM system needs a set of state transition rules which allows it to compute what will be the new state (if any) when the system changes. On the FSM jargon this is called a “when list” and one such list is associated with each state. For units (device, control or logical) with several states, like the cooling loop, and where each state may transform into a relatively large subset of the defined states the design of the “when lists” is a delicate business in order to avoid the system entering an infinite loop. It is also important from the point of view that the “when list” defines the ranking of the states, i.e. some of the states are overlapping thus they have to be prioritized. Hence, for the power supply FSM a technique is used where the RAMPING state is used as a transient state which has the full set of rules and any system change would pass via the ramping state which then uses its “when list” to find the new state. Another great benefit of this approach is that future updates of the system only involves changing code in one place.

In the above paragraphs we have only discussed how states are defined and propated from LV/HV channel to PS channel (module) and finally to the cooling loop. However, in the final implementation each node in the FSM tree will have both a state and status as explained earlier. This is done by implementing two nested FSM trees where one tree handles states and commands as discussed above, while the second tree only propagates status information and has no command implementation. Thus there exist status counterparts to the units discussed above which reflect the status of the PS channel (module) and cooling loop. The PS channel status is taken from the PVSS summary alert as explained in Section 5.4.2 while the status for the cooling loop is derived as the logical “or” of all its children.

Each DCS computer has limited FSM capacity meaning that it can only operate a limited number of FSM units at the same time in a reliable way. Hence, the SCT power supply FSM is constructed in such a way that all the PS channel device units and cooling loops are run by the LCS systems. These systems then take the largest CPU load of running the system, leaving the SCS with a minimal load. At the SCS level the final SCT FSM is built. Cooling loops from the power supply project are referenced from the LCS systems and grouped together into barrel and end caps. Sensors from the Environmental monitoring project are added and similarly information from the cooling project itself. At the time of writing this integration is taking place at CERN and it is foreseen to hand over the control of the SCT detector to ATLAS central DCS early summer 2007.

6. SCT Detector Alignment using Cosmic Rays

In February 2006 the SCT and TRT barrels were joined, thus forming the first combined detector element of the Inner Detector. Following this a series of cosmic runs were performed during spring and summer 2006 where a total of 450 000 cosmic events were recorded and analysed. The cosmic runs (named "SR1 combined testing" after the name of the clean room facility housing the detector structure) were excellent tests of both online and offline software as well as of the DCS systems as discussed in the previous chapter.

For this thesis I have been working on the local χ^2 alignment of the SCT barrel detector, a work performed in collaboration with Ola Øye and presented in Section 6.4. We also investigated the possibilities for ideal track selection for alignment based on ideas presented in [34]. The work is summarized in Section 6.3. Before these two sections a general introduction to the hardware and software setup is given in Section 6.1 while Section 6.2 gives an introduction to the track reconstruction algorithm and its performance.

From now on we shall refer to the SCT barrels as layers which is the terminology used by offline software. Layers are counted from zero rather than three and thus we identify barrel 3, 4, 5 and 6 with layer 0, 1, 2 and 3 respectively.

6.1 Detector Setup and Simulation

Following the insertion of the SCT barrel into the TRT barrel the combined SCT&TRT barrel was positioned inside an enclosure in the SR1 clean room with a set of scintillators positioned above and below the combined barrel. The scintillators were positioned close to the instrumented parts of the barrel, which due to limited accessibility of hardware and time constraints, were limited to two diametrically opposite sectors shown on Figure 6.1. For the SCT a total of 467 modules were cabled and read out, corresponding to almost 1/4 of the complete barrel.

3 scintillators were used for triggering where the top and middle ones were position right above and underneath the instrumented sectors shown on Figure 6.1. The third scintillator was placed under the concrete floor of the clean room in order to achieve a $\sim 200 - 300$ MeV momentum cutoff. Each scintillator was read out by PhotoMultiplier Tubes (PMT) and a trigger was gener-

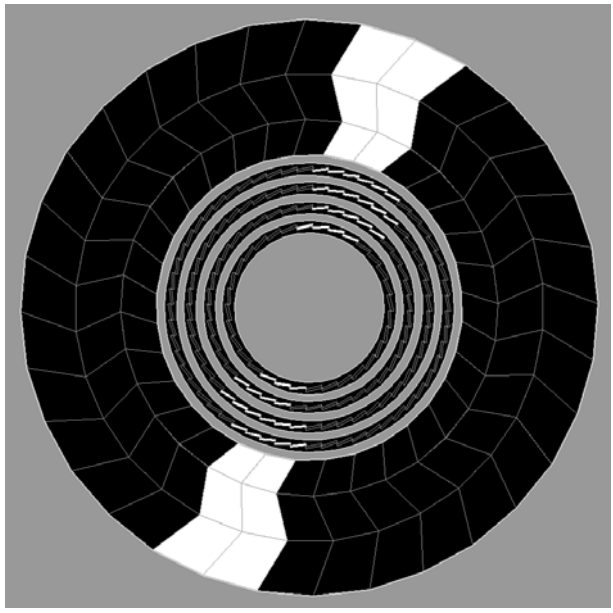

Figure 6.1: The readout configuration of SCT and TRT. The active detector elements are indicated in white.

ated upon a coincidence of the mean signal from the top scintillator and the mean signal of the middle scintillator. The detector was clocked and readout at 40MHz.

Well before the actual cosmics runs were taken, a simulation of the detector setup as described above was implemented in Athena, the ATLAS offline framework [10]. This served both as an important test bed for the reconstruction software to be developed, but it also provides important information about how well the model of the detector, as implemented in the simulation software, mimics the real detector.

The cosmics Monte-Carlo generator *CosmicsGenerator* was used as the input for the detector simulation. It generates single muons with a position and momentum-vector from a user-defined horizontal spatial window. The generated muons have energy and momentum distributions close to those observed by dedicated cosmic experiments. In the setup a user-defined window right above the upper scintillator was used, but since this would yield many muons that would not hit the middle scintillator a modification was done to the generator such that only muons that would hit both top and middle scintillator were generated.

More details about the detector setup and implementation of this in software can be found in [45].

6.2 Track Reconstruction and Performance

The major differences between track reconstruction during LHC data taking and the SR1 cosmics runs is the absence of the magnetic field, hence the reconstructed tracks are straight lines, and the fact that cosmics rays do not originate from the centre of the detector. The Combined Test Beam (CTB) tracking [22] algorithm was developed for such scenarious and thus chosen as the default tracker for the cosmics runs. The CTB-tracking can operate in a combined or stand alone mode. In combined mode a track is fitted through both the SCT and TRT detectors, while in stand alone mode only one of the detectors is chosen. In the following text we shall assume stand alone SCT tracking only.

CTB-tracking constitutes two parts. First there is pattern recognition which, seeded by spacepoints[1], tries to find at least 3 SCT spacepoints forming a line. If a pattern is found the fitted straight line is propagated to modules with no spacepoint in them. Any single side hit, called a cluster, close to the track is associated with the track.

Following pattern recognition the hits associated with the track are fitted by the GlobalChi2 fitter[2]. The fitter minizes the expression

$$\chi^2 = \sum_{i=1}^{N} \frac{r_i^2}{\sigma_i^2},$$

where N is the number of hits associated with the track, r_i is the track residuals and σ_i is the intrinsic measurement error of the hit. A track residual is defined as the shortest distance between the fitted track and a hit associated with it. For the SCT hits (clusters), which do not have any longitudinal information assigned to them, the residuals were defined to be the closest distance between the fitted track and the associated hit in the module frame of the hit.

Figure 6.2 shows a real cosmics event in the combined SCT and TRT barrel. Without Coulomb scattering one would expect that the SCT residual distribution would yield a sigma close to the intrinsic $r\phi$ resolutions of the detector (23 μm) when fitted with a Gaussian. However, low momentum muons are subject to large Coulomb scattering contributions which significantly degrade the results. Understanding the Coulomb scattering's impact on the residuals distribution is important since the dominant part of the cosmic energy spectrum is low energy [34] and the symptoms are the same as those of a misaligned detector.

The residuals distribution from simulation separated into energy bins is shown in Figure 6.3. It is clear that below 10 GeV the contribution from Coulomb scattering dominates over the intrinsic detector resolution. Ideally,

[1] A spacepoint is formed by hits on each side of the detector module that are intersecting each other in the $r\phi$-plane.

[2] For optimal performance the fitter works only with hits (clusters) and not spacepoints which are only used for the pattern recognition.

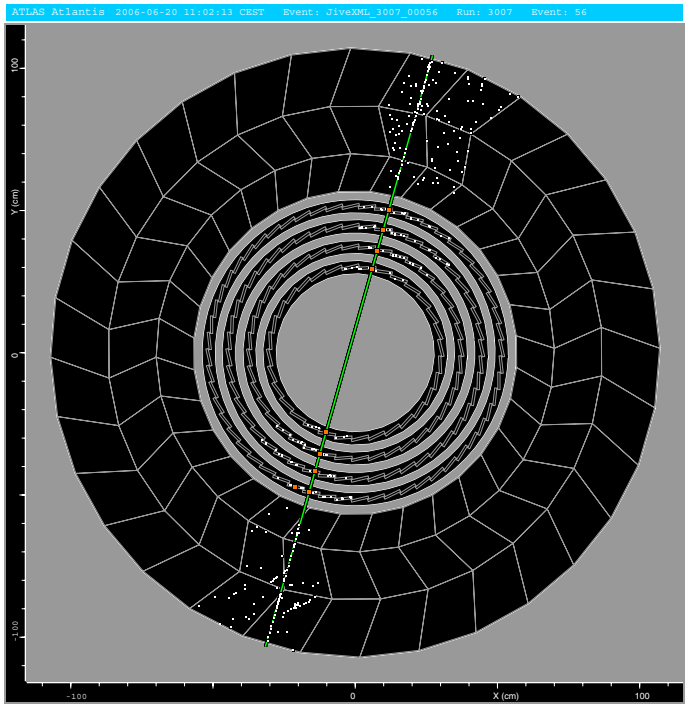

Figure 6.2: The Atlantis event display showing a reconstructed cosmic track in the combined SCT and TRT barrel. Shown with orange square markers are the SCT space-points.

only tracks with momentum above this threshold would be used for alignment purposes. However, the absence of a magnetic field calls for different techniques for their identification.

6.3 Alignment Track Selection

Particles passing through matter are subject to multiple scattering along their path. Muons passing through the SCT detector thus risk being deflected from their path every time they cross a barrel layer. The distribution of scattering angles encountered by a particle when traveling through matter follows a gaussian law, centered at zero, whose width obeys the Moliere formula:

$$\sigma_s = \frac{13.6\text{MeV}}{p\beta}\sqrt{\frac{L}{X_0}}\left(1+0.038\ln\left(\frac{L}{X_0}\right)\right) \tag{6.1}$$

Moliere's formula depends on the mass and speed of the transversing particle (β and p) and the width of the transversed material in radiation length $\frac{L}{X_0}$. The amount of material seen by an incoming muon in the SR1 cosmics setup varies from layer to layer due to the different impact angle the muon has with

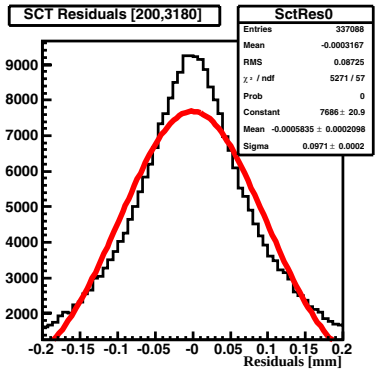

(a) 200 MeV - 3.18 GeV.

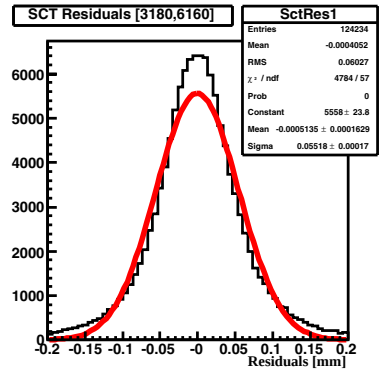

(b) 3.18 GeV - 6.16 GeV

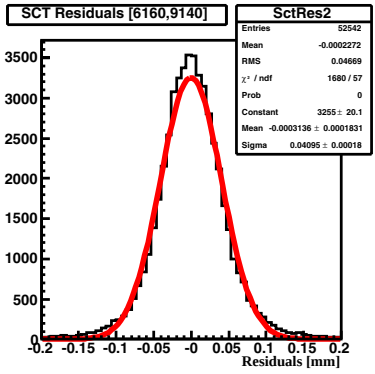

(c) 6.16 GeV - 9.14 GeV

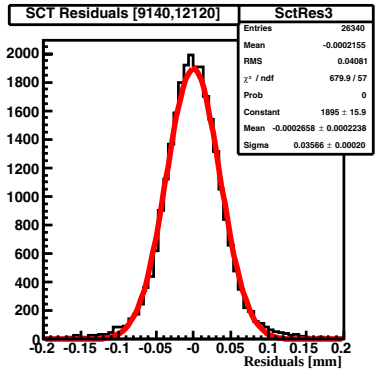

(d) 9.14 GeV - 12.12 GeV

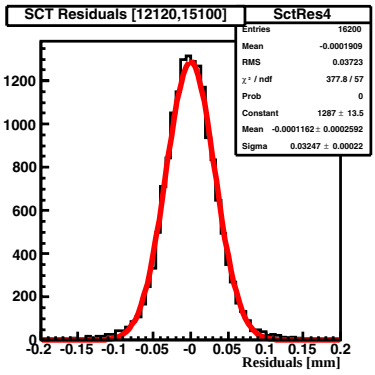

(e) 12.12 GeV - 15.10 GeV

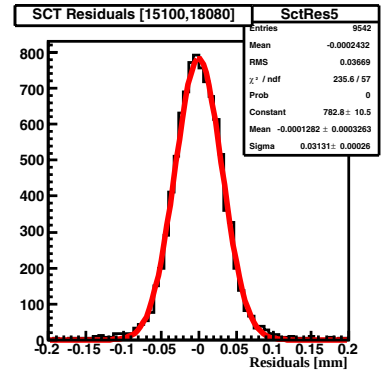

(f) 15.10 GeV - 18.08 GeV

Figure 6.3: Gaussian fits to SCT residuals from 200 MeV to 18.08 GeV. Figures adapted from [45].

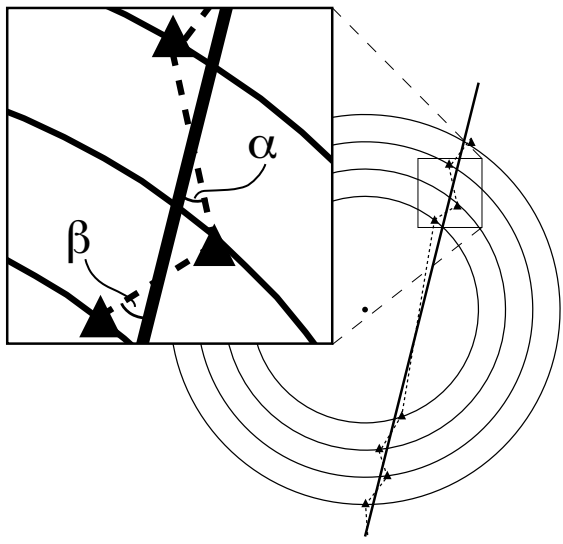

Figure 6.4: Fitted track along with zigzagging real path. The zigzagging effect has been magnified for the purpose of illustration. The triangles represent the hits read out by the detector. We define the angle α to be positive, while β is negative. Figure adapted from [34].

each barrel layer. This difference in turn depends on the distance between the center of the detector and the traveling particle as seen on Figure 6.4.

6.3.1 Kink Analysis

The CTB tracking algorithm as discussed earlier fits a straight line to the hits of a track minimizing the residuals of the hit weighted by the intrinsic measurement error. This approach does not take multiple scattering effects into account and it is thus to be expected that for low momentum tracks the residual distribution is wider.

By looking at the individual hits associated with a track and join hits from module sides that have their strips aligned with the z-axis (beam pipe) by straight lines, we can study the angle between the track direction and the line segment joining two such consecutive hits. We call this angle a kink in the $r\phi$-plane and its sign is determined by the convention shown in Figure 6.4.

Figure 6.5 shows the kink distribution from layer to layer for a perfectly aligned detector (nominal alignment). The distributions were obtained with simulation and the results agree well with the expectations that the width of

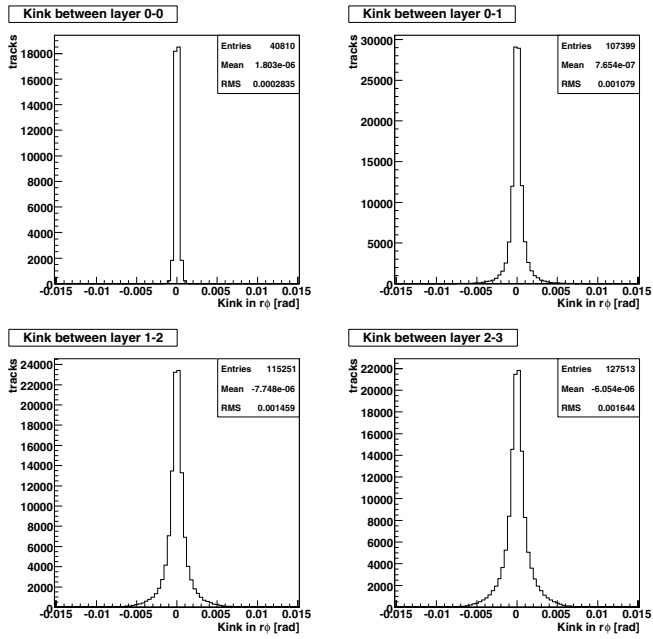

Figure 6.5: Distributions of kinks from layer to layer with perfect (nominal) alignment of the detector. Crossing of the central layer is (top left) is almost insensitive to kinks due to the absence of the pixel detector.

each distribution varies between layers due to the difference in the amount of material seen by the muon. Due to the absence of the pixel detector, the centre of the SCT detector is hollow and thus limited multiple scattering is expected when the muon moves from one side of layer 0 to the other. This is confirmed by Figure 6.5.

While the kink distributions obtained for a perfectly aligned detector are symmetrically centered around zero, one would expect that the misalignment of the detector would yield asymmetric distributions. A global shift of layers with respect to each other would bias the distributions towards a positive or negative kink, underlying the individual displacement of the modules. The impact of misalignment can be seen on Figure 6.7 where the SCT detector has been misaligned with the misalignment set *sctdisp2* as given in Table 6.1.

For each cosmics track reconstructed by the detector, it is possible to measure up to 7 kink angles following our definition (2 angles being the minimum due to the requirement on having at least 3 spacepoints for the tracking). Given n measured angles for a selected track we can compute the mean and variance of the kinks defined as

$$\bar{\alpha} = \frac{\sum_{i=1}^{n} \alpha_i}{n} \tag{6.2}$$

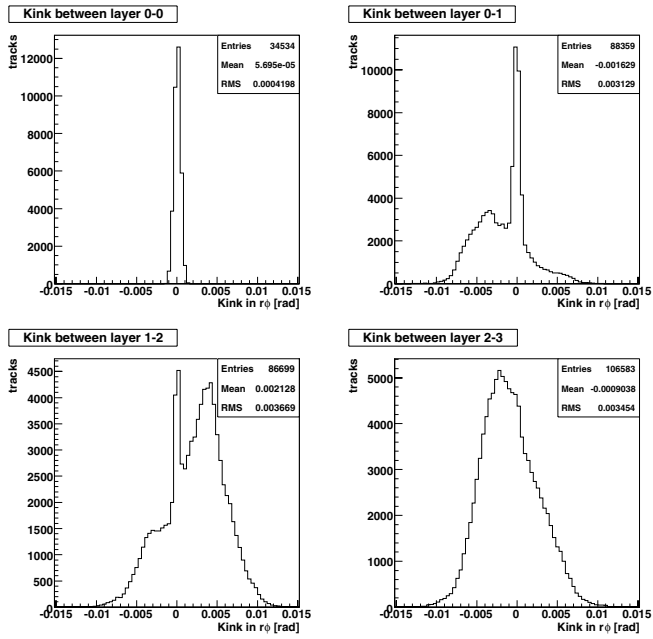

Figure 6.6: Distributions of kinks from layer to layer with a detector misaligned with the misalignment set *sctdisp2* (Table 6.1). The central layer (layer 0, top left plot) is only sensitive to a rotation of the layer around the beam axis together with individual module displacement so limited impact is seen.

$$\sigma_\alpha^2 \quad = \quad \frac{\sum_{i=1}^{n}(\alpha_i - \bar{\alpha})^2}{n-1}. \tag{6.3}$$

For a perfectly aligned detector the variance σ_α mainly contains the intrinsic measurement error of the detector and effects caused by multiple scattering. The latter is momentum dependent, and thus our hypothesis is that the computed variance (at least for the aligned detector) should show a $1/p$ behavior as given by Moliere's formula (Eqn. (6.1)). If verified this could give us an important handle on the momentum of the muon, enabling selection of reasonably high momentum tracks for alignment purposes.

Figure 6.7 shows the angle variance as function of the muon momentum for both nominal alignment and misalignment. While the nominal alignment shows good agreement with our hypothesis above (shown by a fit of Moliere's formula to the obtained distribution) it is clear that the effects from the misalignment completely dominate over the momentum behavior. We are thus forced to conclude that no selection of high momentum muons is possible for the cosmics setup, unless refined techniques, like e.g. studying fixed modules combinations in which the contribution from misalignment is constant, are considered. This however requires enormous amounts of statistics and is not feasible given the limited time of data taking.

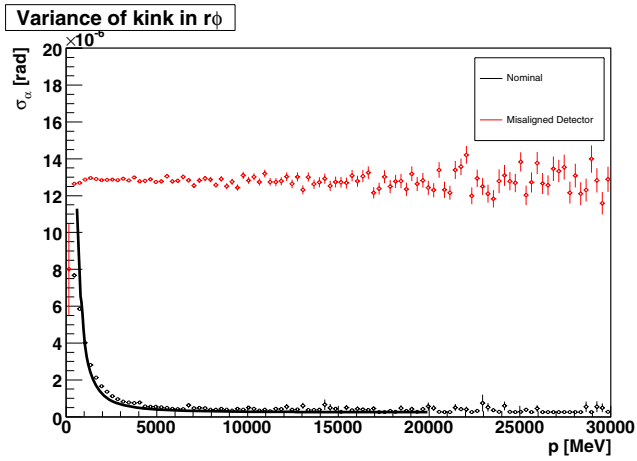

Figure 6.7: Kink variance distribution from simulation using both nominal and misaligned detector geometries. The nominal distribution is fitted with Moliere's formula.

6.4 SCT Alignment

A well aligned detector is a necessity in order to fulfill the ATLAS requirements on track and vertex reconstruction resolution. For the SCT the mounting precision of the detector modules to their support structures is $\sim 100\mu$m, a precision which completely dominates over the intrinsic resolution of 23μm.

The local χ^2 alignment approach [32] aligns each silicon detector module individually by minimizing a χ^2 function based on track residuals. Unlike the global approach [16] the local approach does not take correlations between modules into account. Modules are adjusted independently of each other and the impact of adjusting a module's space coordinates on the residuals for the other modules associated with the track is not evaluated. Inter-module correlations are rather brought into play by having the alignment algorithm run iteratively until convergence has been obtained.

In the following sections, the local local χ^2 approach is presented together with results obtained by applying the alignment algorithm to either real or simulated cosmics data. It should be emphasized that these are initial studies. For a full alignment, the size of the data samples needs to be substantially increased, and the procedures and cuts need further refinement.

6.4.1 The Local χ^2 Approach

The χ^2 of the track residuals can be written as

$$\chi^2(\vec{a},\vec{\pi}_1,\ldots,\vec{\pi}_m) = \sum_{i\in tracks}^{m} \vec{r}_i{}^T(\vec{a},\vec{\pi}_i)\cdot V_i^{-1}\cdot\vec{r}_i(\vec{a},\vec{\pi}_i) \tag{6.4}$$

where $\vec{r}_i$ is a vector of residuals belonging to track i, $\vec{a}$ is a vector of alignment parameters, and $\vec{\pi}_i$ is the vector of track parameters for track i. Defined in the local frame of the SCT detector module, the module has 6 degrees of freedom. (x, y, z) are the translational parameters where x is the parameter transverse to the strip direction, y is along the strip direction and z is defined by having a right-hand coordinate system. The angular parameters (α, β, γ) are rotations around the respective axes.

The alignment algorithm aims to minimize (6.4) such that

$$\frac{d\chi^2(\vec{a})}{d\vec{a}} = \vec{0}. \tag{6.5}$$

As a first step we write (6.4) as a Taylor expansion to first order. By doing this (6.5) can be expressed as a set of n coupled linear equations, where n is the number of degrees of freedom for the system. For the cosmics case this is $n = 6 \times 467 = 2802$.

When a module's position is updated through an alignment procedure the new position of the module will change the residuals for other modules on the track's path. The basic idea of the local χ^2 approach is to ignore these correlations between modules in order to solve the χ^2 minimization. By doing this, the coupled set of linear equations is reduced to a simple sum, where the alignment parameters satisfying (6.5) are given by [32]

$$\begin{aligned} \Delta\vec{a}_k = \; & - \left(\sum_{tracks} \frac{1}{\sigma_{ik}^2} \left(\frac{\partial r_{ik}(\vec{a}_k)}{d\vec{a}_{k0}} \right) \left(\frac{\partial r_{ik}(\vec{a}_k)}{d\vec{a}_{k0}} \right)^T \right)^{-1} \\ & \cdot \left(\sum_{tracks} \frac{1}{\sigma_{ik}^2} \left(\frac{\partial r_{ik}(\vec{a}_k)}{d\vec{a}_{k0}} \right) r_{ik}(\vec{a}_{k0}) \right) \end{aligned} \tag{6.6}$$

where $\Delta\vec{a}_k$ denotes the vector of alignment corrections for module k, and i represents track number i. $\vec{a}_{k0}$ indicates that we derive numerically around the initial alignment parameters.

As mentioned above, the alignment procedure is ran iteratively to incorporate effects from module correlations. This is illustrated in Figure 6.8. After a first alignment of the detector, the modules are adjusted according to the calculated alignment parameters, and the tracking is rerun. The alignment is then ran again on the new tracks. After a given number of iterations, the alignment parameters are expected to converge to stable values.

6.4.2 Results with Simulated Data

Nominal Detector

A primary requirement of the alignment algorithm is that it converges to sensible results when ran on a perfectly aligned detector. The alignment parameters

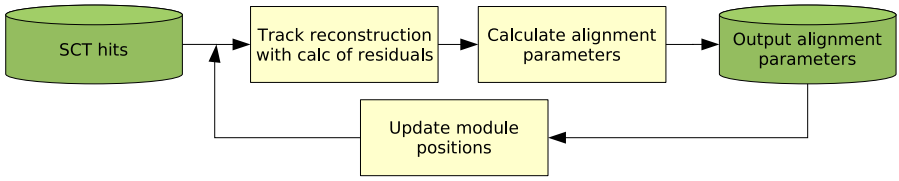

Figure 6.8: Data flow diagram for local χ^2 alignment.

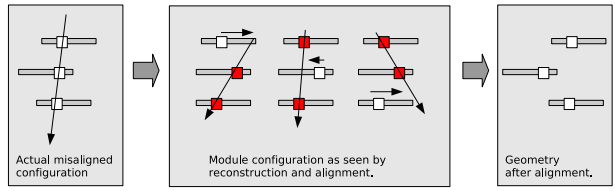

Figure 6.9: Example of overcorrection in local χ^2 when neglecting alignment correlations between modules.

for such a run are shown in Figure 6.10 for the *x*, *y* and *z* alignment parameters. Each curve on the plot shows the alignment parameter for a module as a function of number of iterations. One alignment parameter is shown per row, and one SCT layer per column. No constraints on the allowed alignment parameters were used in this run.

After the first iteration, the spread of the calculated alignment parameters is quite large, as a result of the neglection of module correlations. But already after the second iteration, the parameters have decreased significantly. However, there is an oscillating behaviour picking up after a few more iterations, especially in *y*. This can be attributed to overcorrections due to the neglection of correlations. The effect is illustrated in Figure 6.9. The illustration shows a misaligned detector, but the same argument applies in the nominal case, as an effective misalignment is introduced by the spread of alignment parameters in the first iteration. The effect arises when each module is moved to its "correct" position according to the χ^2 minimization, ignoring the impact this has on nearby modules. This will lead to an overcompensation, resulting in the observed oscillating behaviour.

A possible solution to this is to introduce a damping in the algorithm, multiplying the calculated alignment parameters with a factor < 1. This will make the algorithm converge more slowly, but at the same time allow the modules to gradually move into place. A run with a damping factor of 0.5 is shown in Figure 6.11. We see that the alignment parameters now converge steadily toward the expected zero.

The corresponding plots of α, β and γ show a similar converging behavior and this is illustrated in Figure 6.12.

	Module RMS			Barrel		
Misalignment set	$r\phi$ [μm]	z [μm]	r [μm]	$r\phi$ [μm]	z [μm]	r [μm]
sctdisp1	100	100	500	100	100	100
sctdisp2	100	100	500	200	200	200
sctdisp2rphi	100	-	-	200	-	-

Table 6.1: *Simulation misalignment sets. A misalignment of each individual module is picked from a gaussian distribution with the respective RMS. The same procedure is used to apply global shifts to the four barrel layers.*

Misaligned Detector

We now introduce misalignment in the simulation, and study the behavior of the alignment parameters in this context. The misalignment sets used in these studies are given in Table 6.1.

Figure 6.13 shows the flow of alignment parameters for a run with misalignment set *sctdisp1*, considered a realistic set. The damping factor is in this case 1.0. Like for the nominal detector alignment, the alignment parameters oscillate when no damping factor is applied. Do also notice the change of vertical scale with respect to the corresponding plots for the nominal detector. The oscillations in x and y show a coherent behaviour not seen in the case of nominal alignment. This is most likely due to the global shifts of barrels, causing a global feedback effect from the layer-to-layer correlations.

There is an intrinsic correlation between the x and y coordinate in the SCT local frame. A displacement of a module in x is equivalent to a displacement in y for the u/v (stereoangle) side of the module. Both misalignment in x and y could therefore in principle separately induce oscillations in both x and y. We therefore investigate the alignment parameter flow with the misalignment set *sctdisp2rhi*, which have only misalignment in $r-\phi$. The result can be seen in Figure 6.14. Even if there is no misalignment in the y coordinate, the oscillations are still induced by the overcompensation in x, although picking up a bit later than in the case of *sctdisp1*.

A run with *sctdisp2rphi* and a damping factor of 0.5 is shown in Figure 6.15. We see that there are some initial fluctuations, but that the algorithm converges nicely after some iterations. Notice again the change of vertical scale. The damping factor was put back to 1.0 from iteration 15, and we see that some modules wander off due to this, but are recovered. It can also be seen that additional modules are brought into play as the alignment proceeds. Figure 6.16 shows the corresponding plot for the three angular alignment parameters.

	Before alignment		After alignment	
	σ [μm]	mean [μm]	σ [μm]	mean [μm]
SCT layer0 sim	242.9 ± 23.8	30.4 ± 9.5	65.9 ± 0.3	-0.8 ± 0.2
SCT layer1 sim	245.6 ± 11.3	97.4 ± 9.1	54.6 ± 0.2	0.3 ± 0.2
SCT layer2 sim	130.7 ± 1.5	76.8 ± 1.6	51.1 ± 0.2	-0.2 ± 0.2
SCT layer3 sim	180.6 ± 4.3	-1.7 ± 1.8	68.3 ± 0.3	0.3 ± 0.2
SCT layer0 real	113.8 ± 1.1	-1.0 ± 0.8	80.0 ± 0.5	1.6 ± 0.4
SCT layer1 real	99.6 ± 0.7	2.3 ± 0.6	75.5 ± 0.4	0.4 ± 0.3
SCT layer2 real	96.1 ± 0.6	-5.7 ± 0.5	64.7 ± 0.3	-0.5 ± 0.2
SCT layer3 real	111.2 ± 1.0	0.6 ± 0.7	85.7 ± 0.5	-0.6 ± 0.4

Table 6.2: *Residuals for real and simulated data per barrel before and after alignment.*

6.4.3 Results with Real Data

Since the local χ^2 ran with a damping factor converges on a misaligned detector in simulation, it can be ran on real data. Figures 6.17 and 6.18 show the alignment parameter flow for a run on datasets 3007, 3038 and 3039 (36 217 events). The damping factor is also held here at 0.5 for the 15 first iterations, and then released to 1.0 as the parameters are stabilized. We see that the algorithm converges also on the real data, and we can now study how the residuals distributions change through the alignment procedure.

Figures 6.19 and 6.20 show the standard deviation (σ) and the mean of Gaussian fits to residuals as a function of iterations for the runs in Figure 6.15 and Figure 6.17 respectively. All layers show a converging behavior, both for the simulated and real data case. For the real data, there is a small offset of the converged mean value, especially for layer 0. The residuals per layer before alignment and after the last iteration are shown in Figure 6.21 for simulated data and in Figure 6.22 for real data. All layers show nice distributions after alignment, although the real data still has larger tails. The mean and σ of the fits are given in Table 6.2.

It is clear from the figures that the simulated misalignment shows significantly worse results than the real data case before alignment. This can be taken as an indication that the detector is built with a precision better than 100 μm on module level, and better than 200 μm layer-to-layer.

6.4.4 Summary and Conclusions

The local χ^2 alignment algorithm has been ran on cosmics data for a first study of the SCT barrel build precision. Although the quality of the cosmics data is worse than what one expects in ATLAS under LHC running, it is clear that an

improved alignment of the detector is achieved. In order to cope with oscillating behaviour in the alignment parameters due to neglection of correlations between modules, a damping factor had to be introduced in the alignment algorithm. By comparing the alignment results from real data with simulations of the expected build precision, it is clear that the SCT in its completed state is built well inside the specified precision.

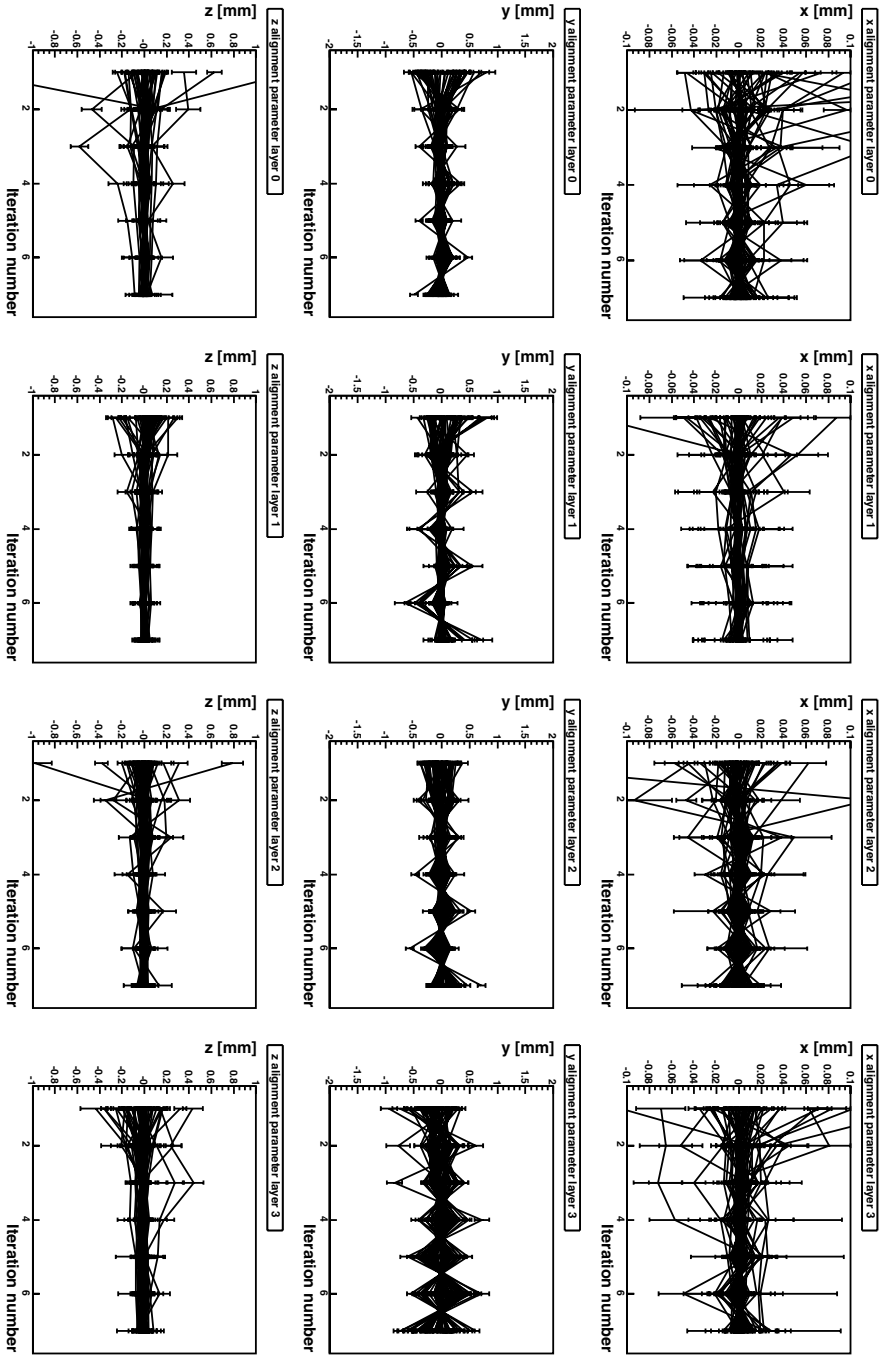

Figure 6.10: Alignment parameter x/y/z flow for nominal (perfect) SCT alignment, simulated data.

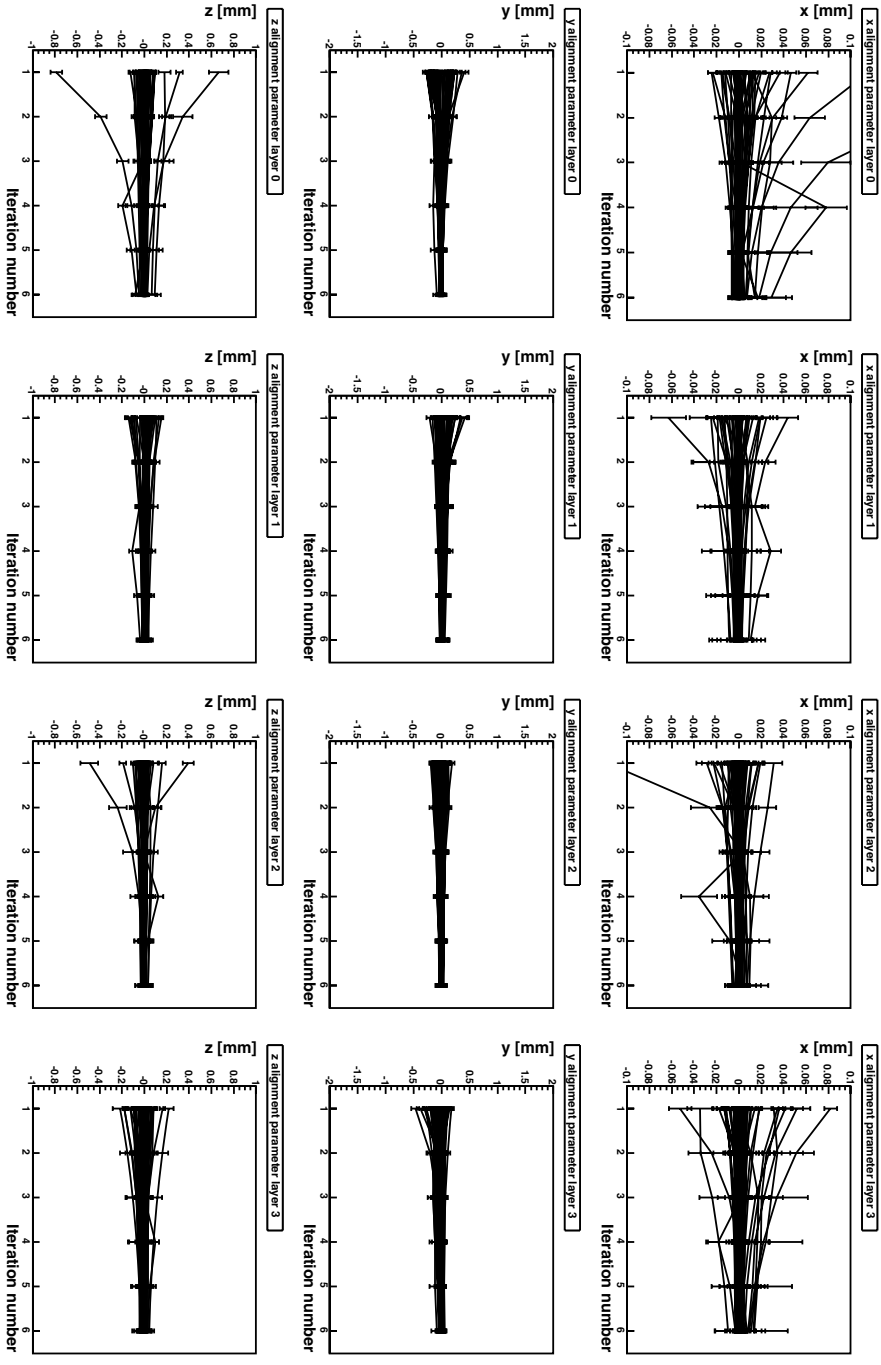

Figure 6.11: Alignment parameter x/y/z flow for nominal (perfect) SCT alignment with damping factor 0.5, simulated data.

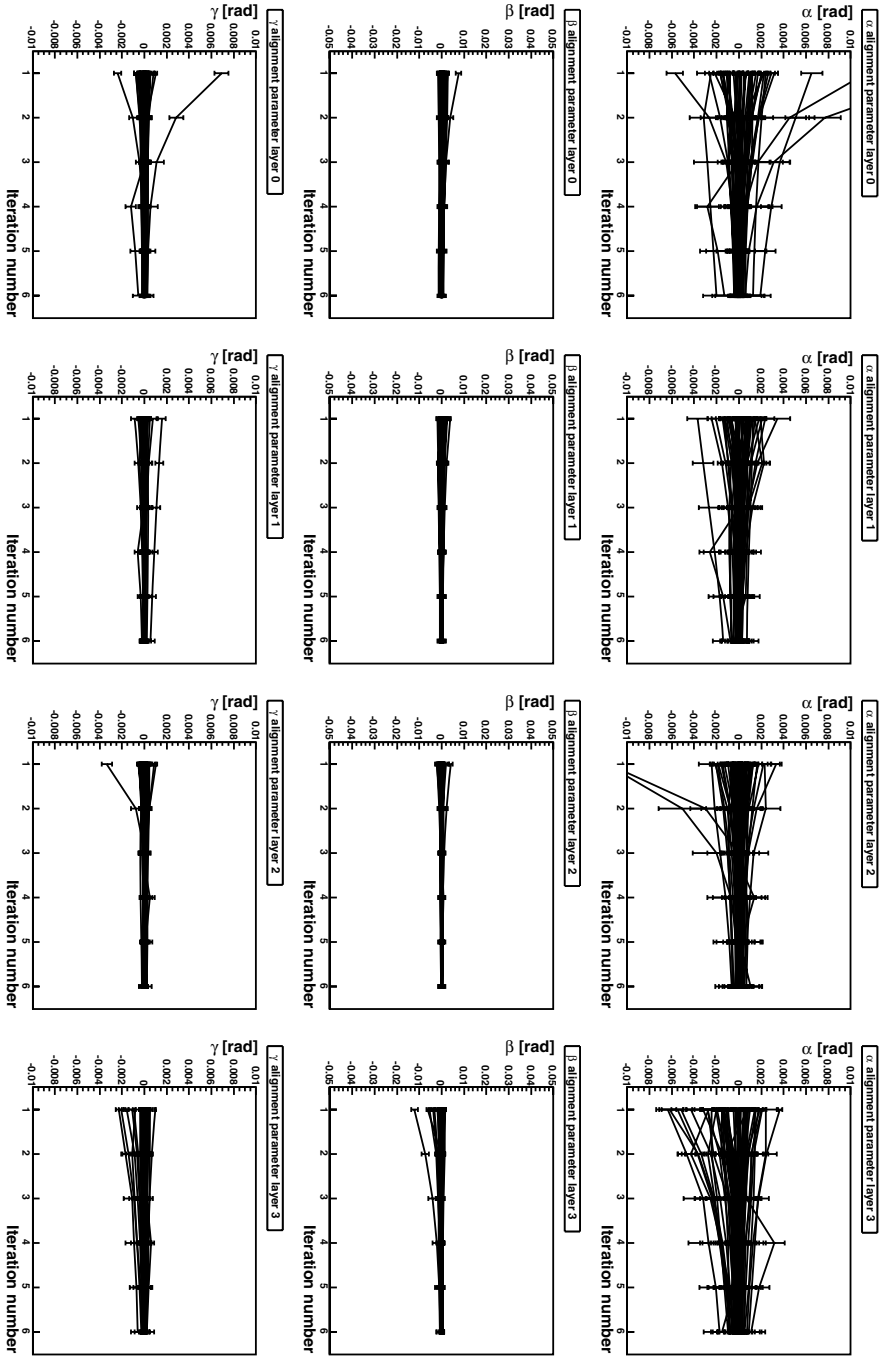

Figure 6.12: Alignment parameter $\alpha/\beta/\gamma$ flow for nominal (perfect) SCT alignment with damping factor 0.5, simulated data.

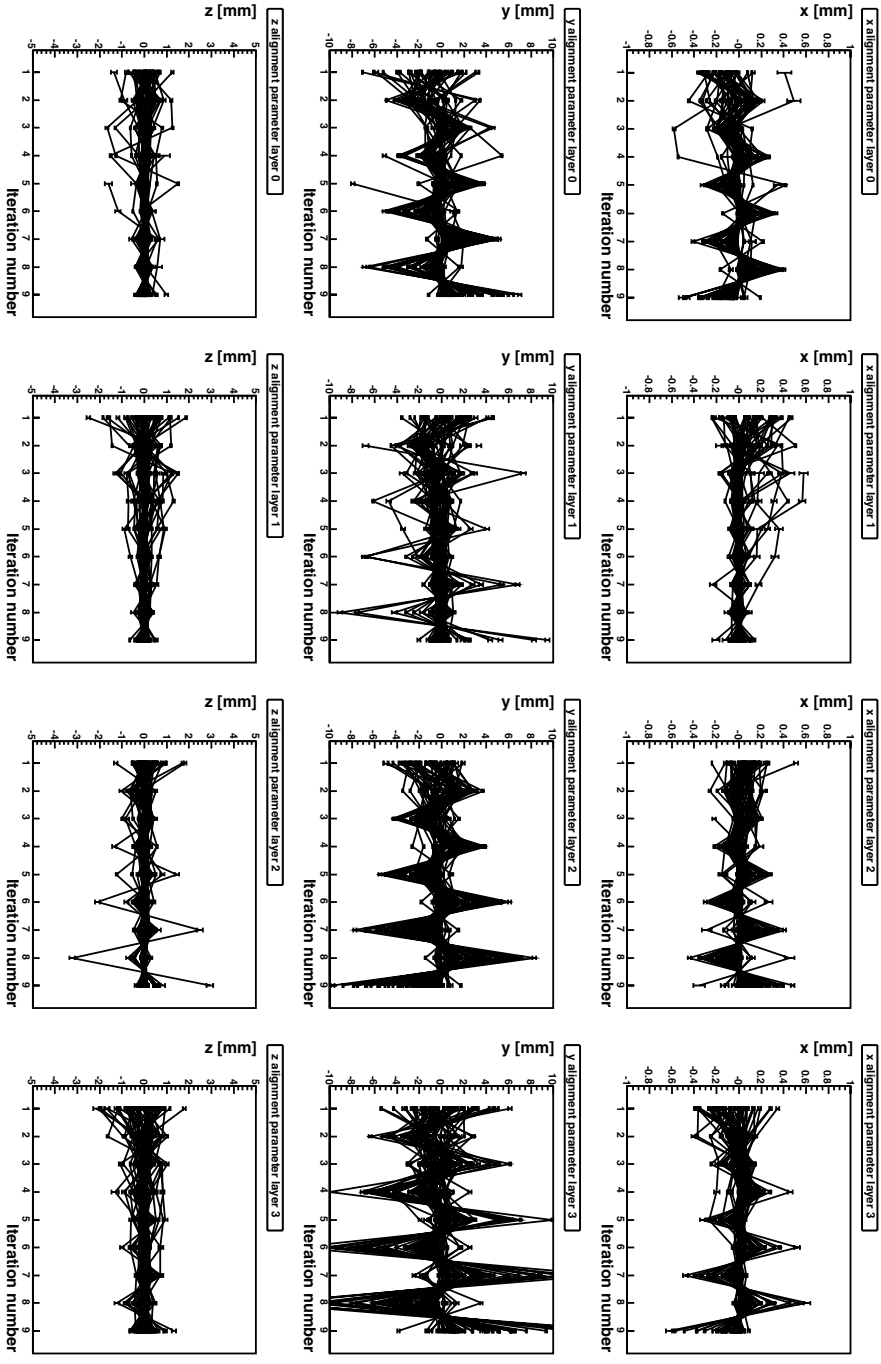

Figure 6.13: Alignment parameter x/y/z flow for sctdisp1 SCT misalignment, simulated data.

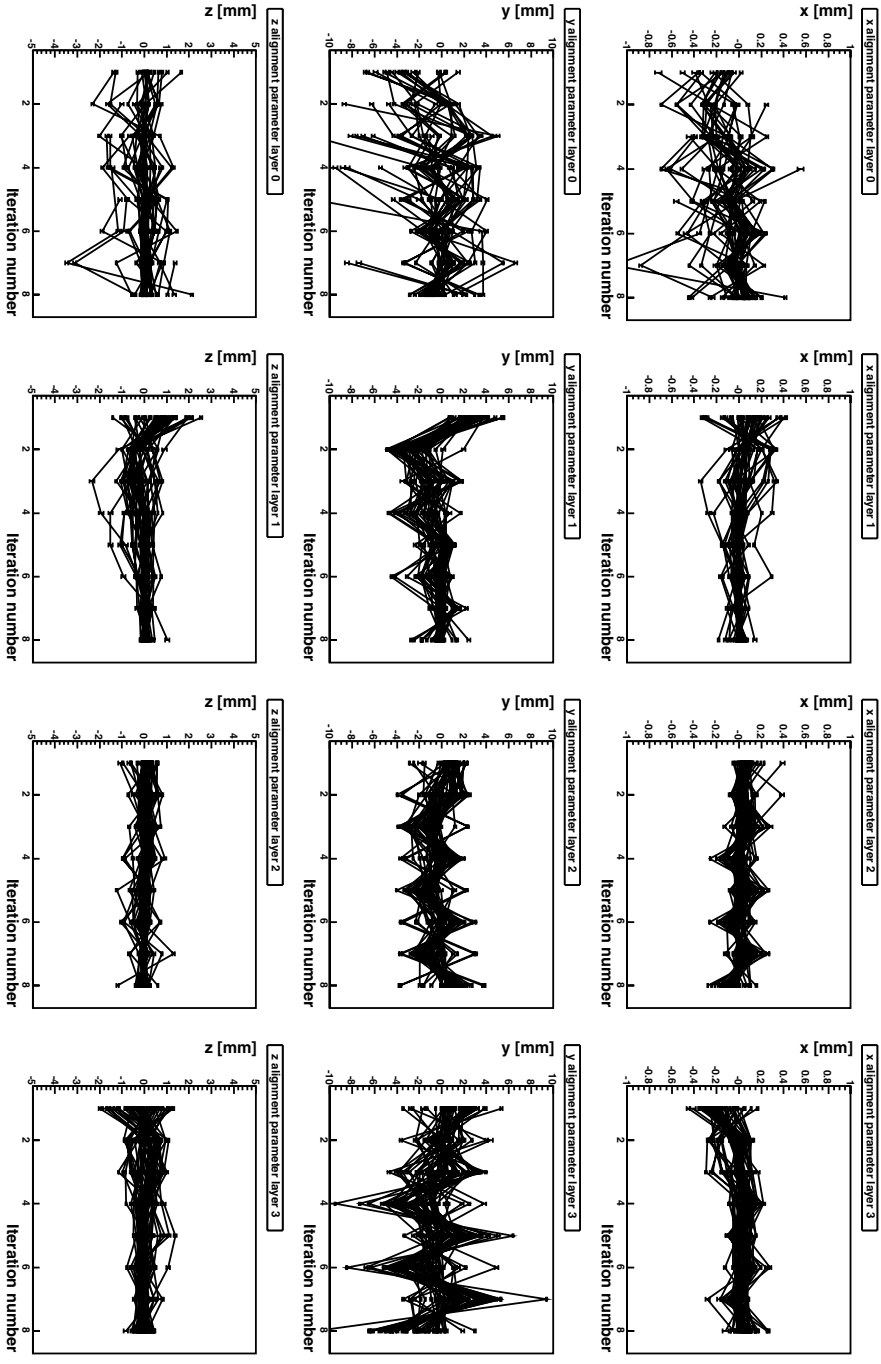

Figure 6.14: Alignment parameter x/y/z flow for sctdisp2rphi SCT misalignment, simulated data.

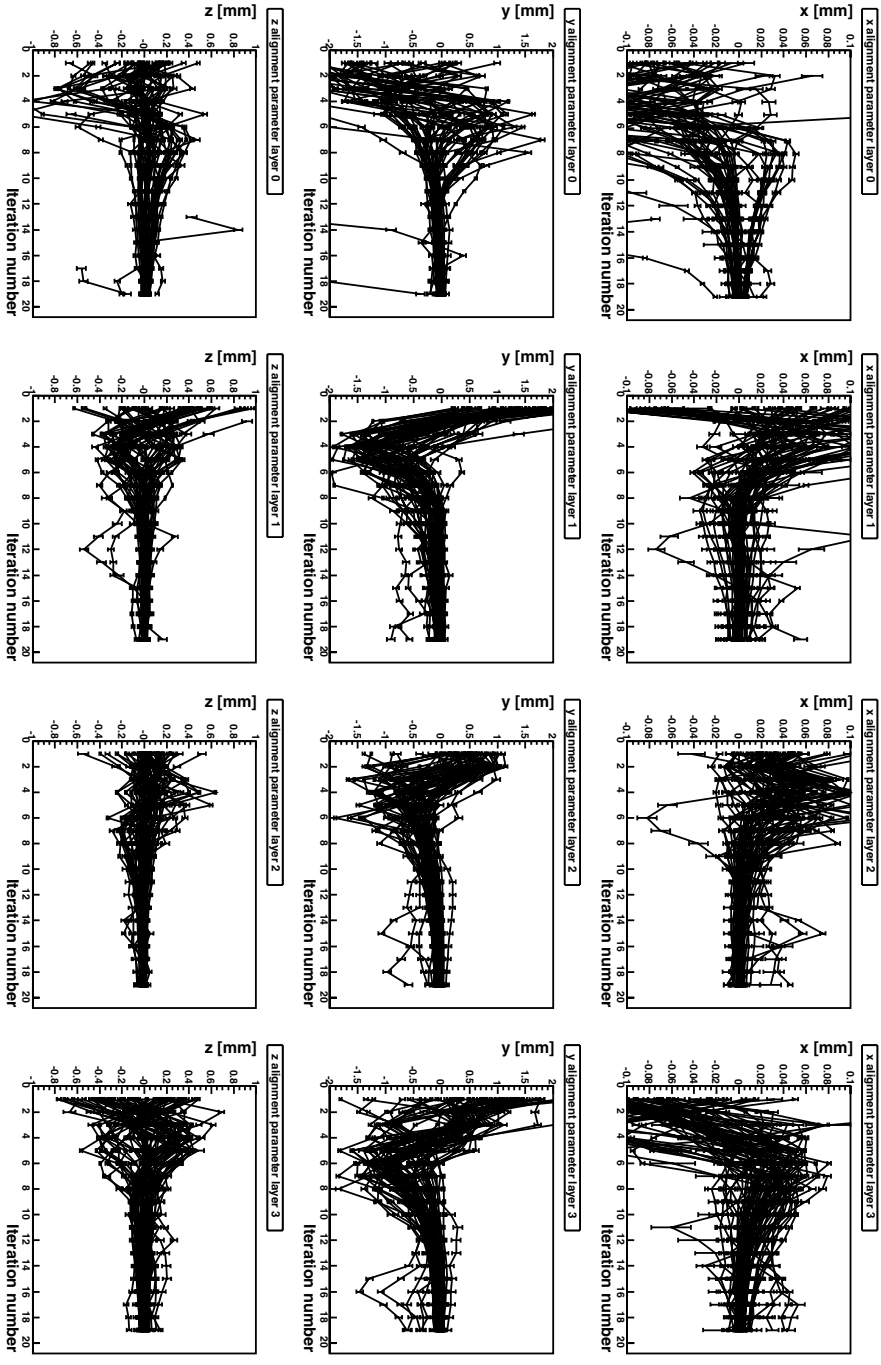

Figure 6.15: Alignment parameter flow x/y/z for sctdisp2rphi SCT misalignment with 0.5 damping factor, simulated data.

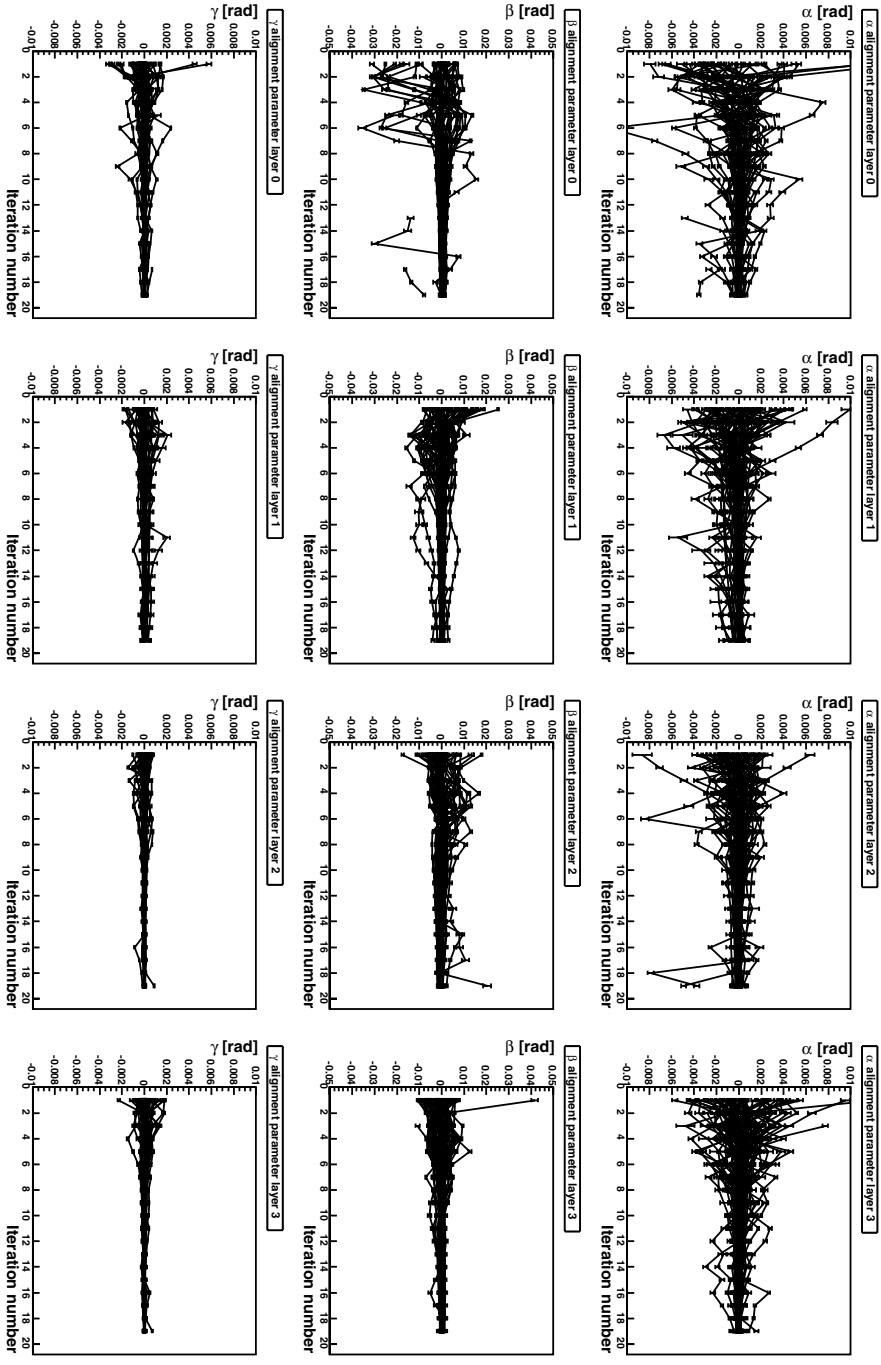

Figure 6.16: Alignment parameter $\alpha/\beta/\gamma$ flow for sctdisp2rphi SCT misalignment with 0.5 damping factor, simulated data.

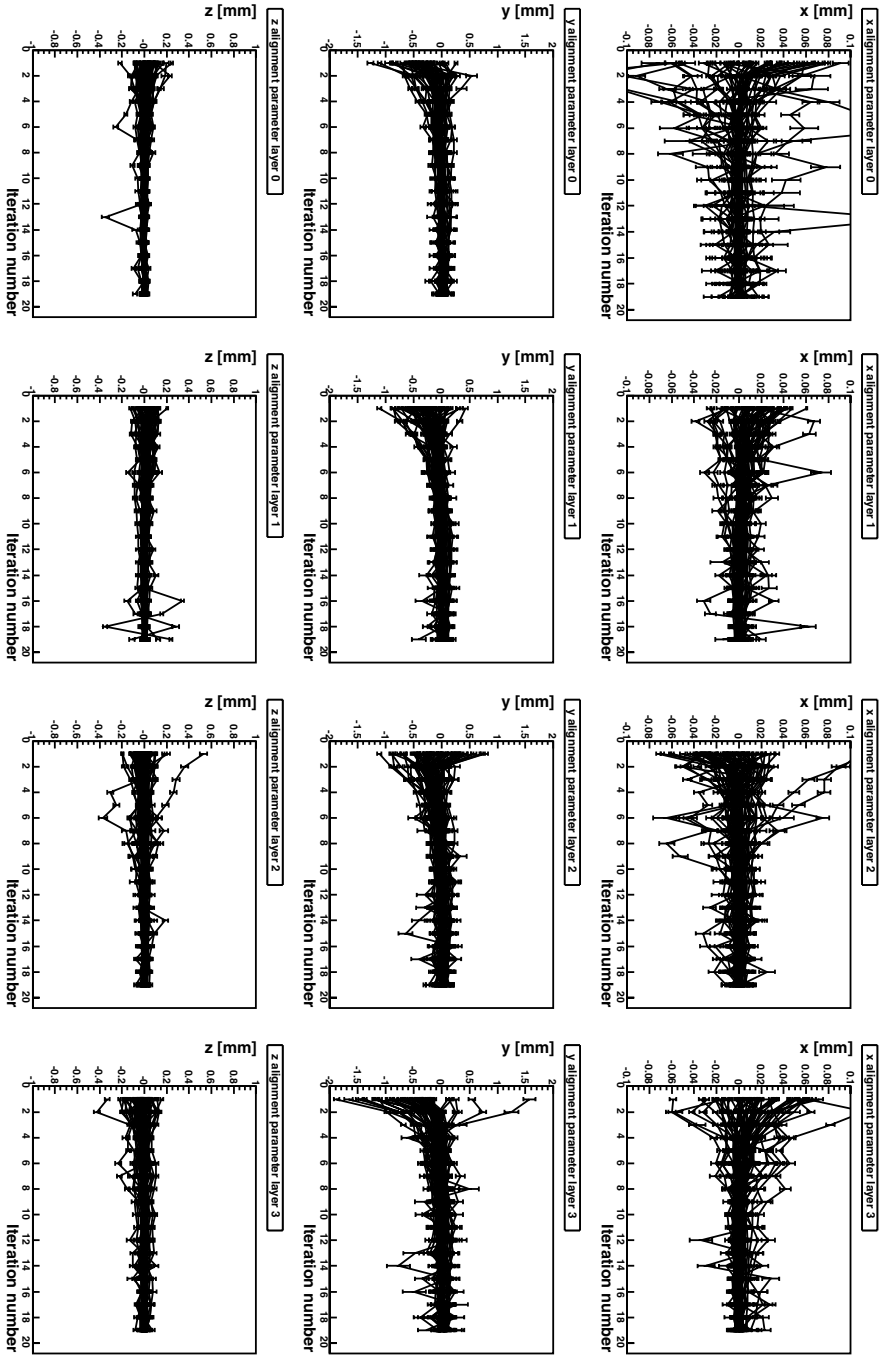

Figure 6.17: Alignment parameter flow for runs 3007, 3038, 3039. Damping factor is 0.5 for 15 first iterations, and then increased to 1.0.

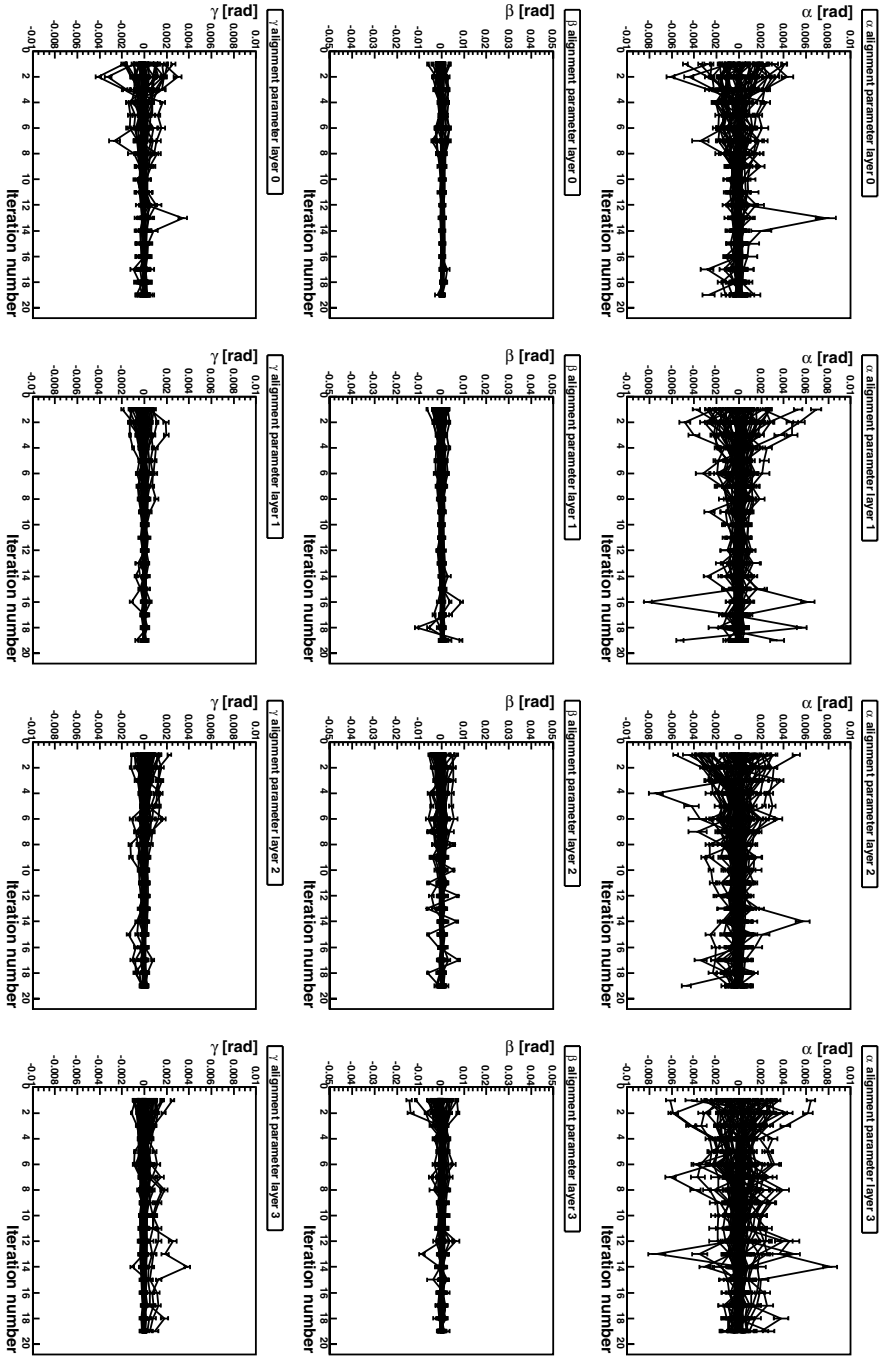

Figure 6.18: Alignment parameter flow for runs 3007, 3038, 3039. Damping factor is 0.5 for 15 first iterations, and then increased to 1.0.

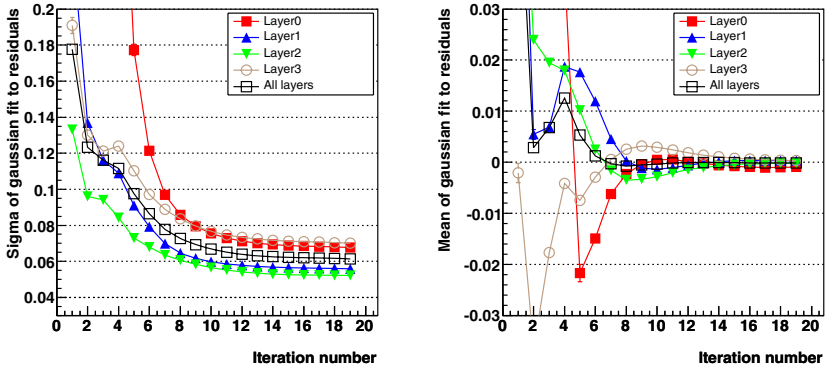

Figure 6.19: Fits to residuals as function of iteration number for simulated data.

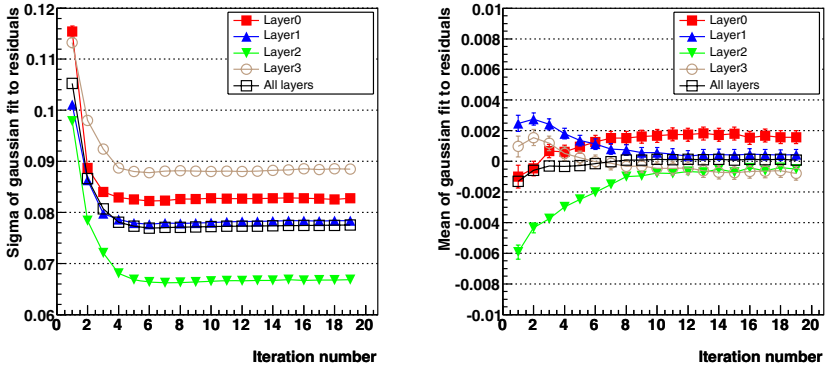

Figure 6.20: Fits to residuals as function of iteration number for real data.

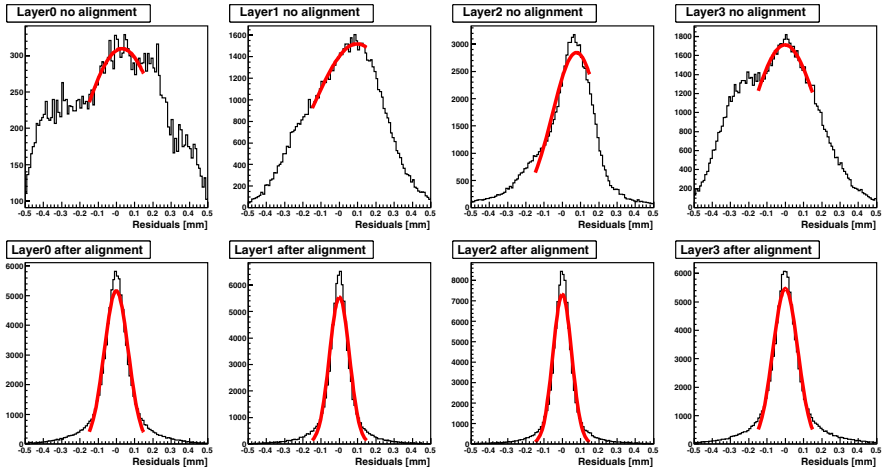

Figure 6.21: Residuals per layer for simulated data. Upper row shows residuals before alignment, lower row after.

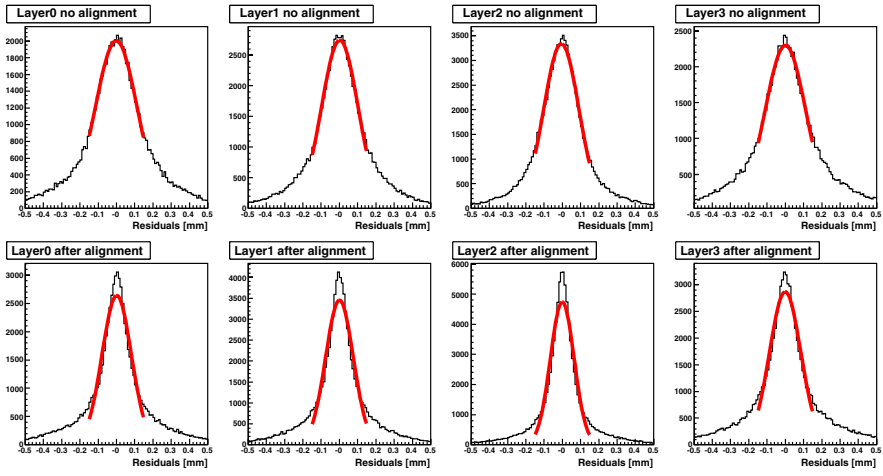

Figure 6.22: Residuals per layer for real data. Upper row shows residuals before alignment, lower row after.

7. Conclusions and Outlook

The first part of this thesis has been devoted to the ATLAS sensitivity to the existence of a charged Higgs boson. A charged Higgs boson discovery would be an unambiguous signal of physics beyond the Standard Model and in this thesis two studies are presented on the search for a charged Higgs boson with mass slightly below or higher than the top-quark mass. Such heavy charged Higgs bosons are produced in association with a top and a bottom-quark through the partly overlapping production processes $gb \to tH^{\pm}$ and $gg \to tbH^{\pm}$.

Due to a minimum in the charged Higgs boson production cross-section at $\tan\beta \sim 7$ it has so far not been possible to produce a charged Higgs boson discovery contour from SM decays which also covers the intermediate regions $6 \lesssim \tan\beta \lesssim 10$. Paper I addresses this problem by looking at a large-mass-splitting MSSM scenario in which the decay mode $H^{\pm} \to W^{\pm}H^0$ is open and receives a sizeable branching ratio in the intermediate $\tan\beta$ region. The study is made using ATLAS fast simulation and $t\bar{t}$ as the main background. Detection is, however, found to be impossible due to the small production cross-section of the signal and the lack of variables providing a good discrimination between background and signal.

While previous charged Higgs studies made use of either one of the two production modes listed above, Paper II makes use of a new event generator to combine them without double-counting, thus enabling production of charged Higgs boson both below, around and above the top-quark mass with a consistent description. In Paper II the production of charged Higgs bosons with masses from 165 GeV up to 600 GeV is studied in the $H^{\pm} \to \tau^{\pm}\nu$ decay mode. The study makes use of ATLAS full simulation and by far more complete background samples than in previous studies. As a starting point, a comparison is made between the new data and previous results and large discrepancies are encountered due to the more complete background samples. The second part of Paper II is hence devoted to the study of new selection variables and improvements to the previous methods to enhance the separation between signal and background. The final results show that a charged Higgs boson discovery is possible for all $\tan\beta$ for masses up to 160 GeV during the first three years of LHC running, extending up to 170 GeV in the following years. Above the top-quark mass a significant region in the $(\tan\beta, m_{H^{\pm}})$ parameter plane is also covered, extending from $\tan\beta \sim 15$ for $m_{H^{\pm}} = 200$ GeV and up to $\tan\beta \sim 35$ for $m_{H^{\pm}} = 600$ GeV for 100fb^{-1} integrated luminosity.

This thesis demonstrates the challenges in searching for a charged Higgs boson produced at the LHC. Both large integrated luminosity and excellent detector performance are needed. The $H^{\pm} \rightarrow \tau\nu$ decay mode offers the best discovery potential for the largest part of the $(\tan\beta, m_{H^{\pm}})$ parameter plane in the MSSM parameter space. Yet there are significant regions which are left uncovered and the detection of a charged Higgs boson at the LHC will depend upon whether supersymmetry is realised in nature with a favourable parameter configuration.

The second part of this thesis concerns the ATLAS semiconductor tracker (SCT) and its construction, testing and integration at CERN, cosmics data-taking and finally installation and commisioning inside the ATLAS detector.

In a joint collaboration between Norway and Sweden, the so-called "Scandinavian cluster" assembled, tested and shipped to the macro-assembly site some 320 SCT barrel detector modules. The silicon sensors were tested and approved at the University of Bergen before being shipped to the University of Oslo where 4 sensors were mounted onto a baseboard. Finally, the readout electronics were attached by Uppsala University and the finished module undervent extensive Quality Assurance (QA) tests before shipping. The results of these tests are presented in Paper III and show that 90% (84% excluding spares) of the produced modules meet the demanding specifications for the complete module. The result is in good agreement with the ATLAS assumed production efficiency of 85%, excluding spares.

The SCT barrels were assembled by Oxford University and once a barrel was finished and tested it was shipped to CERN where it was received and subject to reception tests. In this thesis an overview of the SCT DCS system has been presented and a detailed introduction has been given to the SCT power supply system, in particular its software implementation. The complete SCT power system comprises 88 crates, each supplying 48 modules with power. The size and complexity of the system requires substantial CPU power in order to handle data and command flows, and in Paper IV a so-called PVSS project tailored for the implementation of a power supply system running on several computers is presented. By making extensive usage of scripts and libraries throughout its implementation, the project is robust against programming mistakes but is also easily maintainable. For the final system installed in the ATLAS cavern, 8 local control stations control 11 power supply crates each, all of them supervised by the subdetector control station.

In February 2006 the 4 SCT barrels were joined together and inserted into the TRT barrel in the surface clean room building which housed all ATLAS Inner Detector activities at CERN. Together they formed the first combined detector element of the Inner Detector and during spring and summer of 2006 a series of cosmic runs were performed. The cosmics runs served to exercise the DCS and DAQ systems of both subdetectors, but also gave the unique opportunity to carry out first studies of the SCT detector's assembly precision, i.e. the alignment of the SCT barrel. For this thesis, work has been presented

for both DCS stability and performance during the cosmics runs, Paper V, and first alignment results obtained with the local χ^2 approach has been presented in Chapter 6. While the DCS performance during both the reception test and the later cosmics tests showed good stability, first alignment results revealed an unwanted feature where the alignment algorithm over-corrected the position of the module, thus introducing oscillations in the system. The problem was adressed using simulated data and solved by adding a damping factor to the corrections calculated by the alignment algorithm. By substituting simulated data with real data it was possible to show that the as-built-precision of the SCT barrel is well inside the design specifications.

The final integration of the SCT DCS into the ATLAS DCS will be through the use of a Finite State Machine (FSM). The FSM is a hierarchal control structure in which states are propagated upwards and commands downwards. Thus each level in the control tree needs to have a clearly defined state which can be read by its parent unit to evaluate the state of the level above. For the SCT power supply DCS it is natural to group the modules according to their cooling loops and define a common state for the cooling loop. This requires great care when designing the state rules for the loop since it should take into account all possible state combinations of the modules mounted on a single cooling loop. The loop state should give the best possible information about the system overall state and at the same time insure that information about any individual module failure is passed to the user.

During the last weeks of writing up this thesis the SCT power supply software developed as a part of this thesis has been succesfully deployed in the ATLAS cavern running on all local control stations and the subdetector control stations. The complete SCT barrel has been powered and read out by the DAQ as a part of the commissioning of the SCT inside ATLAS. The work presented for this thesis was thus shown to be of fundamental importance for the successful installation of the SCT detector.

8. Norsk populærvitenskapelig sammendrag

Hva er partikkelfysikk?: Om Standardmodellen og utvidelser av den

Partikkelfysikk er læren om de aller minste byggesteinene i naturen (vi kaller dem elementærpartikler), de som er ansvarlig for å bygge opp all den materie som omgir oss, både på jorden og i universet. Innenfor rammen av partikkelfysikk finner vi også beskrevet hvordan disse elementærpartiklene vekselvirker med hverandre, dvs hvordan de ulike partiklene virker på hverandre og ikke minst hvordan ustabile partikler kan gå over til andre partikler.

Det er altså ikke slik at alle elementærpartiklene er stabile, og faktum er at de fleste av dem har så kort levetid at vi bare kan studere dem ved noen store forskningssentre for partikkelfysikk rundt omkring i verden, noe vi skal komme tilbake til. I dag kjenner vi til 17 slike fundamentale partikler som vi kan dele i to klasser: 12 av dem hører hjemme i klassen vi kaller *fermioner* og det er disse partiklene som er ansvarlige for å bygge opp materie, mens de 5 siste er såkalte kraftformidlere, på fagspråket kalt *bosoner*. Bosonene er ansvarlig for å formidle de elektriske og magnetiske kreftene i naturen samt den sterke og svake kjernekraften i naturen. Tyngdekraften, som er den kraften som kanskje i størst grad påvirker vår hverdag, er derimot ikke en del av denne gruppen partikler, dvs den ville vært det om vi hadde lykkes detektere den partikkelen vi tror formidler tyngdekraften, men det har vi ikke.

Alt vi vet om partiklene som nevnt over er i dag sammenfattet i det vi i dag kaller *Standardmodellen*. Standardmodellen er en kvantemekanisk beskrivelse av naturen hvor hver elementærpartikkel i modellen er assosiert med et felt. Slike felt er funksjoner av tid og rom og sier noe om sannsynligheten for å finne en partikkel ved et gitt sted til en gitt tid. Uten sidestykke er Standardmodellen den i dag best eksperimentelt testede teori innenfor fysikkens fagfelt. Den ikke bare forutså eksistensen av flere partikler lenge før de ble eksperimentelt påvist, men den kunne også meget presist angi masse[1], elektrisk ladning og flere andre egenskaper ved partiklene. Senere kunne man gjennom eksperimentelle målinger fastlå at de målte størrelsene stemte svært bra med de teoretisk beregnede forutsigelsene.

Ett interessant aspekt ved Standardmodellen er at alle elementærpariklene i modellen i utgangspunktet er masseløse. Grunnen til det er at om vi gir par-

[1]Mer presist så kunne man med ved hjelp av modellen, og matematikken den bygger på, forutsi massene til $W^{\pm}$ og Z^0 bosonene. Øvrige partikler som Standardmodellen har spådd eksistensen av og som senere har blitt funnet har man ikke kunnet forutsi massen til.

tiklene masse på den, matematisk, mest opplagte måten så bryter faktisk modellen sammen og blir matematisk ubrukelig. Om vi ønsker en teori som kombinerer evnen til å forutsi fysikkfenomen med meget stor presisjon og som samtidig beskriver partikler som har masse, slik vi har målt med våre eksperiment, så må massen introduseres i modellen på en svært spesiell måte. Vi kaller måten masse er introdusert på i Standardmodellen for *Higgsmekanismen* etter den skotske fysikeren Peter Higgs som kom på ideen. Enkelt forklart så introduserer Higgsmekanismen i Standardmodellen en ny partikkel, ett Higgsboson, som har den egenskapen at den forander vakuumtilstanden i modellen og når våre vanlig partikler nå beveger seg gjennom vakumet så får de nå masse som vi kan identifisere med den vi eksperimentelt måler.

Dessverre så finnes det problemer med dette bildet og det kanskje største problemet er at man til dags dato ikke har funnet noe Higgsboson til tross for flere års søken. Dette er noe som plager partikkelfysikere verden over, men om de ikke har kunnet finne Higgsbosonet så har de ihvertfall kunnet sette en nedre grense for Higgsbosonets masse. Og det er her kommer et annet problem inn, nemlig at denne grensen for Higgsbosonets minste masse begynner å bli svært stor og nærmer seg en øvre grense for hvor stor den kan være uten at modellen vår igjen skal bryte sammen.

Det finnes flere grunner enn dem relatert til Higgsbosonet som gjør at de fleste partikkelfysikere i dag tror at Standardmodellen ikke er den komplette modell eller teori som kan beskrive alt det som hender på elementærpartikkelnivået. Vi skal ikke gå inn på detaljene om hvorfor her, men heller diskutere en mulig utvidelse av Standardmodellen, nemlig det vi kaller for *supersymmetri*.

Vi husker fra tidligere at vi i Standardmodellen har 12 fermioner og 5 bosoner. En supersymmetrisk modell bygger på antakelsen om at det finnes en symmetri mellom disse to typene partikler og at det til hvert fermion og boson i Standardmodellen finnes en superpartner. Superpartnerne har identiske egenskaper som deres partnere i Standardmodellen med det unntak at om Standardmodellpartikkelen er et fermion så er superpartneren et boson og motsatt for bosoner. Men om det var tilfelle så skulle vi jo ha observert slike superpartnere for lenge siden og det har vi ikke. En supersymmetrisk teori kan derfor ikke være helt symmetrisk, men bare "nesten", og når vi velger vår "nesten" supersymmetriske teori så velger vi den slik at alle superpartnerne er mye tyngre enn sine partnere i Standardmodellen og at vi derfor ikke har funnet dem enda.

Supersymmetriske modeller er svært interessante for partikkelfysikere fordi de kan gjøre det mulig å forklare flere av de observerte fenomon som Standardmodellen ikke kan forklare. Ett klassisk slik eksempel er at astronomer har observert og regnet ut at omtrent 22% av universet vi bor og lever i er laget av en type materie som ikke er med i Standardmodellen. Astronomene kaller den "mørk materie" for den kan bare observeres gjennom sin gravitasjonskraft, dvs den kan verken absorbere eller sende ut noe lys. Kanskje er

det slik at denne "mørke materien" er laget av nettopp superpartnerne i en supersymmetrisk teori?

I tillegg til superpartnerene så har også supersymmetriske modeller en annen særegenhet som gjør det mulig å skille dem fra Standardmodellen. De trenger nemlig så mange som 5 Higgsbosoner for at alle partiklene i modellen (både vanlige partiklene og de nye superpartnerne) skal få masse. To av disse Higgsbosonene vil da ha samme masse men like stor og motsatt elektrisk ladning. Fordi de to partiklene har samme masse sier vi at supersymmetriske modeller har et ladet Higgsboson og gir det symbolet $H^{\pm}$. Det ladete Higgsbosonet har altså en elektrisk ladning som gjør den grunnleggende forskjellig fra Standardmodellens ene Higgsboson som er elektriskt nøytralt. En oppdagelse av et ladet Higgsboson vil derfor være ett avgjørende funn som bekrefter at naturen er mer komplisert enn Standardmodellen og kanskje står vi overfor et supersymmetrisk scenario[2].

Litt om $E = mc^2$, partikkelakseleratorer og partikkeldetektorer

Da Einstein i 1905 publiserte sin spesielle relativitetsteori som blant annet inneholder den i dag berømte formelen $E = mc^2$ så hadde han neppe noen anelse om hvilke konsekvenser denne ene formelen skulle ha for verdenshistorien. Det interessante med formelen er at den kan leses to veier, og om vi leser den fra høyre til venstre så ser formelen at masse også er en form for energi. Det er dette som ligger til grunn for atombomben, hvor masse blir omgjort til bevegelsesenergi og fordi massen i formelen er multplisert med lysfarten i kvadrat (c^2) så blir mengden energi meget stor. I bomben som ble sluppet over Hiroshima mot slutten av andre verdenskrig ble bare 0.6 gram Uran gjort om til energi.

Om vi nå i stedet leser formelen fra venstre mot høyre så ser vi at vi fra energi også kan skape masse, og det er dette prinsippet vi benytter når vi i moderne partikkelfysikk bruker store partikkelakseleratorer til å skape nye og tyngre partikler som f.eks. Higgsbosonet. Ved CERN-laboratoriet utenfor Geneve bygges i dag det som skal bli verdens største og kraftigste partikkelakselerator. Den heter *Large Hadron Collider* (LHC) og innstalleres i en 27km lang sirkulær tunnel som ligger opptil 100m under bakken. I denne kommer protoner til akselereres til en energi som er 7 TeV per proton der TeV er en energienhet som brukes i partikkelfysikken. Grovt regnet er 1 TeV er omtrent like mye energi som en surrende mygg har, men det som gjør LHC så spesiell er at den komprimerer denne energien inn i ett volum som er en million million ganger mindre enn en mygg.

LHC har to protonstråler som sirkulerer hver sin vei og som skjærer hverandre ved 4 punkter langs med ringen. Ved disse punktene vil de høyenergetiske protonene kollidere med hverandre og i kollisjonsprosessen vil nye partikler kunne bli til ved at energien i kollisjonsprosessen gjøres om til partikler med

[2]Det finnes også andre modeller som ikke er supersymmetriske men som inneholder ladete Higgsbosoner.

masse. Mange av de partiklene som skapes er svært ustabile og vil derfor direkte henfalle, det vil si "sprenges i stykker", til andre partikler som så slynges ut fra kollisjonspunktet med farter tett oppunder lysfarten. I partikkelfysikken ønsker vi å studere disse såkalte henfallsproduktene, for med seg bærer de en signatur om det som ble skapt i kollisjonsprosessen.

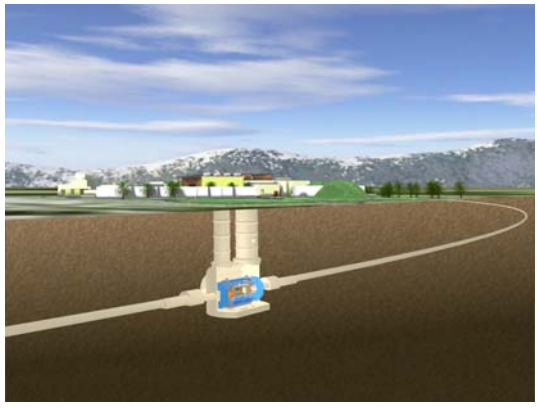

Figure 8.1: LHC vil akselere protoner og kollidere dem ved fire kollisjonspunkter langs med ringen. Vist på figuren er ATLAS eksperimentet ved det ene kollisjonspunktet.

Måten vi studerer henfallsproduktene på er at vi innstallerer store partikkeldetektorer rundt kollisjonspunktene og som partiklene vekselvirker med når de flyr ut fra kollisjonspunktet. En slik detektor er ATLAS (*A Toroidal Lhc ApparatuS*) som i skrivende stund installeres ved LHC. ATLAS har form som en sylinder og er 40m lang, 20m bred og veier 7000 tonn. Se figur 8.1, men også figur 4.1 i kapittel 4 i avhandlingen. Den innstalleres i en enorm hule rundt et av de fire kollisjonspunktene, og litt forenklet kan vi si et en slik detektor består av tre deler:

- **Spor-detektor:** Helt innerst mot kollisjonspunktet finner vi spor-detektoren som lager spor etter partiklene når de flyr ut fra kollisjonspunktet. Den kan bare se elektrisk ladete partikler for det er bare dem som reagerer med spor-detektoren på en slik måte at det skapes en liten elektrisk ladning i detektoren som kan leses ut. Avhengig av hvor den elektriske ladningen ble skapt i vår spor-detektoren så vet vi også hvor partikkelen passerte. Ved å lese ut mange slike elektriske ladninger kan spor-detektoren danne en rad med små punkter hvor partikkelen har passert gjennom og om vi trekker en linje fra punkt til punkt så finner vi det spor som partikkelen fulgte gjennom detektoren. Spor-detektorer sitter inne i ett svært sterkt magnetfelt og det gjør de fordi ladete partikler påvirkes av en kraft når de flyr gjennom magnetfeltet. Kraften tvinger partiklene inn i spiralformet bane og hvor liten eller stor denne spiralen er samt hvilken vei den "snurrer" avhenger av partikkelens fart og elektrisk ladning. Spor-detektoren kan ved å titte på de spiralformete sporene

altså bestemme både partikkelens fart samt hvilken elektrisk ladning den hadde.[3]

- **Kalorimetre:** Kalorimeteret sitter straks utenfor spor-detektoren og som navnet antyder så har denne som oppgave å måle partiklenes energi. Når partiklene kommer inn i ett kalorimeter så påvirkes de av de sterke elektriske felt som omgir atomkjernene og elektronene i materialet som kalorimeteret består av. Denne vekselvirkningen mellom partikkelen og kalorimeteret gjør at det dannes en skur av partikler som til slutt stopper helt opp i detektoren. Partikkelen avsetter altså sin energi i detektoren og litt avhengig av hvilken type partikkel vi måler energien til og hvilken type kalorimeter vi har med å gjøre så leses den avsatte energimengden, dvs den stoppede partikkelskuren, ut som synlig lys eller elektrisk ladning.
- **Myon-detektor:** Myoner er en type partikler som reagerer svært lite med detektoren når de flyr gjennom den og som derfor kan ta seg igjennom kalorimeteret som stopper stort sett alle andre partikler[4]. Til tross for at de reagerer lite med detektoren så reager de tilstrekkelig til at vi kan få laget ett spor av dem, og ved å ha en spor-detektor utenfor kalorimeteret så blir dette altså effektivt sett en myon-detektor fordi det er de eneste partiklene som kommer ut dit og som vi kan se. I ATLAS sitter også denne spor-detektoren i ett sterkt magnetfelt slik at vi kan måle myonets fart/bevegelsesmengde og ladning.

Hva har så jeg gjort?

Om arbeidet som har ledet frem til denne doktorgraden skal sammenfattes i ett bilde så er kanskje Figur 8.2 en bra illustrasjon. Figuren viser partikler som flyr ut fra en kollisjonen i ATLAS detektoren der et ladet Higgsboson har blitt produsert, men som på grunn av sin korte levetid umiddelbart har henfalt til de partiklene som vi ser på figuren. I artiklene Paper I og Paper II som er blitt presentert for denne avhandlingen har jeg altså studert muligheten for å detektere ladete Higgsbosoner med ATLAS detektoren. Dette har jeg gjort ved å simulere både produksjonen og henfall av ladete Higgsbosoner samt responsen som detektoren gir. I den første artikkelen har vi tittet på en spesiell versjon av supersymmetri der vi velger parametrene for modellen slik at massene til de 5 Higgsbosonene blir svært forskjellige og hvor et ladet Higgsboson kan henfalle til det tyngste av de nøytrale Higgsbosonene. Studien var dessverre mislykket å så henseende at når man inkluderer bakgrunner, dvs andre fysikkprosesser som ser nesten lik ut til produksjonen av ett ladet Higgsboson, men som det generelt produseres mangfoldige ganger mer av, så var det ikke mulig å finne det ladete Higgsbosonet. I Paper II har vi studert muligheten

[3]Teknisk sett så er det ikke partikkelens fart spor-detektoren bestemmer, men det vi kaller partikkelens bevegelsesmengde som er en funksjon av farten og massen.

[4]Det finnes nå få andre unntak i tillegg til myonene som ikke reagerer med kalorimeteret, men disse er tilnærmet helt usynlige og observeres derfor aldri ved slike partikkeldetektorer som omtales her.

for å detektere det ladete Higgsbosonet i en annen henfallskanal, denne gangen innenfor rammen av det vi kan kalle “vanlig” supersymmetri. Resultatene viser at avhengig av modellens parametre[5] så finnes det gode muligheter for å detektere et ladet Higgsboson ved ATLAS og om det ladete Higgsbosonet har en liten masse så kan vi gjøre regning med å finne det allerede etter ett års kjøring av LHC og datasamling med ATLAS detektoren.

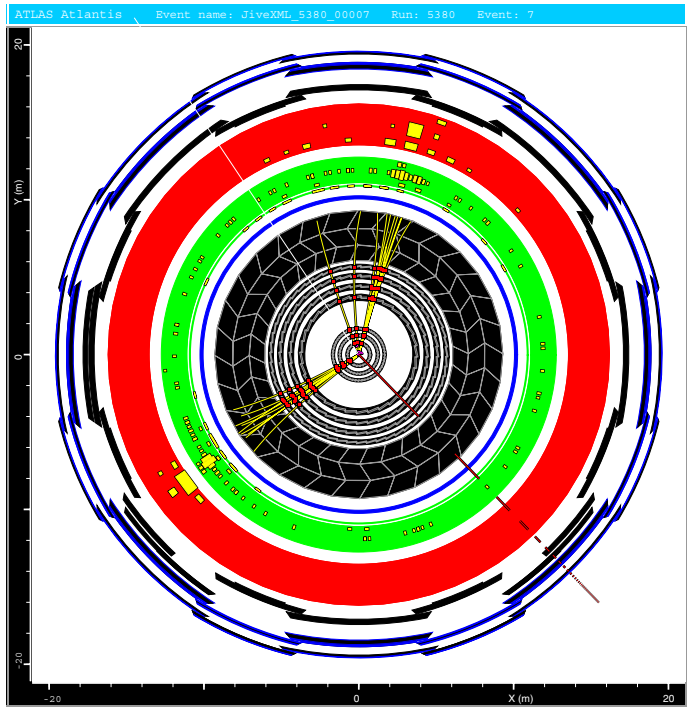

Figure 8.2: Produksjon og henfall av et ladet Higgsboson i ATLAS detektoren. På bildet har vi zoomet ekstra inn på sporene som lages i spor-detektoren og vist som røede små punkter er punktene som spor-detektoren lager for å kunne rekonstruere sporet. De fire ytterste punktene på hvert spor er laget av SCT detektoren. Utenfor spor-detektoren ser vi i grønt og rødt kalorimetrene som stopper partiklene og måler deres energi. Helt ytterst finner vi myon-detektoren.

Men la oss gå tilbake til Figur 8.2 og observere at bildet er ikke helt i riktig skala. Ett såkalt fish-eye perspektiv har blitt brukt for å zoome ekstra inn på spor-detektoren og den delen av spor-detektoren som heter ATLAS Semi-Conductor Tracker (SCT). Artiklene Paper III, IV og V samt kapitlene 5 og 6 i denne avhandlingen handler alle sammen om SCT detektoren. SCT detektoren er en av 3 spor-detektorer i ATLAS som sitter i hva vi kaller ATLAS

[5]Resultatene er avhengig av modellens parametre fordi disse bestemmer hvor tung det ladete Higgsbosonet er, hvor ofte det produserer i kollisjonene samt hvilke typer partikler det henfaller til.

Inner Detector. Den er bygget opp av Silisium halvleder detektorer[6] som er 6x6cm store og 4 slike utgjør en SCT detektor modul (se figurene 5.1 og 5.2 i avhandlingens kapittel 5). Totalt finnes det 4088 SCT detektor moduler i SCT detektoren og 320 av dem ble bygget i ett samarbeidsprosjekt mellom Norge og Sverige. Jeg var med på dette og testet de ferdigbygde modulene i Uppsala før de ble sendt til Oxford for å monteres sammen på tønner. Det er dette arbeidet som er presentert i Paper III.

I Oxford ble detektor modulene montert på 4 store tønner (se figur 5.6 i avhandlingens kapittel 5) som senere ble sendt til CERN hvor de ble skjøvet sammen i hverandre og utgjør det vi kaller SCT barrel. I andre halvdel av del av denne avhandlingen er mitt arbeid relatert til detektor kontrollsystemet presentert. Hver enkelt detektor modul trenger strøm, og den trenger både høy- og lavspenning. Jeg har jobbet med å designe og utvikle den software som skal til for å kunne kontrollere strømforsyningen til SCT detektoren. Ett dataprogram, kalt MoPS, har blitt utviklet og er beskrevet i artikkel Paper IV. Programmet har blitt brukt å kjøre detektoren både under testing og senere etter at detektoren har blitt innstallert i ATLAS. Resultater fra testene og analyser av detektorkontrollsystemet er presentert i Paper V hvor jeg da i hovedsak har jobbet med strømforsyningen.

Helt til slutt har jeg også jobbet med å analysere kosmiske data som ble samlet inn av SCT tønnen etter at den var montert sammen og fremdeles stod oppe på bakken. Disse dataene kan brukes til å linjere opp detektoren (alignment), dvs om noen detektor moduler ikke er plassert på nøyaktig det stedet de skulle så kan man kompensere for dette etterpå. Våre studier tyder på at SCT detektoren er montert med en presisjon som er bedre enn den som var på forhånd antatt, og at vi kan korrigere for de små avikene som finnes.

Som en oppsummering så kan vi si at jeg har vært med på en partikkelfysisk reise der jeg har fulgt SCT detektoren gjennom hele dens fødsel. Jeg har vært med på å bygge den, teste den og til slutt innstallere den i ATLAS. I parallell med dette arbeidet har jeg også utforsket mulighetene for at ATLAS skal kunne detektere ett ladet Higgsboson. Denne muligheten er slett ikke ubetydelig og om noen år burde vi kunne vite svaret.

[6]Disse detektorene ligner faktisk svært meget på fotocellene som man finner så mange steder i dagliglivet.

9. Acknowledgements

The work presented in this thesis is the sum of almost 4 years of work. During those years I've met a lot of nice and helpful people and I would like to take this opportunity to thank some of all the people who have supported me during the journey:

First of all I would like to thank my supervisor Bjarne Stugu and my co-supervisors Richard Brenner and Tord Ekelöf at Uppsala University. I would like to warmly thank you all for giving me the freedom to persue my own scientific ideas and for giving me support and rescuing me whenever I ended up in trouble.

I would like to thank Pamela Ferrari for introducing me to the SCT power supply software and for having faith in me when I started redesigning it. During the last 2 years I've also had the privelege of working with Peter W. Phillips whose knack for finding elegant solutions is extraordinary.

Several of my fellow students deserve a warm thank you, most prominently Ola K. Øye for countless discussions on physics and non-physics topics, never ending support on all kinds of problem and for being a superb travelling companion, room mate and close friend during several years. Are R. Raklev also deserves my warmest gratitude for all his help on the theoretical aspects of particle physics, but even more important for his enjoyable attitude to life and for cheering me up whenever I needed it. Or at least share the same depressions. Physics would not have been the same without the two of you!

When I first came to Uppsala Nils Gollub introduced me to the search for charged Higgs bosons and probably without knowing it paved the way for the following 3 years of my research. Later I became the one to bring the charged Higgs heritage on to new generations of students and it was a pleasure to do so and introduce Martin Flechl to the field. His ideas, working capacity, perfectionism and not to forget personality makes him an outstanding person to collaborate with. Thank you both for being good collaborators and great friends.

Several other students and employees have enlivened my everyday life and helped me out with various problems: Christian, Camille, Elias, Henrik, Lars Erik, Mattias, Michael and Trygve thus all deserve an applause. I would also like to thank my close friends Jonas and Åsa for all the great times we have spent together in Uppsala and for all the great times to come.

Ever since the days of my childhood I've had a unique friend in Stig Wergeland who has always been there for me whenever needed. I owe him my deep-

est gratitude for his support, for bearing over with my whining when the work load has been killing me and for putting life in general in perspective. This autumn we will again go hiking!

I don't know if my interest for physics originates from my mother or father but it's without any doubt their credit that I now hand in this thesis. They have been ever supportive and encouraging and even though they during the later years perhaps not fully grasped what I was working on they never stopped showing interest in my results. I'm also thankful to my two sisters for bringing out the shovel and digging me out from underneath a pile of books when I had gone too far in my search for the smallest building blocks of nature. They do not always hide in books.

Last, but not least, I would like to thank the two loves of my life; Karin and our daughter Emilia. Thank you Karin for being the person you are, for being there for me during all these years, for supporting me and for donating me to science during the last 6 months of this thesis. Thank you Emilia for being such a wonderful bundle of joy, and for occupying your father's bed with your 60cm and 5.5kg.

A. Acronyms

Below some of the most frequently used acronyms are listed:

ABCD3TA	Readout chip used on the SCT detektor module
ASIC	Application Specific Integrated Circuit
ATLFAST	Atlas fast simulation package
BeO	Beryllium Oxide
BR	Branching Ratio
BT	Barrel Toroid, part of the ATLAS magnet system
CAN	Communication Area Network
CC	Crate Controller (SCT)
CS	Central Solenoid or Cooling System (SCT)
CU	Control Unit (FSM)
CSC	Cathode Strip Chamber, part of the ATLAS Muon Spectrometer
CTB	Combined Test Beam
DAQ	Data Acquisition
DCS	Detector Control System
DDC	DAQ-DCS Communication
DIM	Distributed Information Management
DSS	Detector Safety System
DU	Device Unit (FSM)
EC	End-Cap
ECT	End-Cap Toroid, part of the ATLAS magnet system
EEPROM	Electrically Erasable Programmable Read-Only Memory
EF	Event Filter (Third trigger level at ATLAS)
ELMB	Embedded Local Monitoring Board
EM	Electromagnetic
ENV	Environmental project (SCT)
FCAL	Forward Calorimeter, part of the ATLAS hadronic calorimetry
FCNC	Flavor Changing Neutral Current
FSM	Finite State Machine
GEANT4	GEometry ANd Tracking (toolkit simulating particles passing matter)
GUT	Grand Unified Theory
HCAL	Hadronic Calorimeter
HEC	Hadronic End-Cap, part of the ATLAS hadronic calorimetry
HepMC	HEP Monte Carlo format (standardized output format of event generators)
HLT	High Level Trigger (LVL2 and EF)
HV	High Voltage

ID	Inner Detector, part of the ATLAS Detector
IS	Interlock System (SCT)
JCOP	CERN Joint Controls Project
LAr	Liquid Argon (Calorimeter), part of the ATLAS calorimetry
LCS	Local Control Station (DCS computer)
LO	Leading Order
LSP	Lightest Supersymmetric Particle
LU	Logical Unit (FSM)
LVL1	Level 1 (Trigger)
LVL2	Level 2 (Trigger)
MC	Monte Carlo
MDT	Monitored Drift Tube, part of the ATLAS Muon Spectrometer
MoPS	Monitoring Power Supply (SCT)
MSSM	Minimal Supersymmetric Standard Model
NLO	Next-to-Leading Order
OPC	OLE for Process Control
PPM	Power Pack Monitoring (SCT)
PS	Power Supply (SCT)
RMS	Root Mean Square
RoI	Region of Interest
RPC	Resistive Plate Chambers, part of the ATLAS Muon Spectrometer
SIC	System Interlock Card (SCT)
SCAND	SCANDinavian cluster, production group for SCT modules
SCS	Subdetector Control Station (DCS computer)
SCT	Semiconductor Tracker, part of the ATLAS ID
SM	Standard Model
SUSY	SUperSYmmetry
tauRec	tau Reconstruction algorithm, used in ATLAS offline reconstruction
TDAQ	Trigger and Data Acquisition
TE	Thermal Enclosure, seperates the SCT and TRT detectors
THDM	Two Higgs Doublet Model
TGC	Thin Gap Chamber, part of the ATLAS Muon Spectrometer
TileCal	Tile Calorimeter, part of the ATLAS hadronic calorimetry
TPG	Thermal Pyrolytic Graphite
TRT	Transition Radiation Tracker, part of the ATLAS ID
TTC	Trigger, Timing and Control
QA	Quality Assurance

Bibliography

[1] V. M. Abazov et al. Direct search for charged higgs bosons in decays of top quarks. *Phys. Rev. Lett.*, 88:151803, 2002. hep-ex/0102039.

[2] B. Abbott et al. Search for charged higgs bosons in decays of top quark pairs. *Phys. Rev. Lett.*, 82:4975–4980, 1999. hep-ex/9902028.

[3] A Abdesselam and T Akimoto. The barrel modules of the atlas semiconductor tracker. Jul 2006. ATL-INDET-PUB-2006-005. ATL-COM-INDET-2006-009. CERN-ATL-COM-INDET-2006-009.

[4] A. Abulencia et al. Search for charged higgs bosons from top quark decays in $p\bar{p}$ collisions at $\sqrt{s} = 1.96$-tev. *Phys. Rev. Lett.*, 96:042003, 2006. hep-ex/0510065.

[5] A large ion collider experiment, Technical Proposal. CERN/LHCC/95-71, 1995.

[6] Johan Alwall. An improved description of charged higgs boson production. 2004. hep-ph/0410151.

[7] Johan Alwall and J. Rathsman. Improved description of charged higgs boson production at hadron colliders. *JHEP*, 12:050, 2004. hep-ph/0409094.

[8] Ketevi A. Assamagan and Nils Gollub. The atlas discovery potential for a heavy charged higgs boson in g g –> t b h+- with h+- –> t b. *Eur. Phys. J.*, C39S2:25–40, 2005. hep-ph/0406013.

[9] Ketevi Adikle Assamagan, Yann Coadou, and Aldo Deandrea. Atlas discovery potential for a heavy charged higgs boson. *Eur. Phys. J. direct*, C4:9, 2002. hep-ph/0203121.

[10] ATLAS Computing Technical Design Report. CERN/LHCC/2005-022, 2005.

[11] ATLAS Detector and Physics Performance Technical Design Report. CERN/LHCC/99-15, 1999.

[12] R. Barate et al. Search for the standard model higgs boson at lep. *Phys. Lett.*, B565:61–75, 2003. hep-ex/0306033.

[13] C. L. Bennett et al. First year wilkinson microwave anisotropy probe (wmap) observations: Preliminary maps and basic results. *Astrophys. J. Suppl.*, 148:1, 2003. astro-ph/0302207.

[14] C. Biscarat and M. Dosil. Charged higgs search in top quark deceays with the atlas detector. 2003. ATL-PHYS-2003-038.

[15] Bingefors N. Brenner R. and Mohn B. Evaluation of a humidity sensor for use in an environment exposed to radiation. *Accepted by Journal of Testing and Evaluation*. JTE100272-06R.

[16] P Brückman, A Hicheur, and S J Haywood. Global chi2 approach to the alignment of the atlas silicon tracking detectors. Technical Report ATL-INDET-PUB-2005-002. ATL-COM-INDET-2005-004. CERN-ATL-INDET-PUB-2005-002, CERN, Geneva, 2005.

[17] F. Campabadal et al. Design and performance of the abcd3ta asic for readout of silicon strip detectors in the atlas semiconductor tracker. *Nucl. Instrum. Meth.*, A552:292–328, 2005.

[18] CAN in Automation (CiA): http://www.can-cia.de.

[19] Masud Chaichian and Nikolai F. Nelipa. *Introduction to Gauge Field Theories*. Springer–Verlag Berlin Heidelberg, 1984.

[20] The compact muon solenoid, Technical Proposal. CERN/LHCC/94-38, 1994.

[21] P. D. B. Collins, A. D. Martin, and E.J. Squires. *Particle physics and cosmology*. John Wiley & Sons, Inc., 1989.

[22] T G Cornelissen. Ctbtrackingtrack reconstruction for the testbeam and cosmics. Technical Report ATL-INDET-INT-2006-001. ATL-COM-INDET-2006-003, CERN, Geneva, Mar 2006.

[23] Michael Dine and Willy Fischler. A phenomenological model of particle physics based on supersymmetry. *Phys. Lett.*, B110:227, 1982.

[24] John R. Ellis. Beyond the standard model for hillwalkers. 1998. hep-ph/9812235.

[25] Jose Ramon Espinosa and Ren-Jie Zhang. Complete two-loop dominant corrections to the mass of the lightest cp-even higgs boson in the minimal supersymmetric standard model. *Nucl. Phys.*, B586:3–38, 2000. hep-ph/0003246.

[26] Brenner R. *et al. Interlock card specifications*. ATL-IS-ES-085, EDMS id 385793.

[27] Gornicki E. *et al. Crate controller specifications*. ATL-IS-ES-088, EDMS id 385796.

[28] Malecki P. *et al. HV card specification.* ATL-IS-ES-0084, EDMS id 385792.

[29] Framework - Finite State Machine: http://lhcb-online.web.cern.ch/lhcb-online/ecs/fw/fwfsm.html.

[30] Sandaker H. *SemiConductor Tracker Development and Physics Simulation*. PhD thesis, University of Oslo, 2005. ISSN 1501-7710.

[31] C. Hansen, N. Gollub, K. Assamagan, and T. Ekelof. Discovery potential for a charged higgs boson decaying in the chargino neutralino channel of the atlas detector at the lhc. *Eur. Phys. J.*, C44S2:1–9, 2005. hep-ph/0504216.

[32] R. Härtel. Iterative local χ^2 alignment approach for the ATLAS SCT detector. Master's thesis, Max-Planck Institut für Physik, Werner Heisenberg Institut, Münich, 2005.

[33] A. Heister et al. Search for charged higgs bosons in e+ e- collisions at energies up to s**(1/2) = 209-gev. *Phys. Lett.*, B543:1–13, 2002. hep-ex/0207054.

[34] A. Hicheur. Selecting good tracks for alignment in sr1 cosmics run. 2005.

[35] Stastny J. *LV card specification*. ATL-IS-ES-0083, EDMS id 385791.

[36] CERN Joint Controls Project: http://itco.web.cern.ch/itco/projects-services/jcop/.

[37] Assamagan K. and Y. Coadou. The hadronic tau decay of a heavy charged higgs in atlas. 2000. ATL-PHYS-2000-031.

[38] LHC yellow book. CERN-AC-95-05 LHC, 1995.

[39] A large hadron collider beauty experiment for precision measurements of CP-violation and rare decays, Technical Proposal. CERN/LHCC/98-4, 1998.

[40] S. Lowette et al. Heavy charged mssm higgs boson in the $h^{\pm} \rightarrow tb$ decay in cms. 2004. CMS-NOTE-2004-017.

[41] F. Mandl and G. Shaw. *Quantum field theory*. Chichester, UK: Wiley, 1984.

[42] Stephen P. Martin. A supersymmetry primer. 1997. hep-ph/9709356.

[43] R. B. Nickerson et al. Robotic mounting of atlas barrel sct modules. *Nucl. Instrum. Meth.*, A568:686–691, 2006.

[44] Ola K. Øye. A setup for electrical quality assurance of atlas sct barrel modules. Master's thesis, University of Bergen, 2003.

[45] Ola K. Øye. *Preparing the ATLAS experiment - SemiConductor Tracker commissioning and simulation studies of SUSY models*. PhD thesis, University of Bergen, 2007. ISBN 978-82-308-0304-2.

[46] PVSS II by ETM, Austria: http://www.pvss.com/.

[47] Phillips P.W. and Eklund L. Electrical Tests of SCT Hybrids and Modules, 2003.

[48] Cook J. R. and Thomas G. *ELMB128 Documentation*, 2004. ATL-DQ-ON-0006.

[49] Lisa Randall and Raman Sundrum. Out of this world supersymmetry breaking. *Nucl. Phys.*, B557:79–118, 1999. hep-th/9810155.

[50] Kersten S. and Kind P. *Pixel Patch Panel PP3 Design*. ATL-IP-ES-0075.

[51] SMI++ - State Management Interface: http://smi.web.cern.ch/smi/.

[52] Y. Unno. Atlas sct hybrid experience. Prepared for 11th Workshop on Electronics for LHC and Future Experiments (LECC 2005), 2005.

[53] Filimonov V. *OPC CANopen Server User Guide*. ATL-DQ-ON-0007, EDMS id 684951.

[54] G. Viehhauser. Macro-assembly of the atlas barrel sct. *Nuclear Science Symposium Conference Record, 2004 IEEE*, 2:1188–1191, 2004.

[55] W.-M. et al. Yao. Review of Particle Physics. *Journal of Physics G*, 33:1+, 2006.